

# **Photonic microstructures in optical fiber and their sensing applications**

By

Behzad Sadri

A Thesis Submitted in Partial Fulfillment of  
the Requirements for the Degree of

**Master of Science**

Department of Physics and Physical Oceanography  
Memorial University of Newfoundland

December 2021

St. John's

Newfoundland

## **Abstract**

Optical fiber sensors have attracted significant interest in their physical properties and potential applications due to their advantages of compact size, light weight, immunity to electromagnetic interference, and viability in harsh environments. To achieve the potential for applications, it is essential to reveal the underlying physics through both experimentation and simulation, which is an ongoing task now. In this study, microstructures in optical fiber, such as tapers and long-period grating (LPG), are investigated by simulation with COMSOL Multiphysics software, which is also compared with experiments in this study or the experimental results achieved by this group. In the experimentation of this study, the effects of different fabrication parameters on the formation of micro-taper in optical fiber and the transmission spectra of the resulting LPGs are carried out, which indicates that the average diameter of the micro-taper decreases and a blueshift in the transmission spectrum of the LPG occurs by increasing any of the three fabrication parameters such as arc current, arc duration, and tension along the fiber. The sensitivities of LPG to environmental refractive index and temperature are studied computationally, which shows the highest sensitivity of refractive index of 171.82 nm/RIU (Refractive Index Unit) and the temperature sensitivity of 10 pm/°C. Furthermore, tapered fibers in the configurations of either single or in-line Mach-Zehnder interferometer are studied as biosensors for detecting the concentration of Streptavidin (SV) protein computationally and compared with the experimental results previously obtained in our research group. The simulation results show good agreement with the experimental results

indicating the effective refractive indices of the coating materials play a significant role in determining the sensitivity. The findings achieved from this study are helpful for designing LPG-based and tapered fiber-based optical fiber sensors and biosensors, which enable the applications of these optical sensors in various fields, such as telecommunication, chemistry, medical and environmental sciences.

## **Acknowledgments**

I would like to express my special thanks to my supervisors Prof. Qiying Chen and Dr. Liqiu Men, for accepting me as their students in this field and for all their guidance and encouragement. Also, I sincerely appreciate the Physics and Physical oceanography department for providing facilities for this project. I want to extend my gratitude to the School of Graduate Studies (SGS) of the Memorial University of Newfoundland for funding and supporting me during my educations.

I cannot forget to offer my sincere thanks to my family and friends for supporting me and their valuable feedback, which was very helpful for completing this project.

# Table of Contents

<b>Abstract.....</b>	<b>I</b>
<b>Acknowledgments .....</b>	<b>III</b>
<b>Table of Contents .....</b>	<b>IV</b>
<b>List of Figures.....</b>	<b>VII</b>
<b>List of Abbreviations .....</b>	<b>XII</b>
<b>Chapter 1 Introduction.....</b>	<b>1</b>
1.1 Propagation of light in optical fiber .....	3
1.2 Types of optical fiber sensors .....	9
1.3 Interferometric optical fiber sensors .....	13
1.4 Long-period grating .....	18
1.4.1 LPG fabrication techniques.....	21
1.4.2 Theory of LPG .....	22
1.5 A brief review of biosensing experimental results .....	24
1.5.1 Biosensor coated with (PAH/SiO <sub>2</sub> :Au) <sub>3</sub> /Biotin .....	24
1.5.2 Biosensor coated with (PAH/PSS) <sub>3</sub> /Biotin .....	27
1.6 A brief introduction to COMSOL Multiphysics software .....	29
1.7 Thesis outline .....	30
<b>Chapter 2 Experimental details.....</b>	<b>32</b>
2.1 General fabrication processes using electric arc discharge method.....	33
2.2 Sample preparation .....	36
2.2.1 Variation of arc current .....	36
2.2.2 Variation of arc duration .....	43
2.2.3 Variations of tension .....	44
2.3 Geometric properties of micro-tapered fibers.....	45
<b>Chapter 3 Simulation on the formation and application of long-period gratings ....</b>	<b>49</b>
3.1 Micro-taper analysis using two methods in COMSOL® .....	49
3.1.1 Simulation on the tapered fiber using the full-wave method.....	52
3.1.2 Simulation on the tapered fiber using the beam envelope method .....	56
3.2 Geometry deformation in the fiber using the arc discharge.....	60

3.2.1 Structure model .....	62
3.2.2 Material model .....	63
3.2.3 Glass fiber necking .....	64
3.3 Simulation on the effect of fabrication parameters on the formation of the LPG .....	67
3.3.1. LPG electric field distribution and transmission spectrum.....	67
3.3.2 Effect of the number of gratings on the properties of LPG .....	72
3.3.3 Influence of arc current variation on the transmission spectrum of LPG .....	73
3.3.4 Influence of arc duration variation on the transmission spectrum.....	75
3.4 Use of LPG as a sensor .....	81
3.4.1 LPG as an environmental refractive index sensor .....	81
3.4.2 LPG as a temperature sensor.....	86
<b>Chapter 4 Tapered fibers as a protein sensor .....</b>	<b>91</b>
4.1 Introduction.....	91
4.1.1 Structure functionalization.....	92
4.1.2 Adsorption process.....	94
4.1.3 Simulation on sensing of Streptavidin protein concentration .....	95
4.2 Single tapered fiber biosensors .....	96
4.2.1 Single tapered fiber biosensors coated with (PAH/SiO <sub>2</sub> :Au) <sub>3</sub> /Biotin, with a waist of 97, 58, or 45 μm.....	96
4.2.2 Single tapered fiber biosensor coated with (PAH/PSS) <sub>3</sub> /Biotin .....	103
4.3 Inline tapered fiber Mach-Zehnder Interferometer as a protein sensor .....	110
4.3.1 Properties of an inline symmetrical MZI coated with (PAH/SiO <sub>2</sub> :Au) <sub>3</sub> /Biotin.....	112
4.3.2 Properties of an inline asymmetrical MZI coated with (PAH/SiO <sub>2</sub> : Au) <sub>3</sub> /Biotin .....	114
4.3.2.1 Analysis on results of simulation on symmetrical and asymmetrical MZI coated with (PAH/SiO <sub>2</sub> :Au) <sub>3</sub> /Biotin .....	116
4.3.3 MZI protein sensor coated with (PAH/PSS) <sub>3</sub> /Biotin .....	117
4.3.3.1 Properties of an inline symmetrical Mach-Zehnder Interferometer coated with (PAH/PSS) <sub>3</sub> /Biotin.....	118
4.4 Differences between the sensitivities of two biosensors.....	123
<b>Chapter 5 Conclusion .....</b>	<b>127</b>
<b>References .....</b>	<b>132</b>

## List of Tables

Table 1.1 Resonance wavelength shifts due to the different concentrations of protein. ..	28
Table 2.1 Samples obtained from arc current variations while arc duration and tension remain constant at 150 ms and 1.275 g.....	42
Table 2.2 Samples fabricated with different arc durations set in the fiber fusion splicer (arc current: 10 mA, tension: 12.5 mN).....	43
Table 2.3 Samples fabricated with a different tension set in the fiber fusion splicer (arc current: 10 mA, arc duration: 250 ms).....	45
Table 3.1 Numerical values for parameters relating with the hardening function.....	63
Table 3.2 Physical parameters of a single-mode fiber.....	87
Table 4.1 Resonance wavelength shifts due to the addition of protein with different concentrations .....	101
Table 4.2 Resonance wavelength shifts for three (PAH/PSS) <sub>3</sub> /Biotin-coated single tapered fibers having different waists thicknesses.....	109

## List of Figures

Figure 1.1 Schematic illustration of a single-mode fiber. The fiber core and cladding are protected by the fiber buffer jacket. ....	3
Figure 1.2 Propagation of light inside a fiber relying on total internal reflection. ....	4
Figure 1.3 Relationship between electric field vectors and intensity profiles of $LP_{lm}$ modes and conventional modes. ....	8
Figure 1.4 Basic components of an optical fiber sensor system. ....	10
Figure 1.5 (a) Extrinsic and (b) intrinsic types of optical fiber sensors. ....	11
Figure 1.6 Types of Fabry-Perot Interferometer sensors: (a) extrinsic; (b) intrinsic FPI ( $M_1$ and $M_2$ are mirrors). ....	13
Figure 1.7 Schematic illustrations of an optical fiber Sagnac interferometer. ....	14
Figure 1.8 Schematic illustration of an optical fiber Michelson interferometer. ....	15
Figure 1.9 Schematic illustration of an optical fiber MZI. ....	16
Figure 1.10 Example of an interference pattern made using a Mach-Zehnder interferometer .....	17
Figure 1.11 Some types of in-line fiber MZI sensors based on (a) tapers; (b) core offset. ....	18
Figure 1.12 Schematic illustrations of an FBG. The output light includes all wavelengths except the Bragg wavelength. ....	19
Figure 1.13 Schematic illustration of changes in the spectrum during light propagation through an LPG. The output light includes several dips, which correspond to the resonance wavelengths ( $\lambda_R$ ) because of the presence of LPG. ....	20
Figure 1.14 Transmission spectrum of a typical LPG. Each dip in the wavelength axis indicates resonance wavelengths resulting from coupling the core mode with one order of cladding modes. ....	23
Figure 1.15 (a) Transmission spectra of tapered MZI before and after coating (PAH/SiO <sub>2</sub> :Au NPs) <sub>3</sub> /Biotin, and (b) at $\lambda = 1553.22$ nm (Reprinted from [67], with permission). ....	26
Figure 1.16 Transmission spectra of tapered MZI before and after coating (PAH/PSS) <sub>3</sub> /Biotin, as well as their exposure to streptavidin solutions of different concentrations (reprinted from [67], with permission). ....	28
Figure 2.1 Fabrication of LPG in this study: (a) use of arc discharge to write LPG on the fiber, (b) setup for fabricating LPG on the fiber. ....	33
Figure 2.2 Fusion splicer used in this study (FITEL S182A): (a) the instrument with display and keyboard; (b) electrodes, V-grooves, and fiber holders as the key components of the instrument. ....	34

Figure 2.3 Schematic illustration of fusion splicer components used in this study.....	35
Figure 2.4 Complete setup for LPG writing on a single-mode optical fiber. ....	35
Figure 2.5 Arc discharge written LPG in SMF: arc current, 5mA; arc duration, 150 ms; tension, 12.5 mN. ....	37
Figure 2.6 Raw transmission spectrum of arc discharge-written LPG in SMF: arc current, 5mA; arc duration, 150 ms; tension, 12.5 mN; periodicity of grating, 762 $\mu\text{m}$ ; number of gratings, 100. ....	37
Figure 2.7 LPG written in SMF: arc current, 10 mA; arc duration, 150 ms; tension, 12.5 mN.....	38
Figure 2.8 Raw data of arc discharge-written LPG in SMF: arc current, 10 mA; arc duration, 150 ms; tension, 12.5 mN; periodicity of grating, 508 $\mu\text{m}$ ; number of gratings, 70.....	39
Figure 2.9 LPG fabricated in SMF with an arc current of 15 mA, arc duration of 150 ms, tension, 12.5 mN, and grating periodicity of 508 $\mu\text{m}$ .....	40
Figure 2.10 Microstructures fabricated in SMF with an arc current of 20 mA, arc duration of 150 ms, and tension of 12.5 mN.....	41
Figure 2.11 Microstructures fabricated in SMF with an arc current of 25 mA, arc duration of 150 ms, and tension of 12.5 mN.....	42
Figure 2.12 The free body diagram of the fiber and hanging weight. The tension along the fiber equals the gravity force of the mass ( $T = mg$ ) .....	44
Figure 2.13 Dependence of micro-taper diameter as a function of arc current strength. .	46
Figure 2.14 Dependence of micro-taper diameter as a function of arc duration. ....	47
Figure 2.15 Dependence of the diameter of micro-taper as a function of tension.....	47
Figure 3.1 Geometry of a single-mode fiber modeled in the full-wave simulation. The dimensions are much smaller than those of the actual fiber. ....	53
Figure 3.2 Input electric field amplitude achieved from full-wave simulation for a tapered fiber. ....	54
Figure 3.3 Output electric field amplitude obtained from the full-wave simulation for (a) no tapering, and (b) a tapered waist of 5 $\mu\text{m}$ . There is a decrease in electric field amplitude for smaller waist tapers. ....	55
Figure 3.4 Wave propagation in a waveguide with transverse and longitudinal components of the wave constants labeled as $\beta_{\perp}$ and $\beta_{\parallel}$ , respectively, in which $\beta_{\parallel}$ refers to ewbe. beta_1.....	57
Figure 3.5 (a) Geometry of a fiber modeled in the beam envelope simulation. (b) input electric field amplitude achieved using the beam envelope method in COMSOL.....	58

Figure 3.6	Output electric field amplitude for a tapered fiber simulated using the beam envelope method for (a) a fiber without tapering, and (b) a tapered fiber waist of 25 $\mu\text{m}$ .	59
Figure 3.7	Schematic illustration of viscous stretching conforming to the temperature profile, scaled by color.	60
Figure 3.8	Stress-strain relationship in the uniaxial tensile stretching of a viscoelastic material.	61
Figure 3.9	Schematic illustration of the model of the optical fiber used in this simulation. The dashed line and the square indicate the rotational symmetrical axis and mirror, respectively.	62
Figure 3.10	Nonlinear isotropic hardening as a function of equivalent plastic strain for a glass fiber.	64
Figure 3.11	Simulation results for stretched fiber under the stress of 3 MPa. The stress is scaled by color.	66
Figure 3.12	Necking development in the middle section of a fiber at a temperature of 1300°C and stress of 3 MPa.	67
Figure 3.13	Geometry of one period of a two-dimensional model of the LPG in COMSOL. The y-direction is compressed by 0.5 to permit the entire period to be represented in the figure. The vertical axis scale is ( $\mu\text{m}$ ), and the transverse axis is scale ( $\times 10^4 \mu\text{m}$ ).	68
Figure 3.14	Electric field distribution in all fiber areas at a wavelength of 1550 nm. The color scale shows that most light energy propagates along the fiber core....	70
Figure 3.15	Transmission spectrum of an LPG with a periodicity of 500 $\mu\text{m}$ , a grating number equal to 100, and a grating length of 100 $\mu\text{m}$ .	71
Figure 3.16	Evolution of the transmission spectra of LPGs with an increase in the grating number.	72
Figure 3.17	Evolution of the LPG transmission spectrum with varying arc current during fabrication.	74
Figure 3.18	Dependence of resonance wavelength of the LPG on arc current.	75
Figure 3.19	Intensity loss variations of the LPG when the arc current changes.	75
Figure 3.20	Changes in the transmission spectrum of the LPG resulting from arc duration variations.	76
Figure 3.21	Shifts in the resonance wavelength of the LPG resulting from variation in arc duration.	77
Figure 3.22	Changes in intensity loss of the LPG resulting from arc duration variation.	78
Figure 3.23	Changes in the transmission spectrum of LPG resulting from tension variation.	79
Figure 3.24	Shifts in the resonance wavelength of the LPG when the tension changes.	79
Figure 3.25	Changes in the intensity loss of the LPG resulting from tension variation.	80
Figure 3.26	Geometry of 2D model of LPG adopted in COMSOL simulation.	82

Figure 3.27 Influence of refractive index variation on resonance wavelength in arc-induced transmission spectra of LPG (simulation results). .....	83
Figure 3.28 Dependence of resonance wavelength shifts on environmental refractive indices for an arc-induced LPG (simulation results). .....	84
Figure 3.29 (a) Influence of temperature variation on resonance wavelength in the transmission spectrum of an arc-induced LPG. (b) enlarged curves of the resonances at around 1665.70 nm. ....	89
Figure 3.30 Effects of temperature variation on resonance wavelength in the transmission spectrum of arc-induced LPG (simulation results). ....	90
Figure 4.1 Geometry of a tapered fiber used for sensing in simulation. ....	92
Figure 4.2 Schematic illustration of three bilayers used to functionalize a tapered fiber. ....	93
Figure 4.3 Adsorption reaction occurring between Biotin and Streptavidin protein on taper surface at room temperature. ....	95
Figure 4.4 (a) Transmission spectra of a tapered fiber biosensor coated with (PAH/SiO <sub>2</sub> : Au) <sub>3</sub> /Biotin, having a waist of 97 μm and surrounded by different concentrations of streptavidin protein; (b) enlarged curves in the vicinity of a resonance wavelength at 1564.42 nm. ....	98
Figure 4.5 (a) Transmission spectra of a tapered fiber biosensor coated with (PAH/SiO <sub>2</sub> : Au) <sub>3</sub> /Biotin, having a waist of 58 μm and surrounded by different SV concentrations; (b) enlarged curves in the vicinity of a resonance wavelength at 1571.85 nm. ....	99
Figure 4.6 (a) Transmission spectra of a tapered fiber biosensor coated with (PAH/SiO <sub>2</sub> : Au) <sub>3</sub> /Biotin, having a waist of 45 μm and surrounded by different SV concentrations; (b) enlarged curves in the vicinity of a peak wavelength at 1562.46 nm. ....	100
Figure 4.7 Comparison of resonance wavelength shifts for three tapered fiber-based biosensors with three different waist thicknesses, all coated with (PAH/SiO <sub>2</sub> : Au) <sub>3</sub> /Biotin. ....	102
Figure 4.8 Functionalization of tapered fiber with (PAH/PSS) <sub>3</sub> /Biotin coating. ....	103
Figure 4.9 (a) Transmission spectra of (PAH/PSS) <sub>3</sub> /Biotin-coated single tapered biosensor (97 μm waist) with different concentrations of streptavidin protein; (b) enlarged curves in the vicinity of the resonance wavelength at 1564.49 nm. ....	106
Figure 4.10 (a) Transmission spectra of (PAH/PSS) <sub>3</sub> /Biotin-coated tapered fiber biosensor (58 μm waist) surrounded by different concentrations of SV; (b) enlarged curves in the vicinity of the resonance wavelength at 1571.80 nm. ....	107

Figure 4.11 (a) Transmission spectra of (PAH/PSS) <sub>3</sub> /Biotin-coated tapered fiber biosensor (45 μm waist) surrounded by different concentrations of SV; (b) enlarged curves in the vicinity of the resonance wavelength at 1562.55 nm. ....	108
Figure 4.12 Comparison of resonance wavelength shifts for three single tapered fiber-based biosensors with three different waists thicknesses, all coated with (PAH/PSS) <sub>3</sub> /Biotin.....	109
Figure 4.13 Model of a Mach-Zehnder interferometer with a length of 4 cm, adopted for simulation using COMSOL Multiphysics. ....	111
Figure 4.14 (a) Transmission spectra of a coated FMZI (length: 4 cm) with different concentrations of streptavidin protein; (b) enlarged curves around the wavelength in the vicinity of 1555.75 nm. ....	113
Figure 4.15 (a) Transmission spectra of coated ((PAH/SiO <sub>2</sub> :Au) <sub>3</sub> /Biotin) asymmetrical MZI (4 cm in length) with different concentrations of streptavidin protein; (b) enlarged curves around the resonance wavelength of 1556.80 nm. ....	115
Figure 4.16 Comparison between results obtained through experimental and simulation studies on 4-cm-long symmetrical and asymmetrical MZI coated with (PAH/SiO <sub>2</sub> :Au) <sub>3</sub> /Biotin. The dotted line shows the experimental results [67], while the dashed and solid lines indicate the simulation results for symmetrical and asymmetrical MZI, respectively.....	116
Figure 4.17 (a) Transmission spectra of (PAH/PSS) <sub>3</sub> /Biotin-coated symmetrical MZI with a length of 4 cm in different concentrations of streptavidin protein; (b) enlarged transmission spectra around the resonance wavelength of 1556.10 nm. ....	119
Figure 4.18 (a) Transmission spectra of (PAH/PSS) <sub>3</sub> /Biotin-coated asymmetrical MZI with a length of 4 cm with different concentrations of streptavidin protein; (b) enlarged transmission spectra around the resonance wavelength of 1556.80 nm.. ....	121
Figure 4.19 Comparison between the experimental and simulation results of 4 cm-long symmetrical and asymmetrical MZI coated with (PAH/PSS) <sub>3</sub> /Biotin. The dotted line shows the experimental result, while the dashed and solid lines indicate the simulation results for symmetrical and asymmetrical MZI, respectively. ....	122
Figure 4.20 Shifts in the transmission spectrum of the MZI due to changes in the environmental refractive index around 1.330. ....	124
Figure 4.21 Shifts in the transmission spectrum of the MZI due to variations in the environmental refractive index around 1.4200. ....	125

## List of Abbreviations

FBG	Fiber Bragg Grating
FOS	Fiber-Optic Sensors
FPI	Fabry-Perot Interferometer
LBL	Layer-By-Layer
LPG	Long Period Grating
MMF	Multi-Mode Fiber
MZI	Mach-Zehnder Interferometer
NPs	Nanoparticles
PAH	Poly (allylamine hydrochloride)
PSS	Poly (sodium 4-styrenesulfonate)
RI	Refractive Index
RIU	Refractive Index Unit
SMF	Single-Mode Fiber
SV	Streptavidin

## **Chapter 1 Introduction**

Photonic components and devices play essential roles in many optoelectronic applications. Significant efforts have been undertaken to fabricate micro-/nano-structures onto tiny components in order to achieve enhanced performance on a small footprint. Optical fibers have been well recognized as an excellent medium to achieve these aims. In 1966, Dr. C. Kao and his colleagues at Standard Telecommunication Laboratories Ltd. were the first group to propose the idea of an optical fiber to transmit information [1]. Optical fibers are cylindrical waveguides carrying light along their length and have undoubtedly revolutionized modern communications and optical science. The 2009 Nobel prize awarded to Dr. Kao demonstrates the importance of this innovative discovery.

Since attenuation in optical fibers was reduced below 20 dB/km, optical fibers have been employed in communication systems, lighting applications, imaging optics, and laser gain media. In parallel with these developments, optical fiber sensors, which exploit the optoelectronics technologies and fiber optic communications, have fascinated the researchers and tantalized the application engineers for over fifty years. Among the different optical fiber applications, using optical fibers as sensors provides tremendous advantages that are very attractive for various industries.

Optical fiber sensors have high sensitivity to external physical perturbations, such as the refractive index of the surrounding medium, temperature, strain, and current. Sensitivity measured using the optical method is often dramatically higher than that measured from electrical sensors. Also, using electrical sensors in some harsh environments may not be possible. Optical fiber sensors are the highly practical, if not the only solution for such conditions, due to their immunity to electromagnetic interference and their resistance to high temperatures and corrosive substances. The small size and light-weight of optical fibers make them suitable for limited space and portable applications. Easy access to low-cost, long fibers makes them excellent candidates for remote and distributed sensing systems. Over the past several decades, these advantages have been demonstrated by many different types of fiber sensors.

## 1.1 Propagation of light in optical fiber

As shown in Fig. 1.1, an optical fiber is a cylindrical waveguide composed of a core (6 to 10  $\mu\text{m}$  in diameter for a single-mode fiber) surrounded by a cladding (125  $\mu\text{m}$  in diameter). These two layers are protected from physical damage by a plastic buffer jacket that generally has a diameter of 250  $\mu\text{m}$ . Although solving Maxwell's equations gives a clear idea of how an optical fiber guides a light beam, geometrical optics approximations can provide a straightforward overview of light propagation in optical fibers [2].

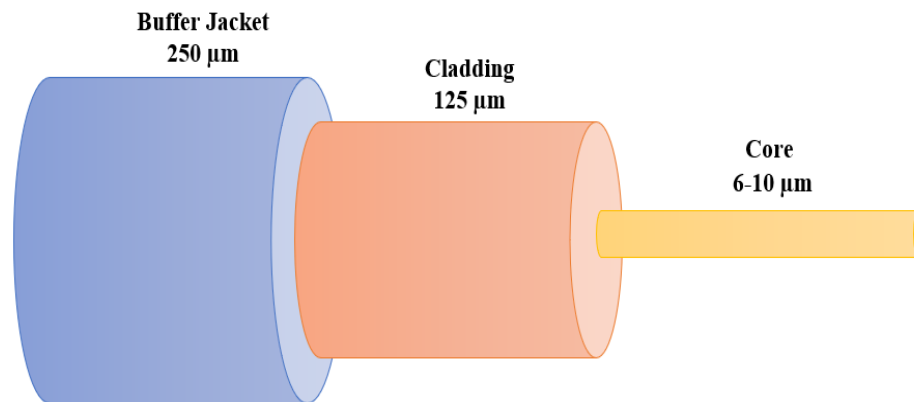


Figure 1.1 Schematic illustration of a single-mode fiber. The fiber core and cladding are protected by the fiber buffer jacket.

According to geometrical optics for a plane wave incident on a boundary at angle  $\theta_i$  (incident angle) between two media that have two different refractive indices, part of the light will be reflected at an angle equal to the incident angle, and the other part will be transmitted to the second medium, in accordance with Snell's law:

$$n_a \sin \theta_i = n_{co} \sin \theta_t, \quad (1.1)$$

where  $\theta_t$  is the transmission angle, and  $n_a$  and  $n_{co}$  are the air and fiber core refractive indices (see Fig. 1.2, point A).

Light propagation in an optical fiber is achieved from total internal reflection rule. Suppose the core and cladding refractive indices are considered as  $n_{co}$  and  $n_{cl}$ , respectively (Fig. 1.2), when light propagates from a higher refractive index medium (fiber core) towards a lower refractive index medium (fiber cladding) with an incident angle greater than a critical angle ( $\theta_c = \sin^{-1} n_{cl}/n_{co}$ ), it is reflected back to the medium with the higher refractive index (see Fig 1.2, point B) [3]. According to this effect, a light beam is limited to propagating within the core. As long as the fiber is not significantly bent, a light beam can propagate over a very long distance along the fiber with very low intensity loss in the order of 0.2-1 dB/km [2].

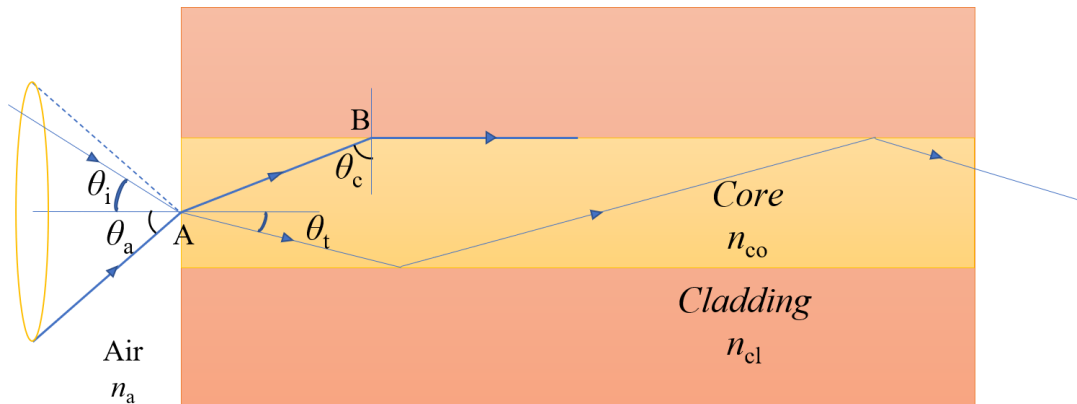


Figure 1.2 Propagation of light inside a fiber relying on total internal reflection rule.

The total internal reflection criterion limits the incidence angle of a light beam that strikes the fiber core from outside. Only beams with an incident angle smaller than an absolute maximum can propagate through the fiber. This absolute maximum is called the

acceptance angle ( $\theta_a$ ) and is identified as the arcsine of the fiber's numerical aperture (NA), which is given by [3]:

$$NA = \sqrt{n_{co}^2 - n_{cl}^2}. \quad (1.2)$$

Therefore, beams with an incident angle greater than  $\theta_a = \sin^{-1}(NA)$  are not propagated within the fiber core (Fig 1.2).

Another critical parameter in the fiber optics field is the  $V$ -number or normalized frequency. To better understand this parameter, it is necessary to have prior knowledge of mode theory. Mode theory uses electromagnetic wave theory to describe light propagation through a fiber. An optical fiber is a linear, isotropic, homogeneous, lossless dielectric material without any sources, including currents, free charges, and ferromagnetic media; therefore, the relevant Maxwell's equations can be written as follows [3]:

$$\nabla \times \mathbf{E} = -\frac{\partial \mathbf{B}}{\partial t}, \quad (1.3 \text{ a})$$

$$\nabla \times \mathbf{H} = \frac{\partial \mathbf{D}}{\partial t}, \quad (1.3 \text{ b})$$

$$\nabla \cdot \mathbf{D} = 0, \quad (1.3 \text{ c})$$

$$\nabla \cdot \mathbf{B} = 0, \quad (1.3 \text{ d})$$

where  $\mathbf{E}$ ,  $\mathbf{H}$ ,  $\mathbf{D}$ , and  $\mathbf{B}$  are the electric field vector, magnetic field vector, electric displacement field vector, and magnetic induction vector, respectively. For isotropic materials, the material relationships are:

$$\mathbf{D} = \epsilon \mathbf{E}, \quad (1.4 \text{ a})$$

$$\mathbf{B} = \mu_0 \mathbf{H}, \quad (1.4 \text{ b})$$

where  $\varepsilon = \varepsilon_0 n^2$  is the dielectric permittivity of the isotropic medium with a dielectric permittivity of free space ( $\varepsilon_0$ ), and  $\mu_0$  is the magnetic permeability of the free space. Substituting Eqs. (1.4 a & b) for (1.3 a & b) and taking their curl provides two homogeneous wave equations for  $\mathbf{E}$  and  $\mathbf{H}$ , as follows:

$$\nabla^2 \mathbf{E} = \varepsilon \mu_0 \left( \frac{\partial^2 \mathbf{E}}{\partial t^2} \right), \quad (1.5 \text{ a})$$

$$\nabla^2 \mathbf{H} = \varepsilon \mu_0 \left( \frac{\partial^2 \mathbf{H}}{\partial t^2} \right), \quad (1.5 \text{ b})$$

In the next step, with the assumption of the time dependency of harmonic fields with an  $e^{(i\omega t)}$ , where  $\omega$  is the single angular frequency, and  $\beta$  is the propagation constant for a mode guided in the z-direction, the electric and magnetic field vectors in cylindrical coordinates can be written as [3]:

$$\mathbf{E} = \mathbf{E}_0(r, \varphi) \exp[i(\omega t - \beta z)], \quad (1.6 \text{ a})$$

$$\mathbf{H} = \mathbf{H}_0(r, \varphi) \exp[i(\omega t - \beta z)]. \quad (1.6 \text{ b})$$

This solution generally produces a set of electromagnetic field configurations that generate a standing wave pattern in a direction normal to the fiber axis. Based on the electromagnetic field pattern of radiation measured in a plane perpendicular to the propagation direction of the beam, there are different types of modes that can be classified as:

- Transverse electric (TE) modes:  $E_z = 0$ ,
- Transverse magnetic (TM) modes:  $H_z = 0$ ,

- Hybrid modes:  $E_z \neq 0$  and  $H_z \neq 0$ , depending on whether the magnetic component ( $H_z$ ), or the electric component ( $E_z$ ), has a dominant effect on the magnitude of transverse field, denoted as either  $HE$  or  $EH$  modes, respectively.

In optical fibers, due to the weakly guiding approximation ( $n_{cl}/n_{co} \cong 1$ ), fiber modes are usually known as linear polarization (LP) modes. Using this approximation makes it possible to achieve some modes with only one electric field component ( $E_x$ ,  $E_y$ , or  $E_z$ ). For the fundamental mode ( $HE_{11}$ ), using this approximation results in an exact linear polarised mode ( $LP_{01}$ ), while for higher-order modes, achieving single component modes (LP modes) requires a combination of modes achieved from the exact theory of waveguide [4]. The relationship between LP modes and conventional modes is represented in Fig. 1.3.

It is convenient to define the  $V$ -number or normalized frequency, which is expressed as follows [3]:

$$V = \frac{2\pi a}{\lambda} NA, \quad (1.7)$$

where  $\lambda$  is the vacuum wavelength,  $a$  is the fiber core radius, and  $NA$  is the numerical aperture. The  $V$ -number includes information regarding the range of propagation constants and the number of modes that a fiber can support. A fiber with a high  $V$ -number, which occurs in a fiber with a high core radius, can support several modes, but when the core radius decreases to a value at which the  $V$ -number is less than 2.405, all modes except the  $HE_{11}$  mode are cut-off. These fibers support a single-mode and are referred to as single-mode fibers. They support only  $HE_{11}$  mode, which is known as the fundamental fiber

mode.  $LP_{01}$  is denoted as the lowest order mode  $HE_{11}$ . The  $V$  value, 2.405, at which  $TE_{01}$  and  $TM_{01}$  reach the cut-off is known as the single-mode condition [5].

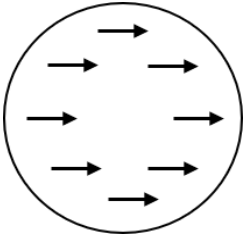
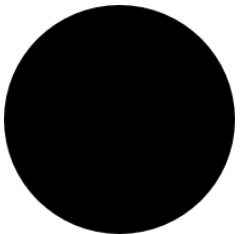
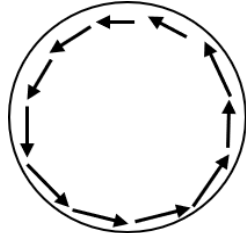
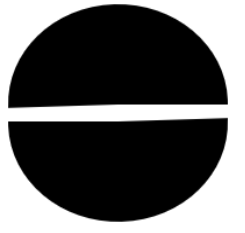
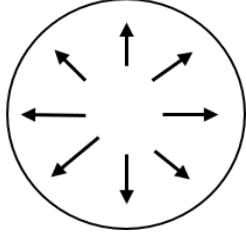
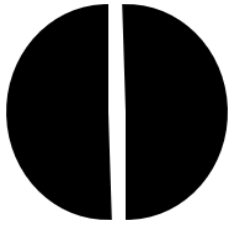
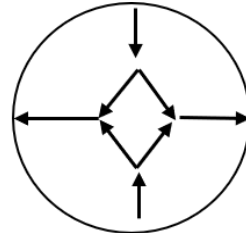
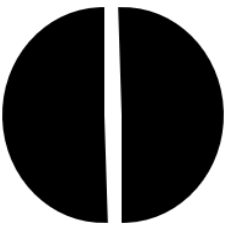
LP mode designations	Traditional designations	Electric field distribution	Intensity distribution of $E_x$
$LP_{01}$	$HE_{11}$		
$LP_{11}$	$TE_{01}$		
	$TM_{01}$		
	$HE_{21}$		

Figure 1.3 Relationship between electric field vectors and intensity profiles of  $LP_{lm}$  modes and conventional modes.

## **1.2 Types of optical fiber sensors**

In terms of operation, optical fiber sensors can be divided into two main groups: point optical fiber sensors operating in a localized area and distributed optical fiber sensors operating along the entire length of the fiber sensor. The operation principle of distributed optical fiber sensors is based on optical scatterings such as the scatterings of Rayleigh, Brillouin, and Raman. Every external disturbance, such as the environmental refractive index, temperature, strain, and pressure, can have a slight or massive effect on the intensity, frequency (wavelength), polarization, and optical backscattering of an optical fiber sensor. As a result, these devices can be used as measuring tools. However, there are some limitations in the operation of distributed optical fiber sensors due to, for instance, high cost or a bulky system. The best alternative for a distributed optical fiber sensor is a point optical fiber sensor. Point optical fiber sensors operate using different types of principles and geometries, including tapered fibers, fiber gratings, and various combinations such as those used in the Fabry-Perot Interferometer, Mach-Zehnder Interferometer, and other structures. Point optical fiber sensors have some advantages over distributed sensors, such as higher sensitivity, lower cost, lower weight, easier manufacturing, and greater compactness.

In terms of sensing location, optical fiber sensors can be classified as intrinsic or extrinsic sensors. When explaining this classification, one needs to consider the general components of a typical optical fiber sensor system.

As shown in Fig. 1.4 on general components, the first component is a light source, which can be any optical source like a laser, LED, or laser diode. The second component is the optical fiber. The third one is the transducer, the sensing or modulator that transduces the measurand to an optical signal. Detection of any modulation is done by the detector, which in most cases is an optical spectrum analyzer.

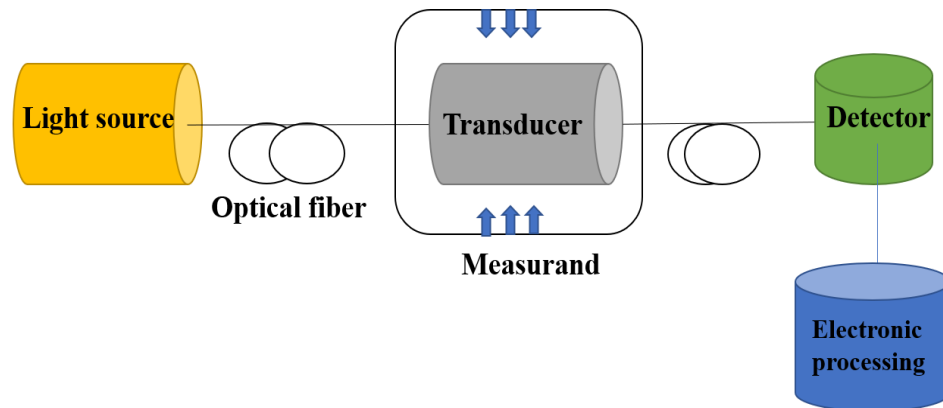


Figure 1.4 Basic components of an optical fiber sensor system.

In general, optical fiber sensors operate by modulating the intensity, phase, or polarization of the passing light. In an extrinsic type of optical fiber sensor, the optical fiber only plays a light carrier role to and from the external optical device where the sensing takes place. The fiber structure is not changed in any way for sensing purposes. Figure 1.5(a) shows this type of sensor. Examples of such types include optode [8], Doppler anemometers [9], non-contact vibration measurements systems [10], and fibers with end face mirrors or Fabry-Perot interferometers [11]. The main advantage of these sensors is their convenience when using an electrical counterpart would be impossible or prohibited.

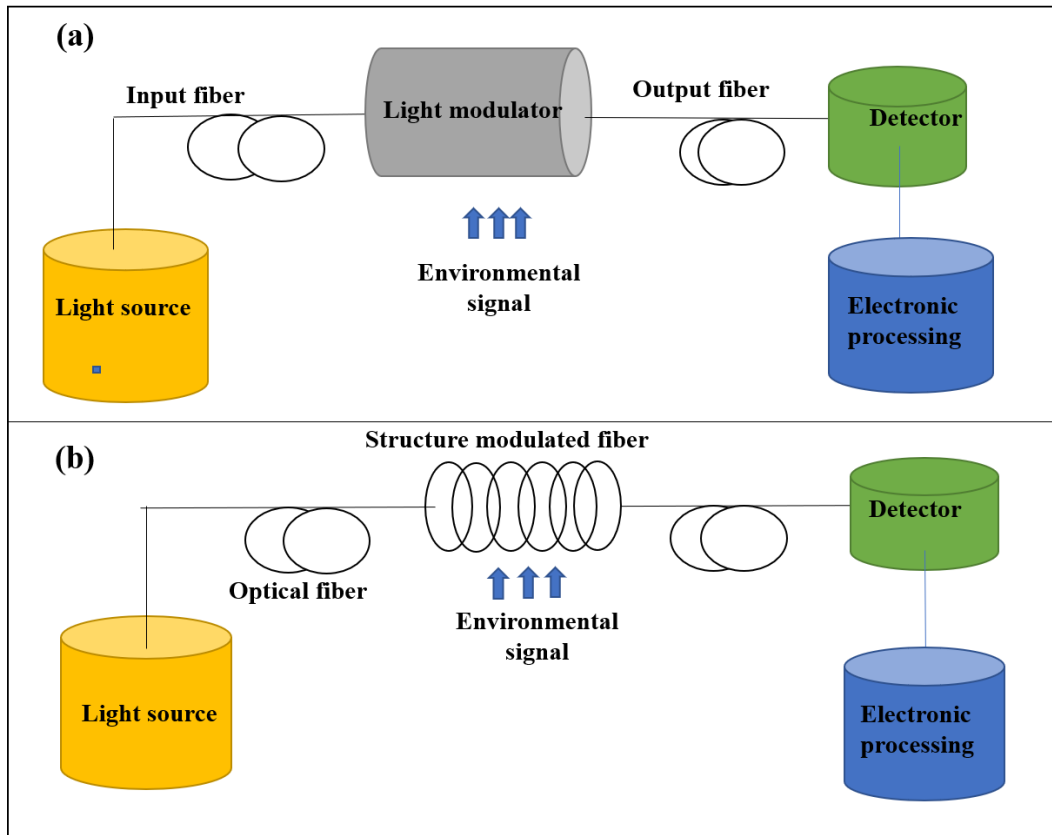


Figure 1.5 (a) Extrinsic and (b) intrinsic types of optical fiber sensors.

On the other hand, intrinsic optical fiber sensors do not require the light beam to leave the fiber for sensing purposes. For this type of optical fiber sensor, the fiber plays an active role in the sensing function by modulating its structure. The propagating light beam undergoes a modulation due to the written structures on the fiber. Examples of an intrinsic type of fiber sensor include the taper-based fiber sensor [12], grating-based fiber sensor [13], a sensor with modified cladding [14], and a micro or macro bend-based sensor [15, 16]. Figure 1.5(b) shows a schematic illustration of this type of sensor. Since the main topics of this thesis (long-period grating fibers and tapered fibers) focus on intrinsic optical fiber sensors, this study will examine this type of sensor in detail. Intrinsic optical fiber

sensors can be divided into different groups based on the electric field of the modulated light beam emanating from an intrinsic sensor. The light electric field can be expressed as:

$$\mathbf{E} = Ae^{i(\omega t - \varphi)}\hat{\mathbf{e}}, \quad (1.8)$$

where  $A$  is the amplitude,  $\omega$  is the angular frequency,  $\varphi$  is the phase, and  $\hat{\mathbf{e}}$  is the unit vector representing the polarization state. The light intensity is proportional to  $(|A|)^2$ , and the light beam wavelength is  $\lambda = 2\pi c/\omega$ , with  $c$  being the speed of light in the vacuum. The four fundamental elements of a light field on which external disturbances can modulate are intensity, phase, polarization state, and wavelength. Measuring these modulations can make it possible to sense specific external parameters. Based on this fact, intrinsic fiber sensors can be classified as wavelength-, intensity-, polarization-, or phase-based sensors.

Intensity-based fiber sensors rely on signal intensity variations in which the measurand modulates the intensity of propagating light through the fiber following various mechanisms such as transmission, reflection, micro-bending, or phenomena such as absorption, scattering, or fluorescence. Due to the attenuation of the signal, there will be a demand for a high intensity of light, and therefore, in most cases, multimode fibers are used in this type of sensor. Some advantages of this type of sensor include ease of use, low cost, and operational feasibility in real distributed sensors. Despite these advantages, this type of sensor is not very reliable due to relative measurements and some natural changes in light source intensities, which cause incorrect measurement results [17]. Wavelength modulated-based fiber sensors exploit light wavelength variations as a measuring tool for external parameter detection. Bragg grating sensors [18], black-body sensors [19], and fluorescent sensors [20] are some examples of this type. Another type of intrinsic fiber

sensor is the polarization modulating-based fiber sensor. This type of sensor works based on variations in the electric field direction of the light beam. The last type of sensor in the intrinsic fiber sensor class is based on phase variations of the light beam with the sensor exposed to external disturbances. Since in this type of sensor, phase modulation is detected by interferometry, most examples consist of interferometric fiber sensors, such as the Fabry-Perot etalon interferometer (FPI), Sagnac interferometer (SI), Michelson interferometer (MI), and Mach-Zehnder interferometer (MZI).

### 1.3 Interferometric optical fiber sensors

The early types of interferometric optical fiber sensors mainly were Fabry-Perot etalon. Figure 1.6 is a schematic illustration of this type of interferometer, which is divided into two main categories: extrinsic and intrinsic FPI. Both types consist of two mirrors that are distant from each other. If these mirrors are outside the fiber, the FPI is an extrinsic type (Fig 1.6(a)). In contrast, in the intrinsic type, the mirrors are located inside the fiber (Fig 1.6(b)). The mirrors reflect part of the incident light and pass the rest of the light through

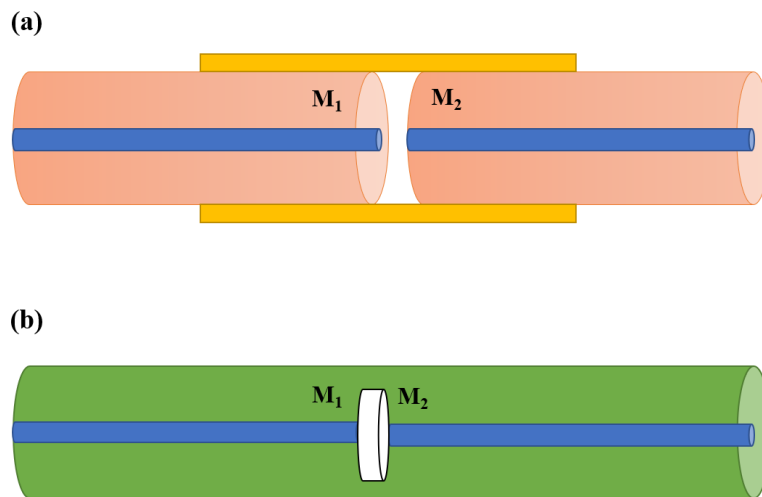


Figure 1.6 Types of Fabry-Perot Interferometer sensors: (a) extrinsic; (b) intrinsic FPI ( $M_1$  and  $M_2$  are mirrors).

the fiber. The interferometric pattern is the result of interference between two beams, one reflected and the other transmitted. For sensing purposes, external parameters will influence the optical path and change the beam phases, resulting in a shift in the interferometric pattern. FPIs have been used as sensors for the measurement of various physical parameters, such as temperature [21], pressure [22], strain [23], and refractive index [24].

Another common type of interferometer is the Sagnac interferometer. The fiber Sagnac interferometer is a type of two-beam, common-pass interferometric device. As shown in Fig. 1.7, the optical beam is first split into two beams by the beam splitter. These beams traverse the same fiber loop but in opposite directions, usually known as clockwise (CW) and counter-clockwise (CCW) directions. After traveling the entire loop, the two beams recombine at the optical coupler and form an interferometric pattern. Since the paths for both beams are the same, there is no optical phase difference; therefore, no interferometric pattern will be created at first sight. However, suppose one external disturbance, such as a change in the temperature or the refractive index, affects the fiber close to the loop end. An instant phase shift occurs in such a case, and an interferometric pattern is formed [25]. This feature makes it possible to use the Sagnac interferometer as

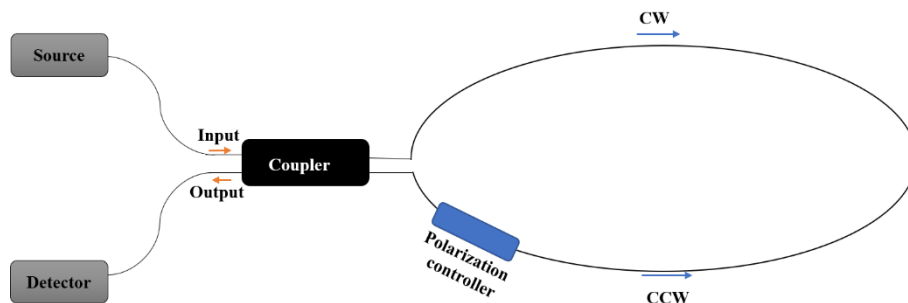


Figure 1.7 Schematic illustrations of an optical fiber Sagnac interferometer.

an online sensor for any variation in environmental perturbations. Nowadays, scientists use the Sagnac interferometer for measuring various physical parameters, such as temperature [26], magnetic field [27], and vibrations [28].

The third common interferometer is the Michelson interferometer (MI). The MI is a two-beam interferometer consisting of two arms and two mirrors connected by a coupler to recombine the beams and form interferometric patterns. Figure 1.8 is a schematic illustration of this type of interferometer. This interferometer is very similar to the MZI in terms of operation. Although the phase difference is twice that of the MZI (with resulting higher sensitivity), the MI requires very high-quality mirrors. This places the MI at a disadvantage compared with the MZI. Despite this problem, MI is often used for sensing purposes. Recently, Bao *et al.* used it for measuring temperature [29]. Another group measured environmental humidity by coating an MI-based fiber sensor with Methylcellulose film [30]. MI-based fiber sensors were also used for measuring liquid refractive index [31] and liquid level [32].

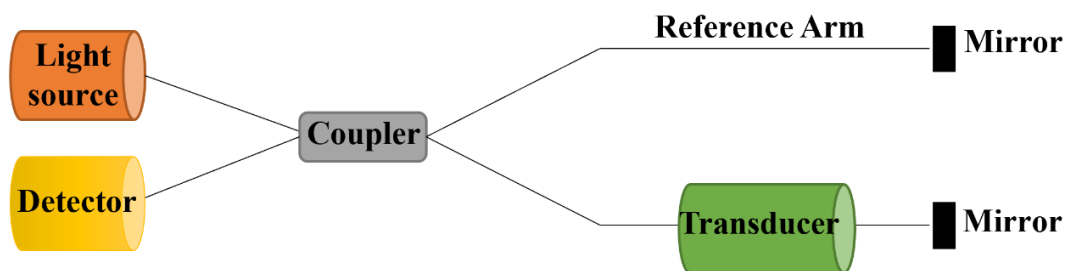


Figure 1.8 Schematic illustration of an optical fiber Michelson interferometer.

Since one of the focuses of this study is the Mach-Zehnder interferometer, it is discussed in detail here. The MZI is a typical two-beam optical fiber interferometer used

to disclose the phase difference between two collimated beams emitted from a coherent light source. It is suitable for measuring slight phase shifts in one of the two beams because of a slight external disturbance in the beam's path. Figure 1.9 is a schematic illustration of the fiber-based Mach-Zehnder interferometer.

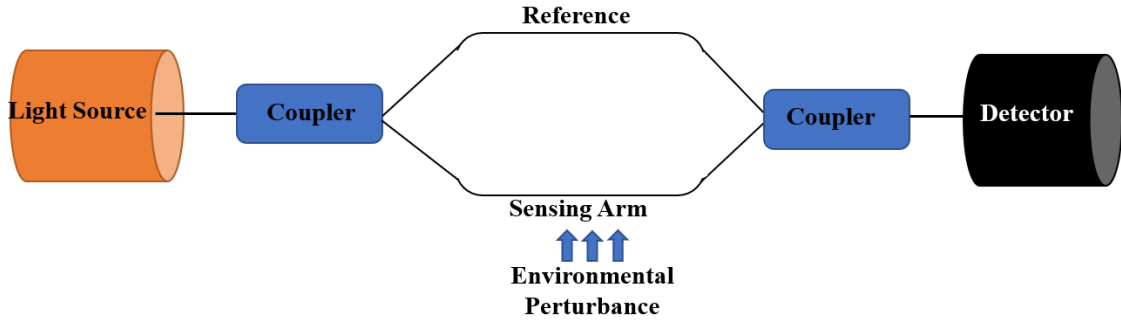


Figure 1.9 Schematic illustration of an optical fiber MZI.

As seen in the above figure, the MZI consists of three main parts. The first part is a coupler that splits the input light into two beams. The second part, in the center, is two separated arms, with one arm having a fiber length longer by  $\Delta L$ . This longer length gives the MZI the phase difference between the two beams propagated along the two paths. The last part is another coupler that recombines the two beams from the arms. An interferometric pattern is then made using a detector. The phase difference between the two beams in the arms can be calculated by [67]:

$$\Delta\varphi = \frac{2\pi n_2}{\lambda} (L + \Delta L) - \frac{2\pi n_1}{\lambda} L, \quad (1.9)$$

where  $n_1$  and  $n_2$  are refractive indices for different environments, and  $\lambda$  is the beam wavelength. It is worth noting that the resulting phase difference can be obtained from either a different optical path ( $\Delta L$ ) or a difference in the refractive index of the different

environments ( $n_1, n_2$ ). The typical transmission spectrum resulting from MZI is shown in Fig. 1.10.

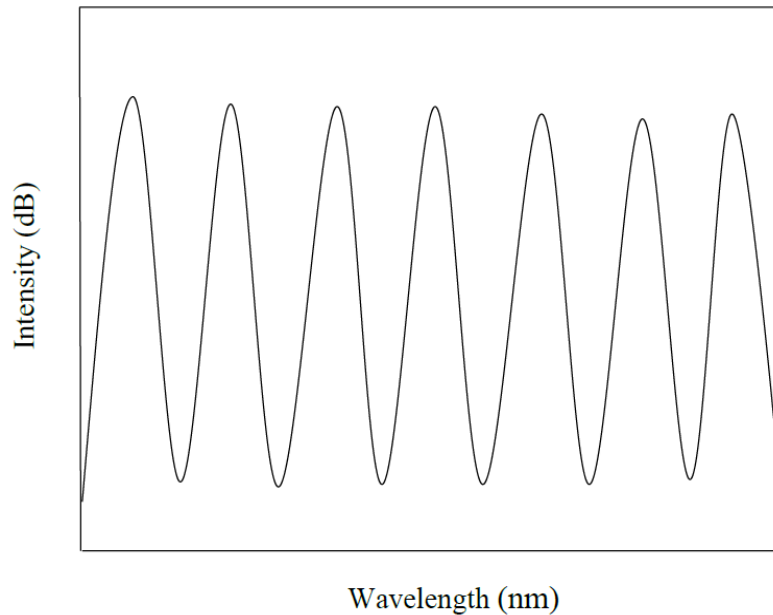


Figure 1.10 Example of an interference pattern made using a Mach-Zehnder interferometer.

In most cases, when measuring external parameters such as temperature or humidity, one arm is kept in contact with the environment. In contrast, the other arm, called the reference arm, is isolated from the surrounding space. The MZI is very flexible in shape. There are many examples of MZI sensors. In-line double tapered fiber MZI is one of the best-known types of MZI and has many different shapes. It can consist of two similar tapers, in which case it is called a symmetrical MZI, or two different tapers, in which case the resulting structure is called an asymmetrical MZI. Using a single-mode fiber between two multimode fibers, or vice versa, can create another shape of MZI. Figure 1.11 shows two possible forms which can be classified as MZI sensors.

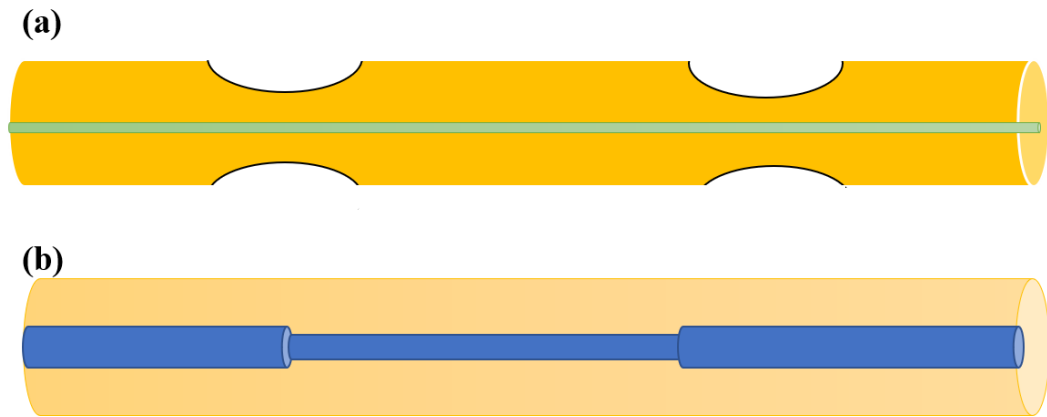


Figure 1.11 Some types of in-line fiber MZI sensors based on (a) tapers; (b) core offset.

## 1.4 Long-period grating

The invention of fiber gratings has significantly promoted developments in communication systems and optical fiber sensors. Fiber gratings have the ability to control different properties of propagating light through a fiber. They have various applications in communication systems, such as spectral filters, dispersion compensating components, and wavelength dividers in multiplexing systems [33, 34]. Also, their response to external perturbations, such as the environmental refractive index, temperature, electric field, and some biomolecules due to suitable surface functionalization, make these devices ideal candidates for sensing and biosensing purposes [35, 36]. Although the earliest fiber gratings were formed by creating periodic modulations in the core refractive index [33],

nowadays, fiber gratings are defined as a periodic perturbation in fiber parameters, which in most cases is the refractive index and/or the geometry of the fiber.

Fiber gratings depend on the periodic distances of the perturbations and can be divided into two main classes. In one class, these periods are shorter than one micron; this class can be named short period fiber grating or fiber Bragg gratings (FBG), as is common in the literature. Bragg gratings can couple the forward propagating core mode of the fiber with the backward, counter-propagated core mode due to its configuration. In each period, a small amount of light is reflected. All reflected light signals are coherently coupled at a particular wavelength in one considerable reflection, satisfying the Bragg condition ( $\lambda_B = 2n_{\text{eff}}\Lambda$  where  $n_{\text{eff}}$  and  $\Lambda$  are the effective refractive index of the fiber core and the periodicity of the FBG, respectively, and  $\lambda_B$  is the Bragg wavelength). Therefore, the output

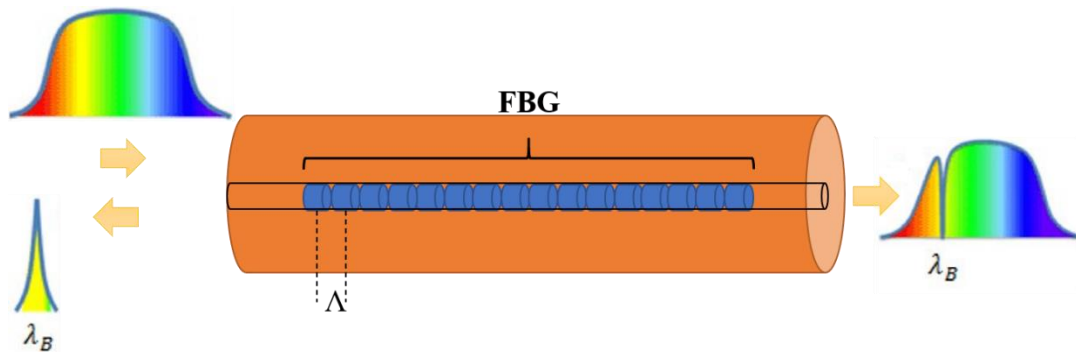


Figure 1.12 Schematic illustrations of an FBG. The output light includes all wavelengths except the Bragg wavelength.

light will include all input wavelengths except the Bragg wavelength [37, 38], as illustrated in Fig. 1.12.

In the other class, the periodicity of gratings is between 0.1 and 1 mm. This type of fiber grating is referred to as long-period gratings (LPG). In LPG-based fibers, periodic

refractive index modulations in the fiber core cause coupling between the core mode and the exciting forward propagating cladding modes [39]. However, the cladding modes are

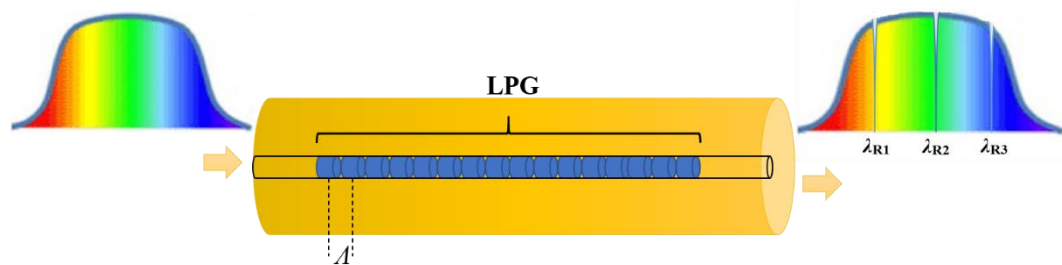


Figure 1.13 Schematic illustration of changes in the spectrum during light propagation through an LPG. The output light includes several dips, which correspond to the resonance wavelengths ( $\lambda_R$ ) because of the presence of LPG.

attenuated rapidly but leave several loss bands in the transmission spectrum centered at discrete wavelengths (resonance wavelengths). These discrete wavelengths are related with coupling the core mode to a different order of cladding modes. Figure 1.13 schematically shows these phenomena.

The resonance wavelength position and the resulting spectrum are very sensitive to the period and length of the LPG. These parameters are also quite sensitive to variations in external environment parameters, such as temperature, strain, bending, and the refractive index of the medium surrounding the fiber. These responsive properties make LPG applicable for sensing systems [39]. Their high sensitivity to the surrounding refractive index makes them suitable for super-sensing systems for chemical and biological materials [40]. Dissanayake *et al.* coated LPG fiber with graphene oxide and used it as a relative humidity and refractive index sensor [41]. In other work, Hromadka *et al.* used an LPG array to monitor temperature and relative humidity (RH) changes in air delivered by a mechanical ventilator operating in different modes [42]. Another group used LPG torsion

characteristics to utilize it as a twist sensor [43]. Yet, another group used Fe-C coated LPG to measure the mass loss for chemical purposes [44]. Richter *et al.* used coated LPG as a virus sensor for clinical and veterinary purposes [45]. In addition to coating, several approaches, such as cladding etching [46, 47] and exploitation near the LPG dispersion turning point [48], are employed to enhance their sensitivity to external parameters. LPG merits have been demonstrated by creating such structures on polymeric optical fibers. Polymeric long-period fiber gratings can support a more extensive strain range and possess a small Young's modulus [49, 50].

#### **1.4.1 LPG fabrication techniques**

Among different LPG fabrication techniques, the most important ones are the use of UV radiation [51], CO<sub>2</sub> lasers [52], IR femtosecond lasers [53], mechanical deformation [54], and electric arc discharge (EAD) [55]. Although one of the sophisticated techniques is the UV radiation approach, which can be applied to photosensitive fibers, some alternative, and cheaper methods, such as, CO<sub>2</sub> lasers or EAD, were proposed because of their flexibility and acceptable results. With these approaches, LPG can be created even in non-photosensitive and unconventional fibers. In 1996, Dianov *et al.* were the first to use the EAD method for writing LPG on a nitrogen-doped fiber [56]. Since then, research groups have used this technique to achieve many positive results and published many scientific reports [57, 58]. The EAD method involves applying an electric arc to fiber with a particular spatial periodicity, resulting in perturbations on the core and the cladding refractive indices [59, 60].

Since the EAD method was developed for writing LPG on a fiber, many attempts have been made to understand its mechanism. Rego *et al.* found that during arc discharge for typical fabrication parameters (10 mA and 250 ms, respectively), fiber temperature reaches a maximum of 1300 °C in less than half a second [58]. It has been proposed that the main reason for the formation of arc-induced perturbations may be due to local stress relaxation in the fiber core and cladding [61, 62]. This phenomenon makes some modifications to the local refractive indices of the core and the cladding. The discharge decreases the core refractive index in the order of  $10^{-4}$  and increases the cladding refractive index in the order of  $10^{-7}$  [62]. The EAD method for fabricating LPG offers some advantages. Firstly, gratings resulting from electric arc discharge have very high thermal stability due to their formation mechanisms, which rely on thermal effects [63]. This high thermal stability makes them the best candidate for use in high-temperature sensors in environments up to 1000°C [64] and, therefore, more suitable than gratings fabricated by other techniques such as UV radiation, in which high temperatures will eliminate the gratings [56]. Secondly, the fabrication cost is low since expensive equipment is not required. The method can also be used to write LPG on different fibers, including non-photosensitive fibers and photonic crystal fibers. However, the EAD method has some drawbacks, such as difficulty in reproducibility and difficulty in the fabrication of LPG with smaller periods.

#### **1.4.2 Theory of LPG**

The LPG hypothesis was developed in 1996 when Vengsarkar and his group used a UV laser to induce a periodic modulation in the refractive index of a fiber core [33]. Periodic

refractive index modulations in a fiber core cause coupling between the core mode and the excited forward propagating cladding modes. However, the cladding modes are attenuated rapidly but leave some series of loss bands in the transmission spectrum. Resonance wavelengths in the LPG transmission spectrum satisfy the phase-matching condition, which is given by [34, 65]:

$$\lambda_{res}^m = (n_{eff,co} - n_{eff,cl}^m)\Lambda, \quad (1.10)$$

where  $\Lambda$  is the grating period, and  $n_{eff,co}$ , and  $n_{eff,cl}^m$  are the effective refractive indices of the core and the  $m^{\text{th}}$  order of the cladding modes, respectively. The typical transmission spectrum for LPG is shown in Fig 1.14. The dips in the wavelength axis indicate resonance wavelengths.

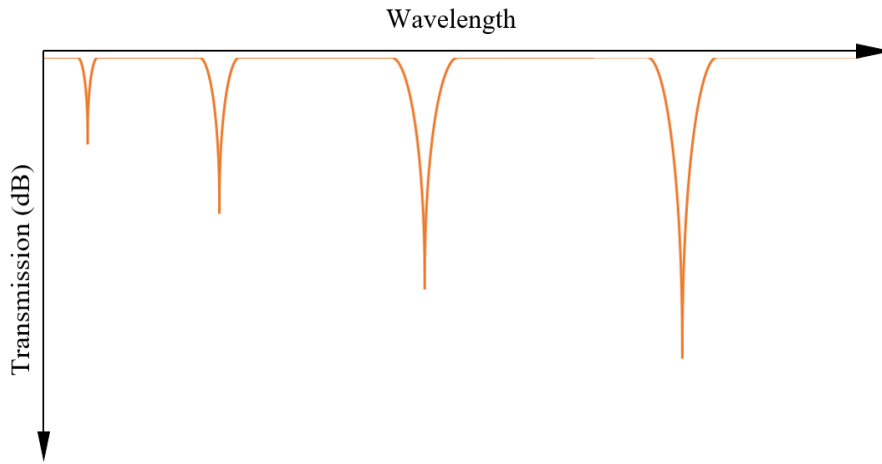


Figure 1.14 Transmission spectrum of a typical LPG. Each dip in the wavelength axis indicates resonance wavelengths resulting from coupling the core mode with one order of cladding modes.

One notable fact about beam transmission through a fiber is that when a light beam confronts an LPG in its path, it behaves like a sinusoidal function as follows [66]:

$$T = \cos\left(\frac{DL}{2}\right), \quad (1.11)$$

where  $L$  is the grating length equal to  $N \times \Lambda$  ( $N$  is the number of gratings, and  $\Lambda$  is the LPG periodicity) and  $D$  is the coupling coefficient that depends on the fiber core refractive index modulations.

## 1.5 A brief review of biosensing experimental results

In addition to investigations on arc-induced LPG properties, this study will simulate experiments performed by Maryam *et al.* to measure protein concentrations using a tapered fiber-based MZI coated with (PAH/SiO<sub>2</sub>:Au)<sub>3</sub>/Biotin and (PAH/PSS)<sub>3</sub>/Biotin [67], where PAH, SiO<sub>2</sub>:Au, and PSS are referred as poly (allylamine hydrochloride), silica and gold nanoparticles and poly(styrene sulfonate). The following is a brief explanation of their experiments. Their experimental results will be used as a reference to compare the simulation results obtained in this study. The software used for the simulation is COMSOL<sup>®</sup> Multiphysics Version 5.

### 1.5.1 Biosensor coated with (PAH/SiO<sub>2</sub>:Au)<sub>3</sub>/Biotin

For the experimental results [67], two types of streptavidin protein biosensors were examined. For one type, a symmetrical in-line tapered fiber MZI was coated with three bilayers of PAH/SiO<sub>2</sub>:Au NPs, covered with Biotin particles, since this material is the main material used for adsorbing proteins. In general, adsorbing proteins on a surface increase the effective refractive index of the bilayers, thereby causing a shift in the interferometric pattern. In the first step, bare MZI immersed in water was exposed to a broad-band light beam ranging from 1530 nm to 1580 nm, and the transmission was recorded. Then, an MZI

coated with the previously mentioned materials was used, and its transmission spectrum was collected. The subsequent steps included the addition of the protein in set concentrations: 83, 300, 800, and 1300 nM (nanomolar). The results are shown in Fig 1.15. The resonance wavelength shift for the coated material was  $0.18 \pm 0.01$  nm towards shorter wavelengths. This new point was chosen as the reference point for the following shifts. Adding proteins at 83 nM shifted the dip position by  $0.18 \pm 0.01$  nm towards shorter wavelengths. These phenomena were repeated for 300 and 1300 nM of SV concentration, which had the same blueshifts of  $0.27 \pm 0.01$  nm towards short wavelengths. An SV protein concentration of 800 nM resulted in the highest blueshift of  $0.36 \pm 0.01$  nm. This number was used in the sensitivity calculations for this biosensor. The decrease in the wavelength shift in transmission spectrum for 1300 nM protein concentration can be explained by the fact that an increase in protein concentration enhances the chance of protein particles being repelled by other proteins and increases the loss of more protein-biotin bonds in the washing process [67].

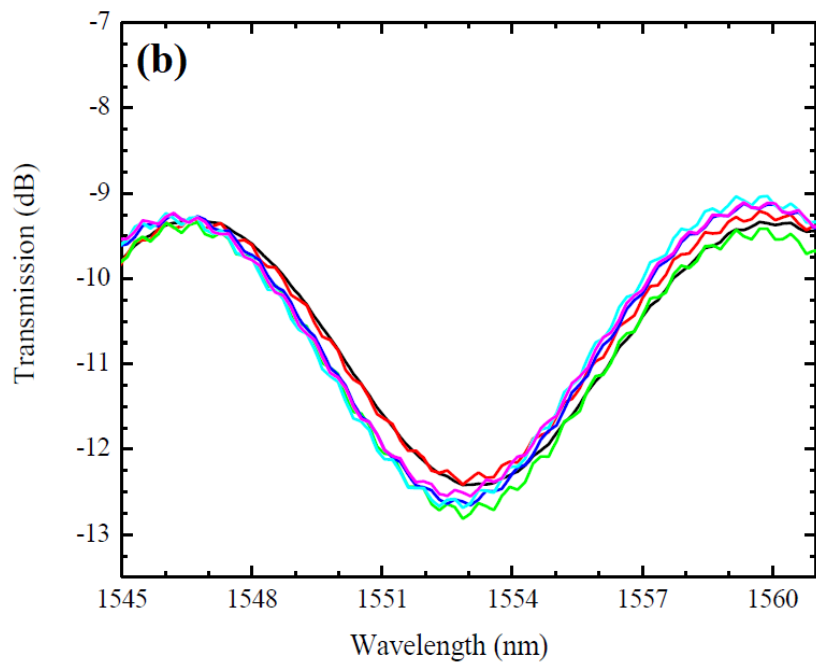
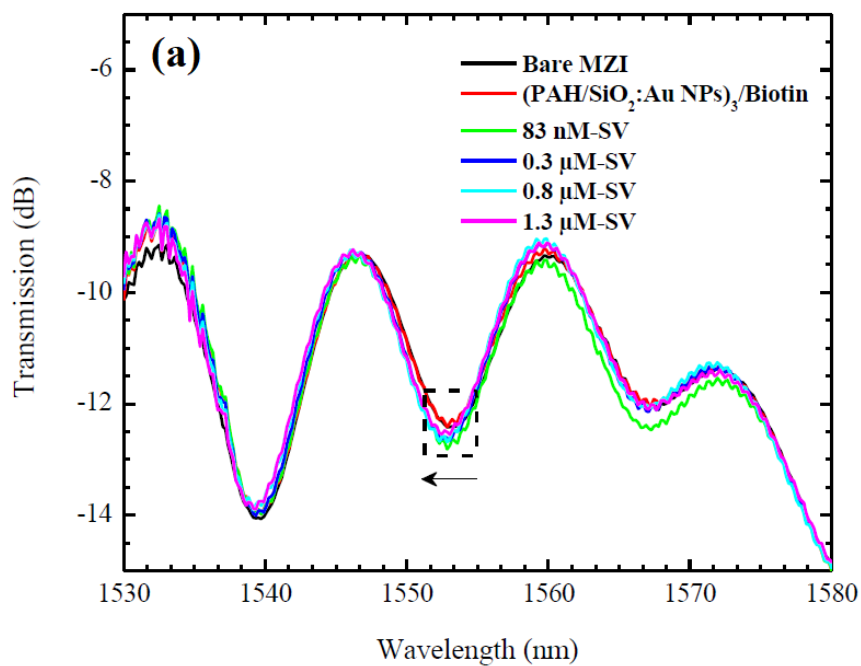


Figure 1.15 (a) Transmission spectra of tapered MZI before and after coating  $(\text{PAH}/\text{SiO}_2:\text{Au NPs})_3/\text{Biotin}$ , and (b) at  $\lambda = 1553.22 \text{ nm}$  (Reprinted from [67], with permission).

In this case, the sensitivity for the biosensor is calculated by the formula [68]:

$$S = \frac{\Delta\lambda_{max}}{\sigma}, \quad (1.12)$$

where  $\sigma$  is the surface density of the detected biomaterial (Streptavidin protein) given by  $\sigma = 6.23 \text{ ng/mm}^2$ , and  $\Delta\lambda_{max}$  is the highest wavelength shift observed during the experiment. For this case,  $\Delta\lambda_{max}$  was 0.36 nm; therefore, the sensitivity is  $0.07 \text{ nm}/(\text{ng/mm}^2)$  [67].

### 1.5.2 Biosensor coated with (PAH/PSS)<sub>3</sub>/Biotin

In the second case, the same structure was coated with three bilayers of PAH/PSS and Biotin. First, the transmission spectrum was collected for the bare MZI in water, then for the coated structure. Finally, the protein concentrations were added to the system, similar to the previous case. The spectrum shift for coated bilayers was  $0.81 \pm 0.01 \text{ nm}$ , towards shorter wavelengths. It is essential to mention here that the new position for the resonance wavelength obtained after coating was the reference point for the following steps. The addition of protein at 83 nM concentrations shifted this spectrum by a further  $0.72 \pm 0.01 \text{ nm}$  towards shorter wavelengths again. Increasing the concentration to 300 nM increased this blueshift by  $0.81 \pm 0.01 \text{ nm}$ . Adding more protein at a concentration of 800 nM to the solution caused a  $1.44 \pm 0.01 \text{ nm}$  shift towards shorter wavelengths. Finally, increasing the SV concentration to 1300 nM shifted the resonance wavelength by  $1.80 \pm 0.01 \text{ nm}$ . All these results are summed up in Fig. 1.16. The resulting sensitivity for this biosensor was  $S = 0.29 \text{ nm}/(\text{ng/mm}^2)$ , which is almost four times greater than in the (PAH/SiO<sub>2</sub>:Au)<sub>3</sub>/Biotin coated biosensor. Table 1.1 shows the shifts in the resonance wavelength of two types of

biosensors transmission spectra resulting from the addition of different protein concentrations [67].

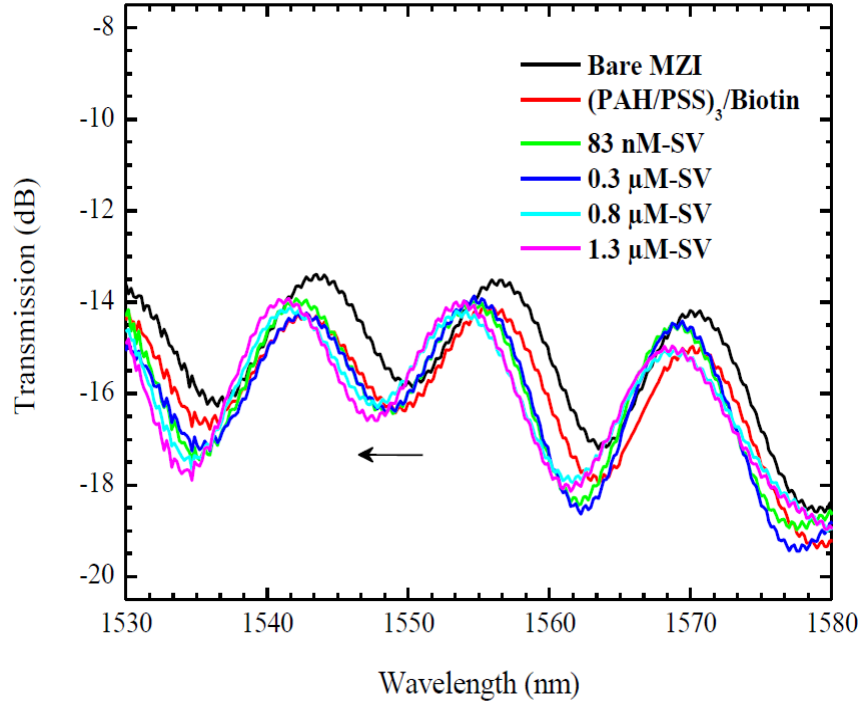


Figure 1.16 Transmission spectra of tapered MZI before and after coating  $(\text{PAH/PSS})_3/\text{Biotin}$ , as well as their exposure to streptavidin solutions of different concentrations (reprinted from [67], with permission).

Table 1.1 Resonance wavelength shifts due to the different concentrations of protein.

Structure of the sample	Wavelength shifts (nm) in transmission spectrum with concentration of SV added at:			
	83 nM	300 nM	800 nM	1300 nM
$(\text{PAH/SiO}_2:\text{Au})_3/\text{Biotin}$	0.18	0.27	0.36	0.27
$(\text{PAH/PSS})/\text{Biotin}$	0.72	0.81	1.44	1.80

## 1.6 A brief introduction to COMSOL Multiphysics software

For this thesis, experimental results will be simulated using COMSOL Multiphysics 5. The main problem-solving method of the COMSOL software is finite element analysis (FEA). This method uses numerical techniques to find an approximate solution to the various problems. The numerical approach applies partial differential equations that can be solved using numerical integrations to achieve reasonably close to exact answers. This method has been used for solving problems in optics, thermal physics, solid mechanics, dynamics, and so on.

In general, COMSOL software first examines a problem and simplifies it as a geometrical model. The next step is to design the model. For every component in the COMSOL, the material must be identified. The most important steps when using a COMSOL code are determining the boundary conditions and meshing the structure. Each user-defined interface has its mathematical formalism and functions. COMSOL software solves problems using FEA, which divides the geometry into several pieces called meshing. Below, we summarize the procedures [69]:

- **Discretize the continuum:** the primary step is to divide the problem geometry into finite elements. In COMSOL software, the operator determines the division using prepared patterns. Meshing quality ranges from extra-coarse to finest.
- **Select interpolation functions:** as is evident by the name, interpolation functions must interpolate variables over elements. Usually, polynomials are selected as interpolation functions. This step is done automatically by the COMSOL software.

- **Find the element properties:** in this step, matrix equations are established. These equations relate the nodal values of interpolation functions of one element to these values of other elements. In other words, the values of functions on boundaries of elements are achieved, compared together, and saved for the next steps. This step is done by the COMSOL software as well.
- **Assemble the element equation:** in this step, all separate element equations are assembled. The result is to achieve a global equation system for the entire solution region. In other words, all discretized local element equations are combined to form a global equation. In COMSOL software, assembling local element equations takes place after determining the boundary condition. In this study, the boundary condition is the scattering boundary type.
- **Solve the global equation system:** after assembling the element equations and forming a global one, the software solves the equation, thereby achieving the desired functions. Since COMSOL software is a graphical software, this step takes time, depending on the problem's meshing quality.
- **Compute additional results:** in this study, in addition to solving Maxwell's equations, obtaining other information such as strain or stress is required. For this step, COMSOL software facilities are used to obtain this information.

## 1.7 Thesis outline

The present thesis consists of 5 chapters. The content of subsequent chapters is as follows:

Chapter 2 discusses the experimental details used to construct LPG on standard single-mode fiber. The chapter introduces the electric arc discharge technique used for this thesis and analyzes prepared samples in terms of average micro-taper diameters.

Micro-tapering simulations are examined in Chapter 3. The acquirement of different simulation results on tapered fiber and the analysis of the experimental results through simulation are also explained. The simulation of LPG as a sensor for environmental refractive index and temperature is also discussed and reported in the chapter.

Chapter 4 reports on simulations based on experiments performed for measuring Streptavidin protein concentrations, using a single tapered fiber and in-line tapered fibers as MZI.

Chapter 5 presents the conclusions of the research performed in this study and summarises the results.

## **Chapter 2 Experimental details**

This study uses the electric arc discharge (EAD) method for LPG fabrication. The first step of the fabrication processes consists of placing an uncoated fiber between the electrodes of a fiber fusion splicer. One side of the fiber is affixed with a piece of tape in a fiber holder on top of a micro-stepper. A weight is attached to the other side of the fiber to maintain the fiber at a constant axial tension. In the second step, an arc discharge, controlled by specific arc current magnitude and arc duration, is applied on a small segment (several hundred micrometers in length) of the fiber. In the third step, the fiber is moved by the grating period, typically 400-800  $\mu\text{m}$ . A pulley is used to facilitate fiber movement, as

shown in Fig. 2.1 (a). Exposure of the fiber to the electric arc in sequence with a specific periodicity may lead to the emergence of loss peak(s) in the transmission spectrum of the fiber. Since both ends of the fiber are accessible, it is possible to carry out in-situ spectral monitoring during the grating writing, enabling simultaneous characterization of the fiber during grating fabrication.

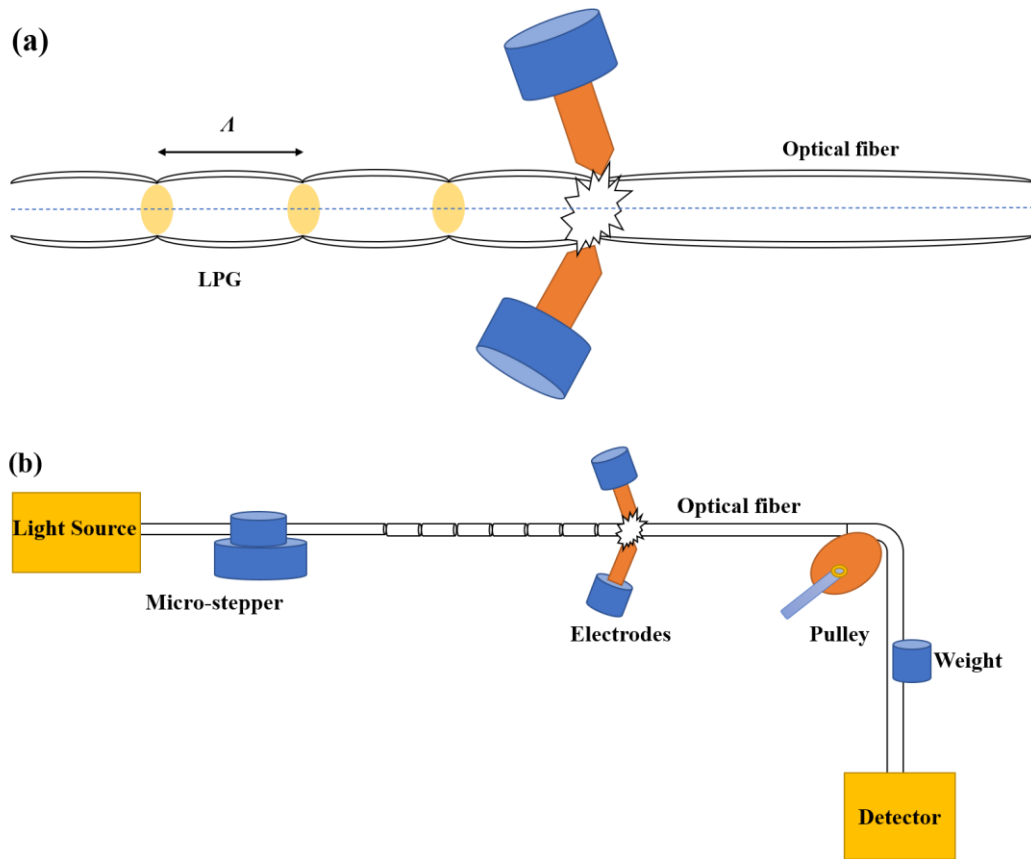


Figure 2.1 Fabrication of LPG in this study: (a) use of arc discharge to write LPG on the fiber, (b) setup for fabricating LPG on the fiber.

## 2.1 General fabrication processes using electric arc discharge method

A standard single-mode optical fiber (Corning SMF 28e), which exhibits low loss in the infrared region, is determined to be suitable for writing LPG in this study. The maximum

attenuation of this fiber at the telecommunication wavelength of 1550 nm is 0.18 dB/km [70]. The diameters of its cladding and core are 125 and 10  $\mu\text{m}$ , respectively [70]. For all samples in this study, fiber length is set at one meter, and the transmission spectrum is monitored with an optical spectrum analyzer. The one-meter fiber is stripped using a fiber stripper in a location near the middle to remove the plastic jacket. The stripper removes most of the jacket, although some tiny plastic or glass particles remain. Wiping with an ethanol-soaked napkin clears the fiber part effectively where the jacket has been removed.

The following procedures are adopted to assemble the setup using a fiber fusion splicer (Yokogawa, FITEC Model S182A), as shown in Fig. 2.1(b). Figure 2.2 shows the fiber fusion splicer used in this study, including two movable stages, ZL and ZR, V-grooves where the fiber is positioned, and two electrodes that generate an electric arc discharge. The section of fiber with the jacket removed is placed in the V-grooves. Also, Fig. 2.3 shows these components schematically. One side of the fiber is attached to a micro-stepper with a translation precision of 30.75  $\mu\text{m}$  (0.00125 inches). The fiber is connected to a

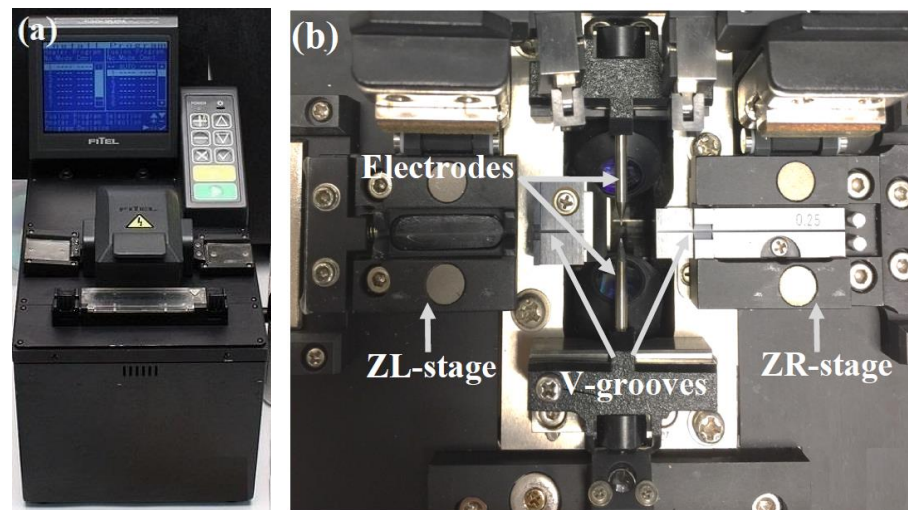


Figure 2.2 Fusion splicer used in this study (FITEC S182A): (a) the instrument with display and keyboard; (b) electrodes, V-grooves, and fiber holders as the key components of the instrument.

weight on the other side to induce tension along the fiber. Regulating the fusion splicer in the manual state makes it possible to set the arc current and the arc duration through the fusion splicer panel.

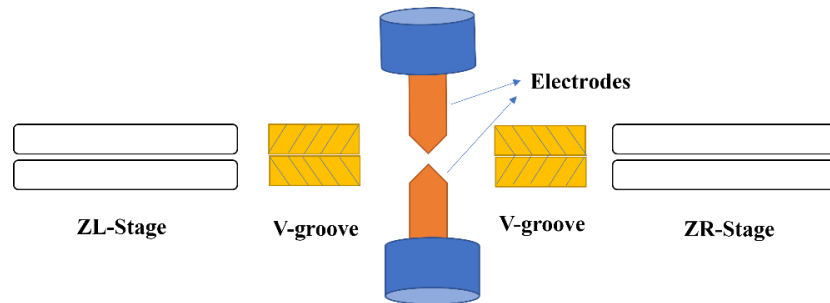


Figure 2.3 Schematic illustration of fusion splicer components used in this study.

Figure 2.4 shows the complete setup in the lab for LPG fabrication in this study. By setting the fusion splicer parameters and changing the tension in the fiber through adjusting the mass of the attached weight, writing LPG on the fiber in a controlled manner becomes feasible. The writing is accomplished with an arc current and arc duration set at 5 mA and 150 ms, respectively, with a tension of 12.5 mN (milli-Newton) (a mass of 1.275 g). One micro-taper for every discharge is expected. There is a wait time between every

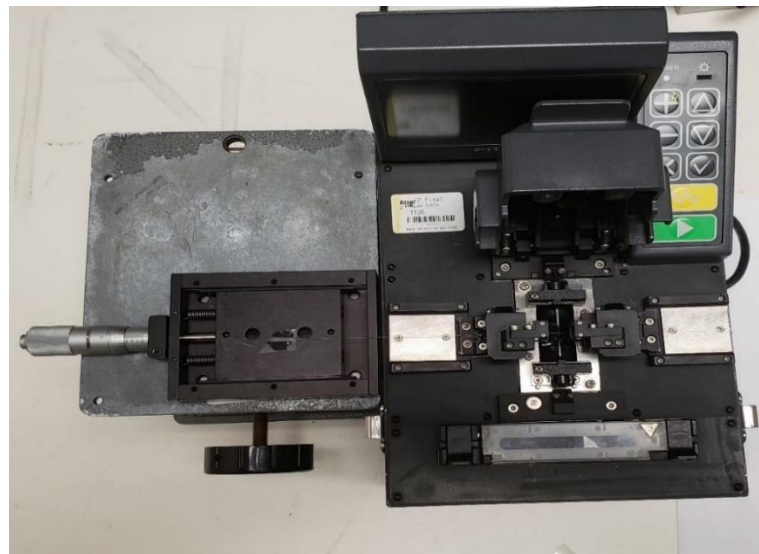


Figure 2.4 Complete setup for LPG writing on a single-mode optical fiber.

discharge, depending on the arc current and the arc duration. The wait time is varied from 30 to 90 minutes during the writing process. There is always a possibility that any discharge can break the fiber if the wait time is not carefully monitored. In the next section, the effects of various fabrication parameters, such as arc current, arc duration, and tension, will be investigated experimentally with this setup to reveal the physical mechanisms governing fabrication and the resulting properties, compared with what is achieved through simulation.

## **2.2 Sample preparation**

### **2.2.1 Variation of arc current**

The influence of the magnitude of arc current is investigated by fabricating samples with different arc current values, while other parameters, such as arc duration and tension, remain unchanged. In order to construct Sample #1, an arc current of 5 mA and arc duration of 150 ms are chosen, with a tension of 12.5 mN. The selection of optimum values for these experiments is judiciously evaluated to prevent damage to the sample. However, in order to form a pronounced transmission spectrum for the LPG, such as that shown in Fig. 1.14, several tens of microstructures are required to generate the spectrum. An optical image of the achieved sample is shown in Fig. 2.5. The raw transmission spectrum for this structure can be found in Fig. 2.6, which shows a resonance wavelength at around 1542 nm. Due to the low arc current (5 mA), the refractive index modulations are not such high for exciting  $LP_{02}$ . Therefore, the  $LP_{01}$  is the only appearing mode in the range between 1494 to 1594 nm. Note that in the raw transmission spectrum, the background noises or transmission spectrum regarding the light source are included in the final spectrum. Other noises in the

Fig 2.6 as well as a dip at around 1580 nm, is not related to the sample but represents a background noise relevant to the light source. As mentioned before, since the arc current amount is pretty low (5 mA), for producing a pronounced transmission spectrum, the number of gratings is set to be 100 with a periodicity of  $508 \pm 15 \mu\text{m}$ . The average diameter of the resulting micro-tapered sections along the LPG, measured using a micro-meter on the optical microscope display, is  $110 \pm 1 \mu\text{m}$ .

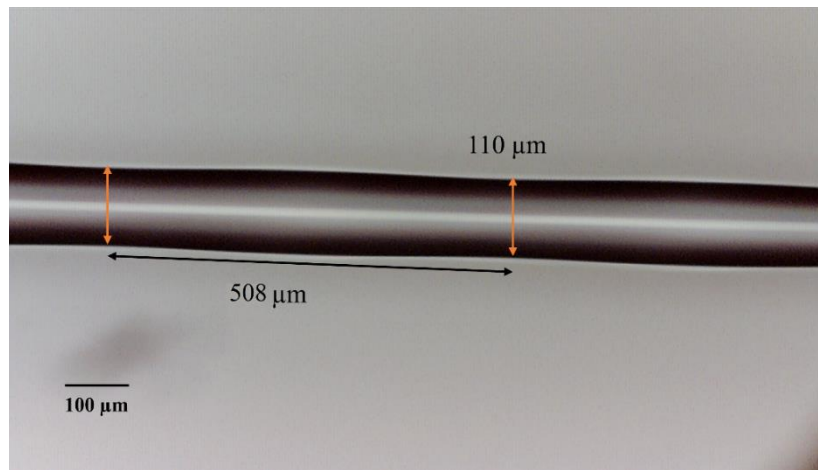


Figure 2.5 Arc discharge written LPG in SMF: arc current, 5mA; arc duration, 150 ms; tension, 12.5 mN.

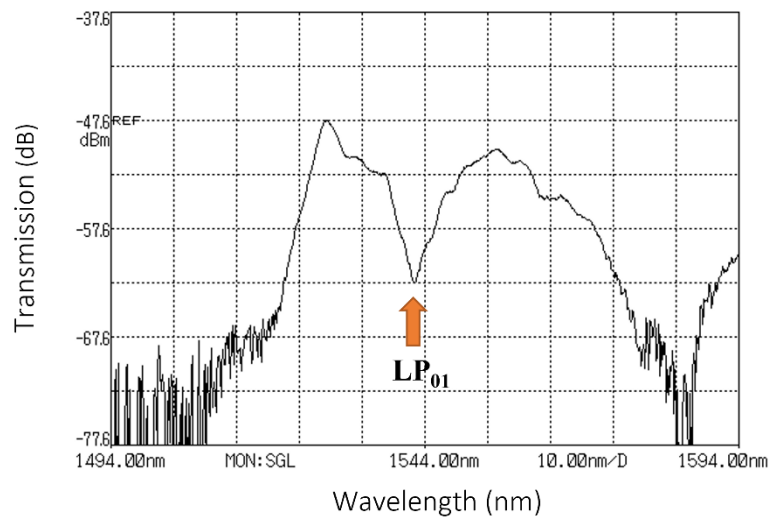


Figure 2.6 Raw transmission spectrum of arc discharge-written LPG in SMF: arc current, 5mA; arc duration, 150 ms; tension, 12.5 mN; periodicity of grating,  $762 \mu\text{m}$ ; number of gratings, 100.

It is essential to mention that the formation of micro-tapers results from deformation on the fiber surface due to the melting and stretching processes, not a result of material removal. There are two leading causes for material removal: vaporization and etching. Since the boiling point of the silica glass (single-mode fiber main material) is 2230°C [74], the glass vaporization cannot play a role here, because the maximum temperature produced by the transferred heat at the arc discharge position is 1300°C [73]. Also, the arc discharge is not strong enough to etch the fiber surface [73].

Sample #2 is fabricated with an arc current of 10 mA. The average micro-tapered diameter is about  $105 \pm 1 \mu\text{m}$ . In order to achieve a spectrum pattern exhibiting pronounced grating features, the arc discharge process is continued until the grating number reaches 70. Figure 2.7 shows the morphology of this sample with a periodicity of  $508 \pm 15 \mu\text{m}$ .



Figure 2.7 LPG written in SMF: arc current, 10 mA; arc duration, 150 ms; tension, 12.5 mN.

The raw transmission spectrum of this sample without background subtraction is shown in Fig. 2.8. In this case, due to the higher arc current (10 mA), the decrease in the effective refractive index difference of the fiber core and cladding is significant so that in addition to LP<sub>01</sub> mode in the range between 1493 to 1593 nm, the LP<sub>02</sub> mode is appeared as well. The figure indicates two resonance wavelengths, one at around 1539 nm, and the other around 1555 nm. Like the previous case, the background noise in the same position of around 1580 nm also appears here. In fact, the unchanged position of these dips in Figs 2.6 and 2.8 is the main reason for being as background noise.

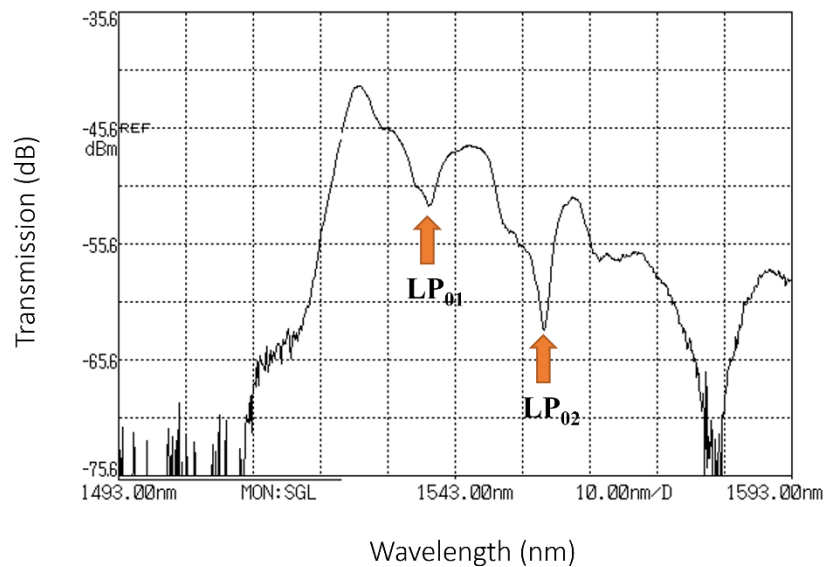


Figure 2.8 Raw transmission spectrum of arc discharge-written LPG in SMF: arc current, 10 mA; arc duration, 150 ms; tension, 12.5 mN; periodicity of grating, 508  $\mu\text{m}$ ; number of gratings, 70.

Sample #3 is fabricated with an arc current of 15 mA, with fixed values for the arc duration (150 ms) and tension (12.5 mN). The fabricated component is shown in Fig. 2.9. The figure indicates that the average diameter for the micro-tapered sections is smaller than

that of Sample #2 ( $99 \pm 1 \mu\text{m}$ ). The periodicity and the gratings number of Sample #3 exhibited in Fig. 2.9 are  $508 \pm 15 \mu\text{m}$  and 30, respectively.



Figure 2.9 LPG fabricated in SMF with an arc current of 15 mA, arc duration of 150 ms, tension of 12.5 mN, and grating periodicity of  $508 \mu\text{m}$ .

Sample #4 is fabricated using an arc current of 20 mA, while the other parameters are maintained at the same values as those for previous samples. The average micro-tapered diameter is  $91 \pm 1 \mu\text{m}$ , and the grating number is 15. Unfortunately, the number of gratings, 15, is insufficient to yield an excellent spectral pattern. In previous samples (Samples #1, #2, and #3), the arc current magnitudes are not such high to break samples. However, when the arc current magnitude exceeded 15 mA, no successful results are achieved for microstructure numbers over 15 due to the high heat transfer to the fiber resulting from the arc discharge [71]. Figure 2.10 shows the resulting structure when the arc current is 20 mA.

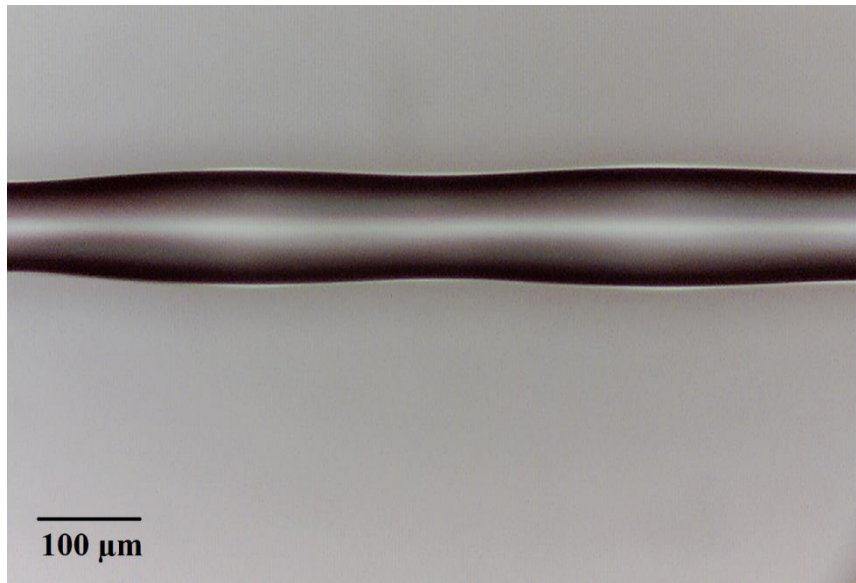


Figure 2.10 Microstructures fabricated in SMF with an arc current of 20 mA, arc duration of 150 ms, and tension of 12.5 mN.

Sample #5 is fabricated at an increased arc current of 25 mA. Although the number of gratings can not exceed more than 15, which is not enough to have a concrete transmission spectrum, the resulting structure can be analyzed using geometrical analysis. It would appear that an arc current exceeding 15 mA is too strong to create an LPG on SMF due to the high heat transfer from the arc discharge to the fiber structure [71], making its structure too weak for the existing tension along the fiber. Figure 2.11 shows the resulting structure in this case. The figure indicates that the average diameter of the micro-tapered sections is small ( $86 \pm 1 \mu\text{m}$ ) in comparison to cases with lower arc currents.

For an arc current larger than 25 mA, LPG fabrication in the fiber is not possible because high-temperature discharges would melt the fiber at the arc location, and the existing tension along the fiber would become unbearable for the fiber structure [71].

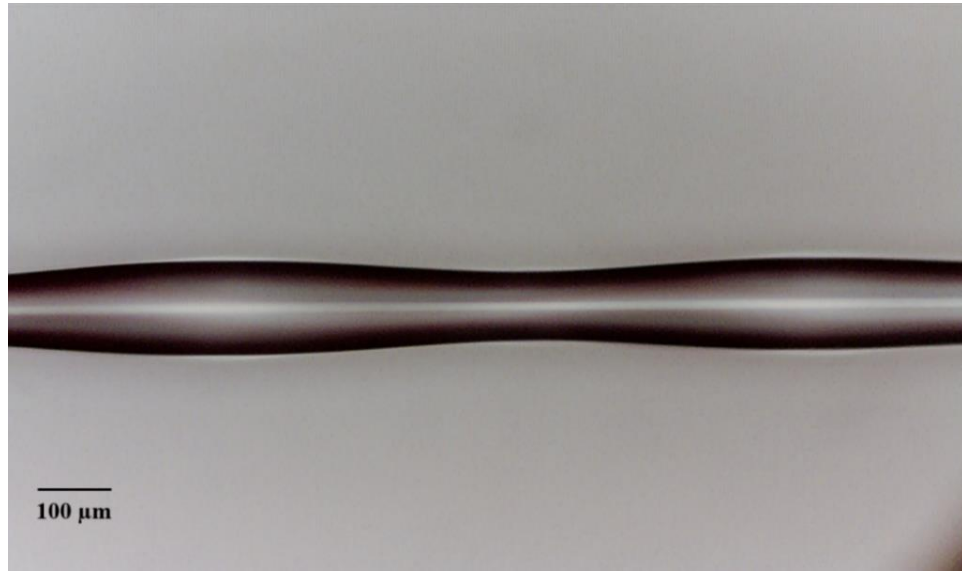


Figure 2.11 Microstructures fabricated in SMF with an arc current of 25 mA, arc duration of 150 ms, and tension of 12.5 mN.

Varying the arc current applied to the sample indicates an upper limit of 25 mA. Note that for Samples #1 and #2, the number of gratings is continued until the concrete transmission spectrum is achieved. For samples #3, #4, #5, the maximum number of gratings is reported right before the breaking of the sample. Table 2.1 shows a summary of the resulting samples made by arc current variations. Since the geometrical analysis can be done using both successful and unsuccessful samples, Table 2.1 includes either successful or unsuccessful samples.

Table 2.1 Samples obtained from arc current variations while arc duration and tension remain constant at 150 ms and 12.5 mN. The uncertainty of the average diameter is 1 μm.

Parameters	Sample #1	Sample #2	Sample #3	Sample #4	Sample #5
AC (mA)	5	10	15	20	25
Average diameter (μm)	110	105	98.5	91.25	85.83

### 2.2.2 Variation of arc duration

The following set of samples is produced to investigate the impact of varying arc durations on the LPG fabrication process. The arc duration is changed from 150 to 450 ms, while the arc current and tension are fixed at 10 mA and 12.5 mN, respectively. Sample #1 is produced with a 10 mA arc current, a 150 ms arc duration, and a 12.5 mN tension, as discussed in Section 2.2.1. Sample #2 is produced using a 250 ms arc duration with fixed values for the arc current and the mass. The periodicity and number of gratings are  $762 \pm 15 \mu\text{m}$  and 20, respectively. The average diameter of the micro-tapers in this sample is  $101 \pm 1 \mu\text{m}$ . Sample #3 in this group is produced when the arc duration is increased to 350 ms. The average micro-tapers diameter is found to be smaller in comparison with the former case. Also, due to the higher arc duration, wait times between each discharge are longer. 1.25 hours is the average wait time for Sample #3. The micro-tapered diameter and the periodicity of this sample are  $97 \pm 1 \mu\text{m}$  and  $508 \pm 15 \mu\text{m}$ , respectively. Sample #4 in this group is produced using a 450 ms arc duration. The average micro-tapered diameter is  $94 \pm 1 \mu\text{m}$ . For an arc duration longer than 450 ms, the fiber is found to break. Table 2.2 lists the samples produced when the arc duration varied from 150 to 450 ms.

Table 2.2 Samples fabricated with different arc durations set in the fiber fusion splicer (arc current: 10 mA, tension: 12.5 mN). The uncertainty of the average diameter is  $1 \mu\text{m}$ .

Parameters	Sample #1	Sample #2	Sample #3	Sample #4
Arc duration (ms)	150	250	350	450
Average diameter ( $\mu\text{m}$ )	105	100.5	97.5	93.5

### 2.2.3 Variations of tension

The last set of samples is produced to investigate the result of changes in the tension supplied using weight attached to the fiber. As illustrated in Fig 2.12, since the tension along the fiber is equal to the gravity force of the hanging weight ( $T = mg$ ), the mass used for sample fabrication is reported as tension. Sample #1 is produced using 10 mA, 250 ms, and 12.5 mN (1.275 g) for the arc current, arc duration, and tension (mass), respectively, as discussed in Section 2.2.2. Sample #2 in this group is obtained when the tension is increased to 16.7 mN (1.7 g). The average micro-tapered diameter is  $95 \pm 1 \mu\text{m}$ . The last sample in this group, #3, is obtained when the tension is increased to 24.5 mN (2.5 g). The average micro-taper diameter for this sample is  $89 \pm 1 \mu\text{m}$ . Table 2.3 lists all samples in this group.

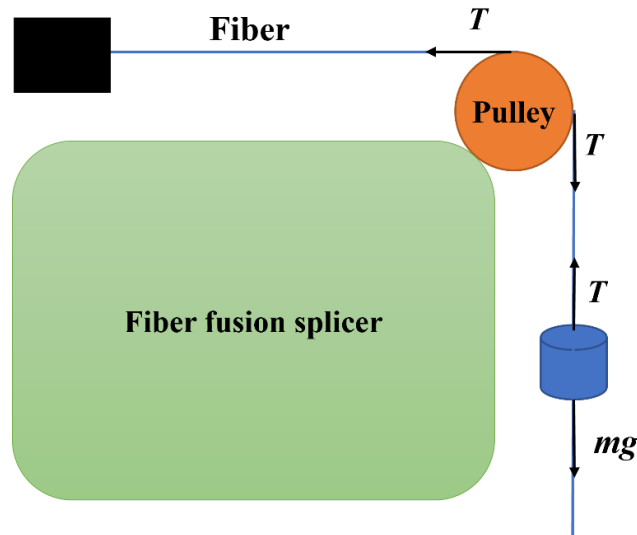


Figure 2.12 The free body diagram of the fiber and hanging mass. The tension along the fiber equals the gravity force of the mass ( $T = mg$ ).

Table 2.3 Samples fabricated with a different tension set in the fiber fusion splicer (arc current: 10 mA, arc duration: 250 ms). The uncertainty of the average diameter is 1  $\mu\text{m}$ .

Parameters	Sample #1	Sample #2	Sample #3
Tension (mN)	12.5	16.7	24.5
Average diameter ( $\mu\text{m}$ )	105.0	94.75	88.75

In general, due to the high effect of tension on fiber tapering, there is a limited possibility for tension variations. An arc discharge using 10 mA arc current in a duration of 250 ms prepares highly heat transferred to the fiber structure, which is unbearable for the fiber under tensions greater than 24.5 mN. Therefore, the number of samples that can be manufactured is limited to three for the tension variation.

### 2.3 Geometric properties of micro-tapered fibers

After the micro-tapered fibers are fabricated, their geometric properties are investigated to explore their effect on spectral properties. The first part of the experiment is carried out while the arc duration and tension are fixed at 150 ms and 12.5 mN, respectively, with the arc current varying from 5 to 25 mA. As can be seen from Table 2.1, the average diameter of the fiber taper fabricated at 5 mA is  $110 \pm 1 \mu\text{m}$ , while this value is  $105 \pm 1 \mu\text{m}$  when fabricated at an arc current of 10 mA. The average diameters of micro-tapers produced at arc currents of 15, 20, and 25 mA are  $99 \pm 1$ ,  $91 \pm 1$ , and  $86 \pm 1 \mu\text{m}$ , respectively. Figure 2.13 demonstrates that, as the arc current increases, the average diameter of micro-tapers experiences a linear decrease. A linear regression model indicates that for each unit

increase in the arc current, fiber diameter decreases by 1.24  $\mu\text{m}$ , while the other parameters remain constant.

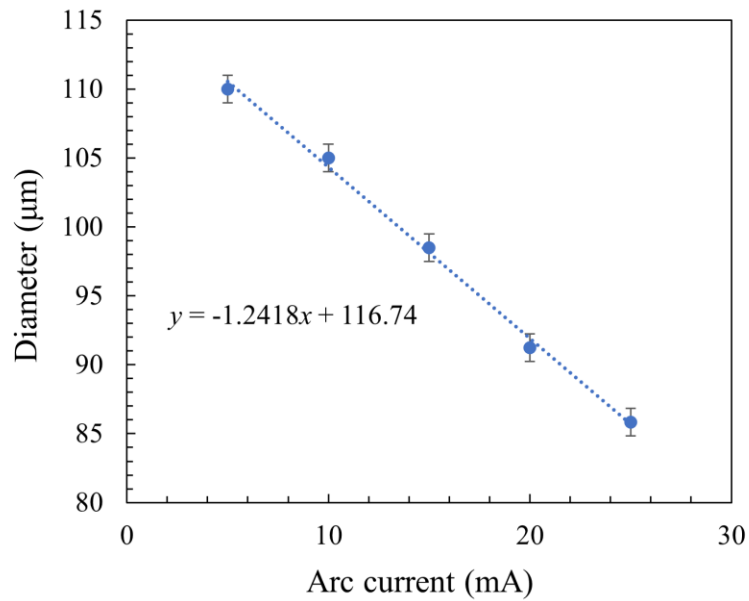


Figure 2.13 Dependence of micro-taper diameter as a function of arc current strength.

Also, by fixing the arc current and tension values at 10 mA and 12.5 mN, respectively, the effect of arc duration variations is studied. As shown in Fig. 2.14, the trend again indicates a downward linear fit. A linear trend with a negative slope shows that the average diameter of micro-taper fabricated along the fiber decreases as the arc duration increases, while the arc current and mass remain constant.

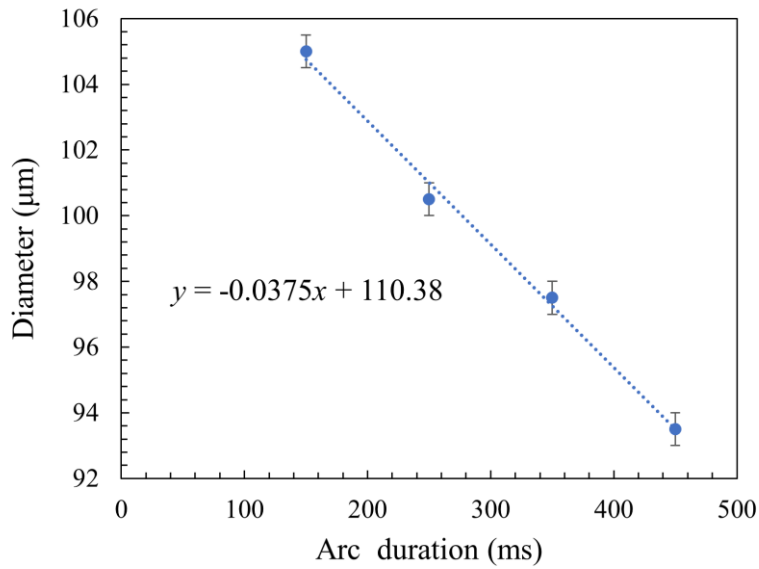


Figure 2.14 Dependence of micro-taper diameter as a function of arc duration.

Finally, the same investigations are conducted for tension variations while the arc current and the arc duration are fixed at 10 mA and 250 ms, respectively. As shown in Fig. 2.15, the average diameter of the micro-tapers decreases nonlinearly when the tension increases. Since the number of data is less than four, the connecting line is not displayed.

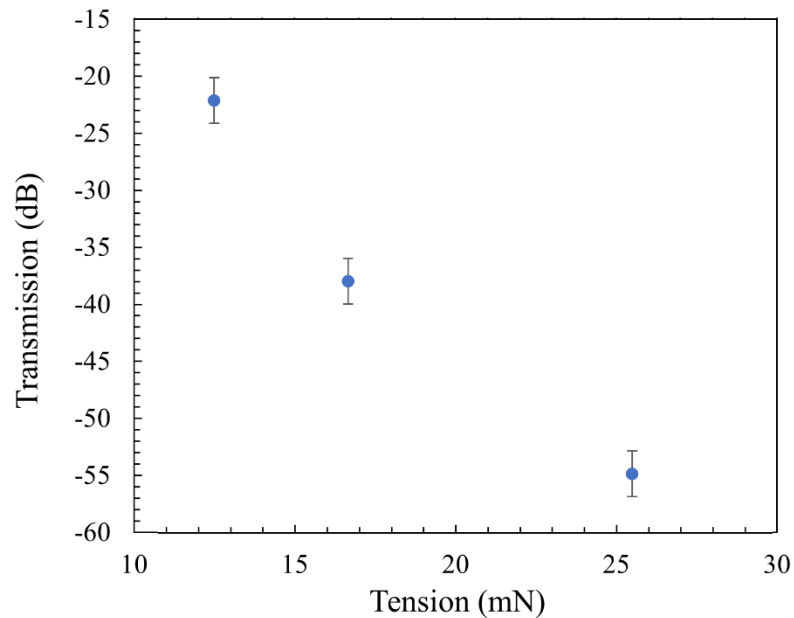


Figure 2.15 Dependence of the diameter of micro-taper as a function of mass.

In general, during the arc discharge process, the heat transferred to the fiber is linearly proportional to the discharge power ( $P$ ) and the arc duration ( $t$ ), as follows [72]:

$$Q = Pt. \quad (2.1)$$

As the voltage difference between electrodes is almost constant, 500-600 V for such fiber fusion splicer in this study [72], discharge power is essentially proportional to the arc current ( $P = VI$ ). Therefore, the heat transferred to the fiber is linearly proportional to the arc current and the arc duration. As a result, any increase in the arc current or arc duration causes a linear increase in the heat transferred to the fiber structure. Hence, deformation on the fiber structure can also be linear since the tension along the fiber is fixed at a constant value. However, as will be discussed in Chapter 3, Section 3.2, since the glass fiber is a type of viscoelastic material, increasing the tension exerted on the fiber cross-section (stress) causes a non-linear deformation in the fiber structure while the heat transferred to the fiber is constant (the arc current and arc duration remain unchanged) [74].

This chapter discusses writing LPG on the single-mode fiber using the EAD method and the effect of variations in its fabrication parameters. The diameter of the micro-tapers decreases by 1.24  $\mu\text{m}/\text{mA}$  when the arc current is increased and while the arc duration and tension on the fiber are fixed. Expanding arc duration produced the same results. The slope of the variation is found to be -0.037  $\mu\text{m}/\text{ms}$ . The last parameter is the tension along the fiber, controlled by hanging weights attached to the fiber. When the tension is increased while other parameters are kept constant, the average diameter of the micro-tapers decreases nonlinearly.

## **Chapter 3 Simulation on the formation and application of long-period gratings**

### **3.1 Micro-taper analysis using two methods in COMSOL®**

This chapter discusses the formation and characteristics of tapered fibers and arc-induced long-period gratings (LPG). First, the most suitable method for solving problems in COMSOL Multiphysics software must be chosen, which is the main topic of this section. To find the most appropriate approach for this study, electric field analysis of the tapered fiber will be carried out using two different methods: the frequency domain method and the beam envelope method. All other quantities, such as magnetic field ( $\mathbf{B} = \mathbf{E}/c$  where  $\mathbf{B}$ ,  $\mathbf{E}$ , and  $c$  are magnetic field vector, electric field vector and the speed of light in free space,

respectively), and light intensity (Subsection 3.1.2), can be obtained directly from the electric field.

In COMSOL Multiphysics, any electromagnetic wave problem is solved by constructing a model composed of domains and boundary conditions. Within the domains, material models are used to represent a wide range of substances. However, from a mathematical perspective, all these materials are dealt with nearly identically within the governing equations, which are Maxwell's equations in this study (as mentioned in Section 1.1)

In the wave optics module in COMSOL Multiphysics, simulations of light propagation in an extensive optical system are challenging due to the complexity of mesh element size optimization for solving Maxwell's equations for an optical system with massive dimensional variations in dimensions. Note that the domain is split into a discrete number of elements in the meshing process for which the solution can be calculated. In the wave optics module, Maxwell's equations are solved for the fields using the equation of  $\mathbf{E}(\mathbf{r}) = \mathbf{E}_1(\mathbf{r})e^{-i\mathbf{k}\cdot\mathbf{r}}$  (where  $\mathbf{E}_1$  is the field amplitude vector and  $\mathbf{k}$  is the wave vector) in two different methods. The full-wave method involves solving Maxwell's equations from scratch to obtain the amplitude and wave vector ( $E_1, \mathbf{k}$ ). The corresponding simulation is extremely difficult and time-consuming, which requires significant memory in computation. In the beam envelope method, in case the wave vector is known, the solution can be downgraded to find the wave amplitude only. Since the wave vector is the fast oscillation part that moves around the phase velocity ( $V_p = \omega/k$ ), determining it before compiling the code will significantly simplify obtaining the solution because the electric

field's envelope (or amplitude) part slowly varies. Therefore, there is no need to solve the entire equation.

These different procedures influence the number and size of the mesh elements. The size of the mesh elements used in the full-wave method is in the order of the wavelength because the problem is solved directly for the full-wave, thereby increasing the number of the mesh elements significantly. Small-sized and large-number mesh elements will affect the computation time and memory resources required to complete the calculations. However, since the expected result of the beam envelope method is an electric field amplitude, the number of mesh elements used for large structures can be reduced significantly. The needed memory and the simulation time depend on the number of mesh elements, which can substantially influence the computational requirements of the simulation.

In this study, the tapered fiber is simulated using both methods. However, as mentioned above, in order to decrease the computational cost when using the full-wave method, the fiber dimensions are chosen to be almost five times smaller than in the actual system. Due to the decrease in dimensions on the modeled structure in the full-wave method, the transmission spectrum of the propagating light through the structures will not be comparable since this parameter depends on the length and waist of the tapered fibers, as discussed in Section 4.2. Therefore, the difference in the electric field amplitude of the propagating light in the fiber input and output for each method will be discussed.

### 3.1.1 Simulation on the tapered fiber using the full-wave method

As mentioned in Section 1.6, COMSOL uses the finite element method to solve electromagnetic fields within modeling domains. When the material properties are linear with respect to the field strength and the field varies sinusoidally in time at the angular frequency  $\omega=2\pi f$ , the governing Maxwell's equations in three dimensions can be reduced to [3]:

$$\nabla \times (\mu_r^{-1} \nabla \times \mathbf{E}) - \frac{\omega^2}{c^2} \left( \epsilon_r - \frac{i\sigma}{\omega\epsilon_0} \right) \mathbf{E} = 0, \quad (3.1)$$

where  $\mu_r$ ,  $\epsilon_r$ , and  $c$  are relative permeability, relative permittivity, and the speed of light in free space, respectively, and  $\sigma$  is the electrical conductivity of the material. The above equation is used to obtain the electric field of propagating light for the tapered fiber shown in Fig. 3.1. However, the dimensions chosen are almost five times smaller than the actual fiber due to limitations in the simulation tools (the length of the tapered fiber is decreased more). The modeled fiber geometry includes two rectangles as the core and the cladding in the regular fiber section and four half-ellipses in the tapered section.

The diameters of the fiber core and cladding are set to be 25 and 2.5  $\mu\text{m}$ , respectively, and both have a length of 40  $\mu\text{m}$  along the longitudinal direction. The tapered section in the cladding is formed by two ellipses, with its major axis representing the length of the tapered section, while its minor axis stands for the depth of the taper. The same denotation is applied for the core region as well. In the next step, the properties of the different segments or domains in the structure are determined. The fiber core and cladding refractive indices are set to be 1.4457 and 1.4378, respectively [70]. In the full-wave

method section on the code, the boundary type is chosen as a scattering boundary condition due to the power loss through the boundaries during light propagation in the fiber taper. In the electromagnetic wave module in COMSOL software, "port" is the location where the electromagnetic wave enters or exits the structure to be modelled. Therefore, two numeric ports at the input and output of the structure are determined. The meshing process is done using an "extremely fine" type of mesh. Due to the presence of two numeric ports, two "boundary mode analyses" must be added to the "Study" section and run the code for modeled structure. By adding two cut lines through the "Datasets" section to the code using the start and end locations of the structure, obtaining the input and output electric field amplitudes of the wave propagating along the fiber becomes feasible. In Fig. 3.1, the input is at the left end of the fiber that receives the input electromagnetic wave, while the output is at the right end.

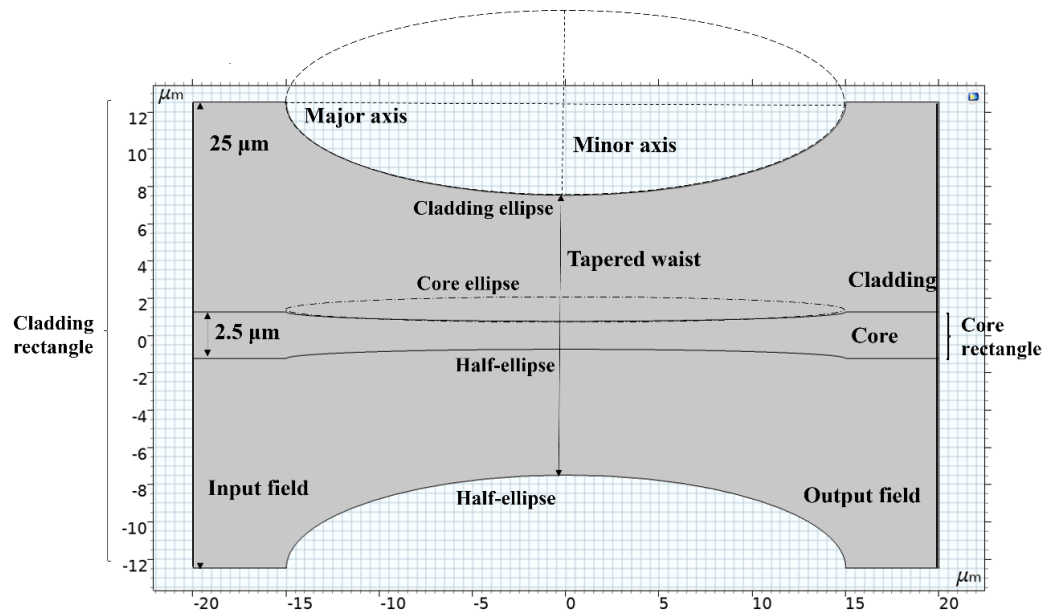


Figure 3.1 Geometry of a single-mode fiber modeled in the full-wave simulation. The dimensions are much smaller than those of the actual fiber.

Figure 3.2 indicates the electric field amplitude of the input wave, which is the same for all tapers with different waists. Clearly, most of the light propagates through the fiber core. However, due to the small diameter of the core, part of the propagating light penetrates to the fiber cladding.

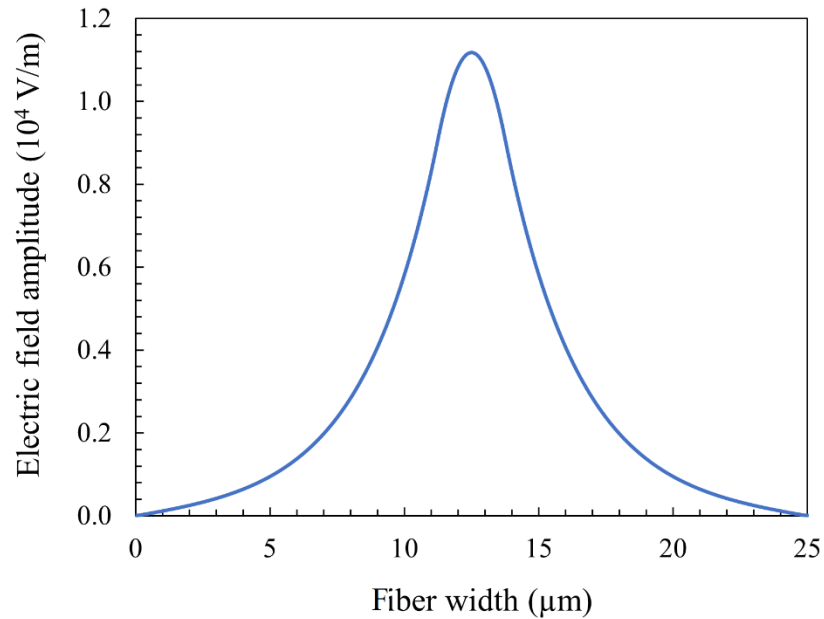


Figure 3.2 Input electric field amplitude achieved from full-wave simulation for a tapered fiber.

Figure 3.3 illustrates the output electric field amplitude of the propagating wave along the fiber tapers, which show two different waist thicknesses,  $25 \mu\text{m}$  (no tapering) and  $5 \mu\text{m}$ . The electric field amplitude decreases during its propagation from the input to the output end. When the wave passes through the tapered section, it partly penetrates the cladding section at the waist, loses some of its strength, and exhibits different amplitudes at the output.

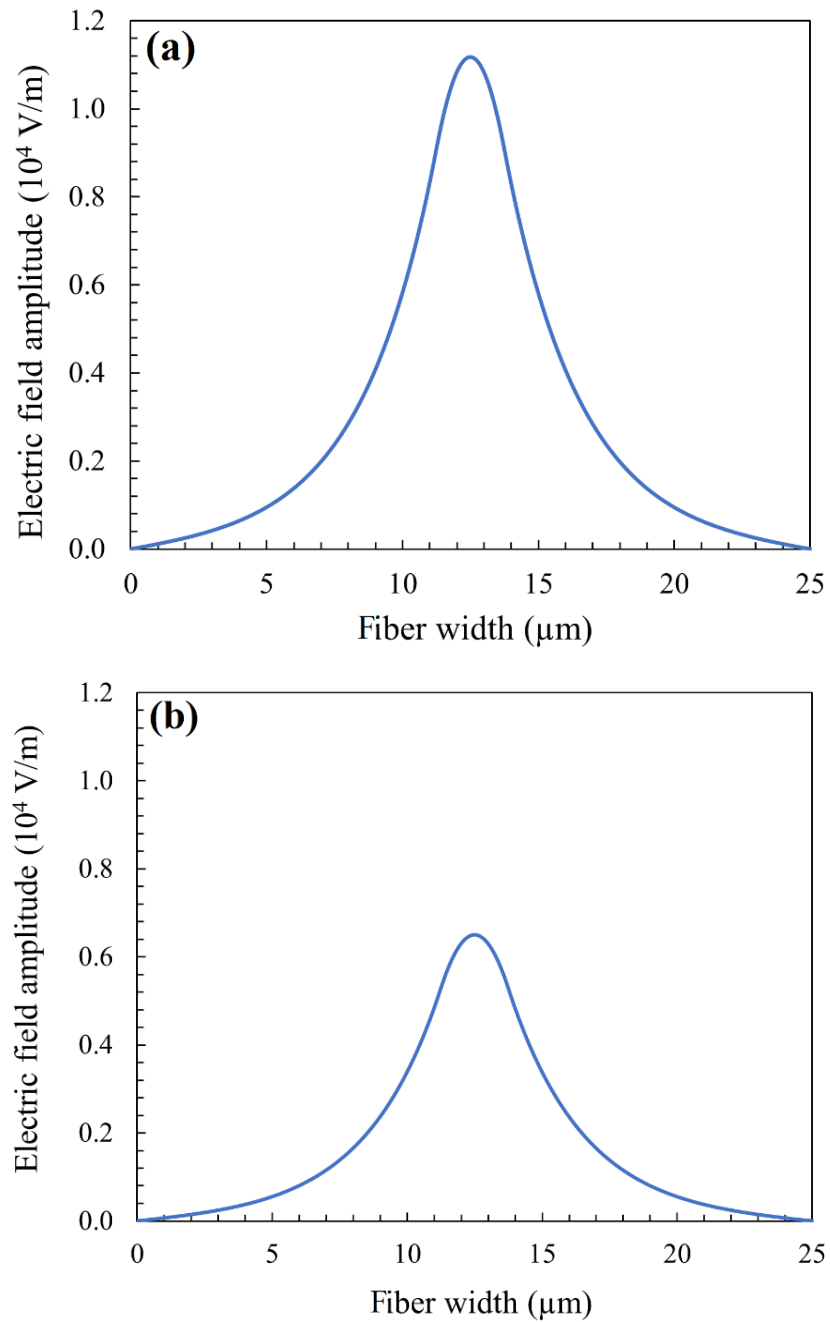


Figure 3.3 Output electric field amplitude obtained from the full-wave simulation for (a) no tapering, and (b) a tapered waist of 5  $\mu\text{m}$ . There is a decrease in electric field amplitude for smaller waist tapers.

### 3.1.2 Simulation on the tapered fiber using the beam envelope method

In this simulation, the beam envelope method is applied to simulate a tapered fiber having the exact dimensions of the actual fiber. The main equation for this method is given as [82]:

$$(\nabla \times i\nabla\phi_1) \times \mu_r^{-1}[(\nabla - i\nabla\phi_1) \times \mathbf{E}_1] - k_0^2 \left( \varepsilon_r - \frac{j\sigma}{\omega\varepsilon_0} \right) \mathbf{E}_1 = 0, \quad (3.2)$$

where  $\mu_r$ ,  $\varepsilon_r$ , and  $\omega$  are the relative permeability, relative permittivity, and angular frequency, respectively,  $\sigma$  is the electrical conductivity of the material,  $\mathbf{E}_1$  is the dependent variable (beam envelope) and  $\phi_1$  is the phase ( $\mathbf{k} \cdot \mathbf{r}$ ) in phasor representation of the field as follows:

$$\mathbf{E} = \mathbf{E}_1 \exp(-i\phi_1). \quad (3.3)$$

As mentioned before, with prior knowledge of  $\phi_1$ , the only unknown variable is  $\mathbf{E}_1$ . In this thesis, achieving the field amplitude satisfies our requirement since the light intensity is proportional to electric field amplitude ( $I = \frac{1}{2} (c\varepsilon E_1^2)$ ). After setting the "type of phase specification" as "wave vector" in COMSOL code, a defined variable could be used in the beam envelope interface in COMSOL software, called "ewbe. beta\_1". This variable represents the propagation constant for the wave, which propagates through the structure. As indicated in Fig. 3.4, for every propagating wave through a fiber, there are two components in the propagation constant: transverse ( $\beta_{\perp}$ ) and longitudinal ( $\beta_{\parallel}$ ). COMSOL first computes the transverse component of the propagation constant and then analytically calculates the longitudinal component using the following formula:

$$k^2 = n_1^2 \omega^2 c^2 = \beta_{\perp}^2 + \beta_{\parallel}^2. \quad (3.4)$$

In the beam envelope method,  $\beta_{\parallel}$  is referred to as ewbe. beta\_1 and is used as a predefined wave vector in the code.

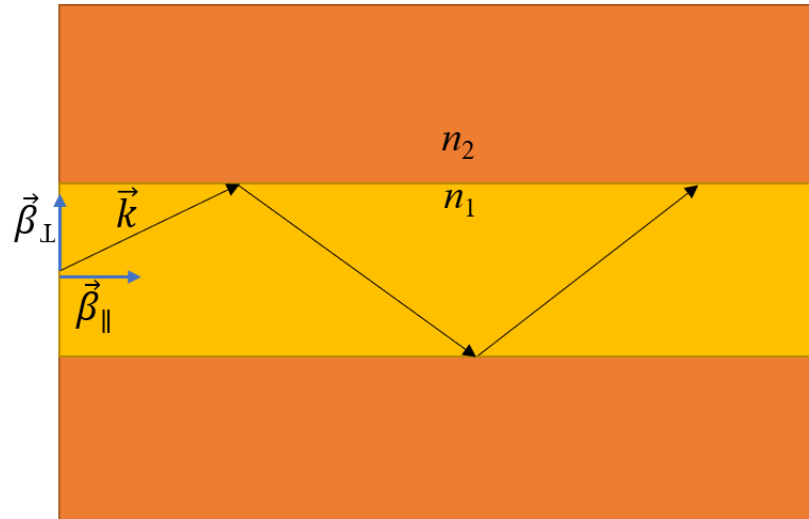


Figure 3.4 Wave propagation in waveguide with transverse and longitudinal components of the wave constants labeled as  $\beta_{\perp}$  and  $\beta_{\parallel}$ , respectively, in which  $\beta_{\parallel}$  refers to ewbe. beta\_1.

The geometry of the tapered fiber for a specific waist is shown in Fig. 3.5 (a), with a length of 500  $\mu\text{m}$ . The fiber core and cladding diameters are 10 and 125  $\mu\text{m}$ , respectively. Figure 3.5(b) indicates the input amplitude of the electric field of the wave propagating through the tapered fiber. Figure 3.5 (b) illustrates that the fiber core is the main path for light propagating along the fiber since the distance from 57 to 67  $\mu\text{m}$  (fiber core) includes the highest field amplitude so that in the core center, the field amplitude is around 9000 V/m, while this parameter in the fiber cladding is negligible.

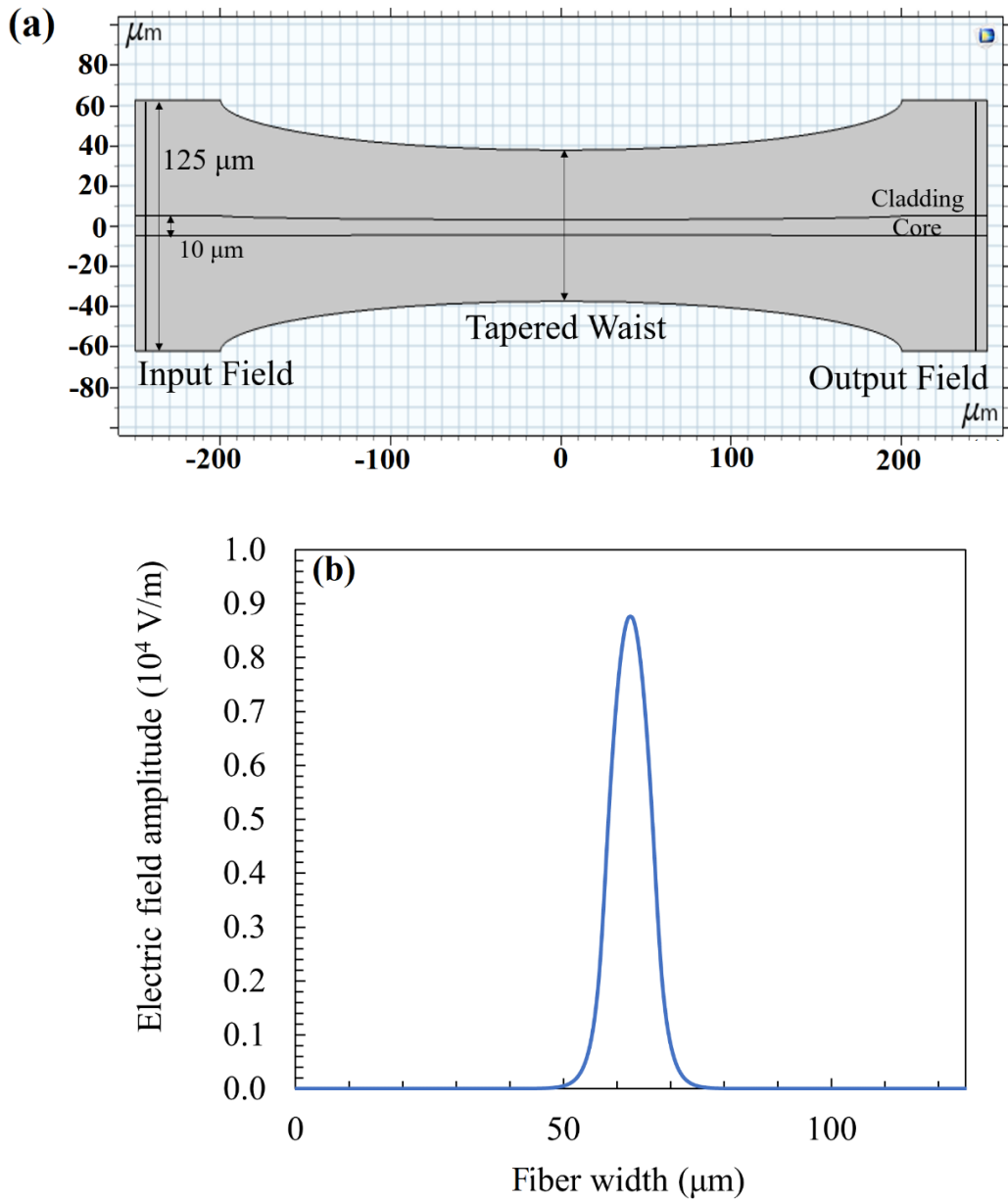


Figure 3.5 (a) Geometry of a fiber modeled in the beam envelope simulation. (b) input electric field amplitude achieved using the beam envelope method in COMSOL.

Figure 3.6 shows the output electric field amplitude of the propagating wave along an untapered and a tapered fiber with a waist of 25 μm, simulated using the beam envelope method in COMSOL Multiphysics software. Except for the amount of the field

amplitude, the results match the full-wave case since the output electric field amplitude is considerably lower than the input electric field amplitude for tapered fiber. However, the fiber dimensions are the actual values adopted in simulation using the beam envelope method.

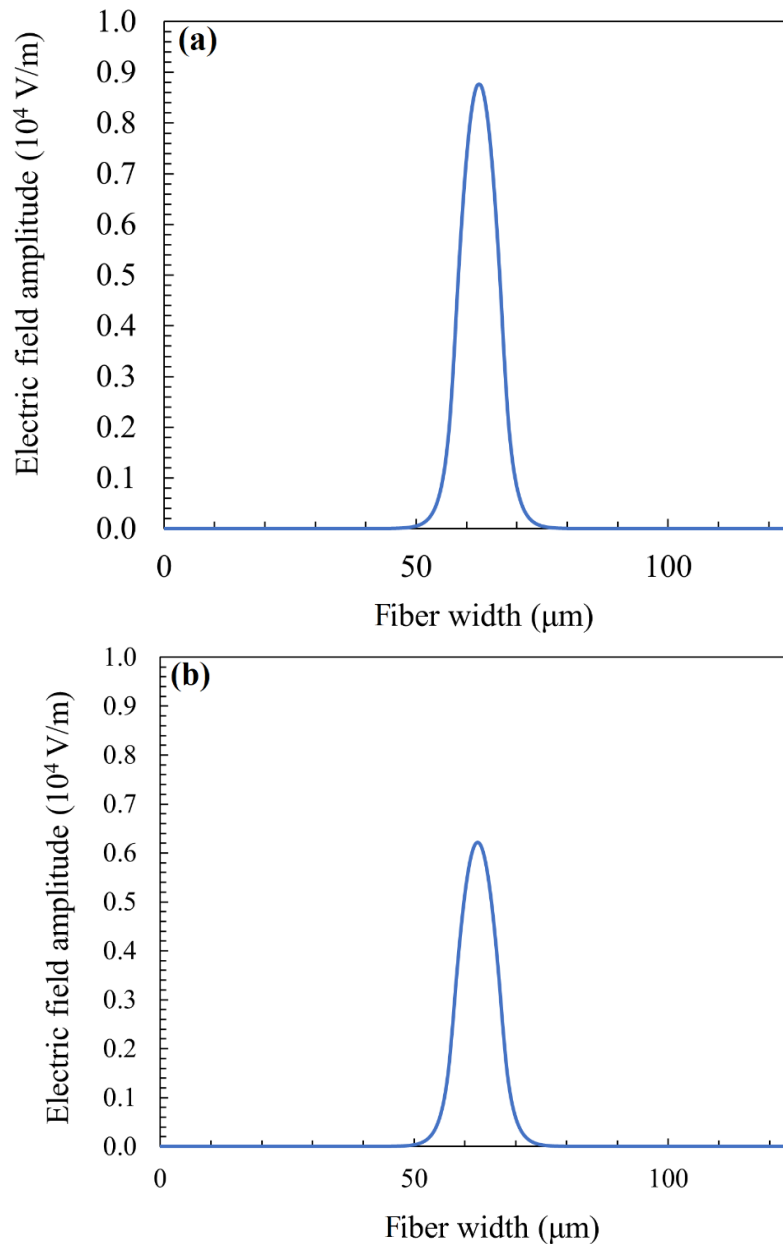


Figure 3.6 Output electric field amplitude for a tapered fiber simulated using the beam envelope method for (a) a fiber without tapering, and (b) a tapered fiber waist of 25  $\mu\text{m}$ .

The two methods provide the same results, but the full-wave method does not adopt actual fiber dimensions. Therefore, the beam envelope method will be employed in the following computations.

Before investigating LPG properties fabricated using the arc discharge method, it is worth examining the formation of a taper in a glass fiber. The geometry deformation on an optical fiber using the arc discharge method will be simulated and discussed in the next section.

### 3.2 Geometry deformation in the fiber using the arc discharge

In this section, the formation of a micro-tapered fiber by arc discharge and the effect of arc duration variations are simulated and investigated. The temperature profile resulting from the arc discharge is considered as a Gaussian distribution, with the temperature peaked around the arc discharge position. Figure 3.7 shows the temperature profile during the formation of a taper in the fiber.

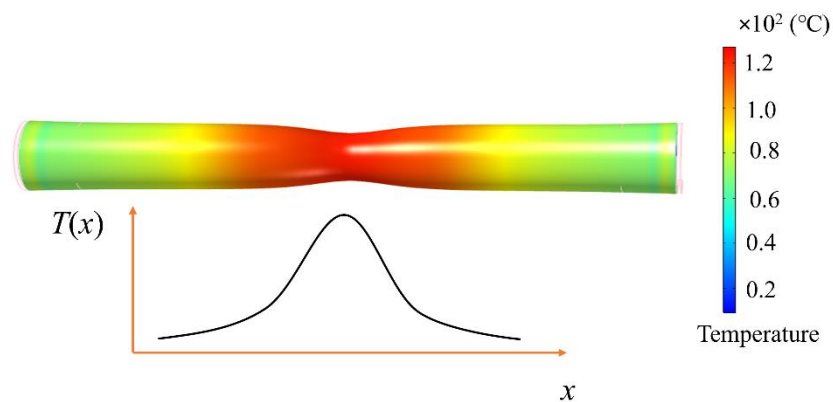


Figure 3.7 Schematic illustration of viscous stretching conforming to the temperature profile, scaled by color. The maximum temperature is 1300°C.

As shown in Fig. 3.7, the temperature at the arc point is the highest, which decreases as the distance moves further from the center until it finally reaches ambient temperature. In accordance with Ref. [73], the maximum value of the Gaussian-shaped temperature profile is set at 1300°C. Silica glass is known as a viscoelastic material, and when it is exposed to a stress at a high temperature along its axial direction, it undergoes successively elastic deformation, uniform plastic deformation, and non-uniform plastic deformation where localized necking occurs (see Fig. 3.8). The elastic contribution diminishes at a high-temperature range like the case here, and plastic deformation plays a dominant role [74]. Figure 3.8 shows a stress-strain diagram of a viscoelastic material with some information taken from Ref. [74].

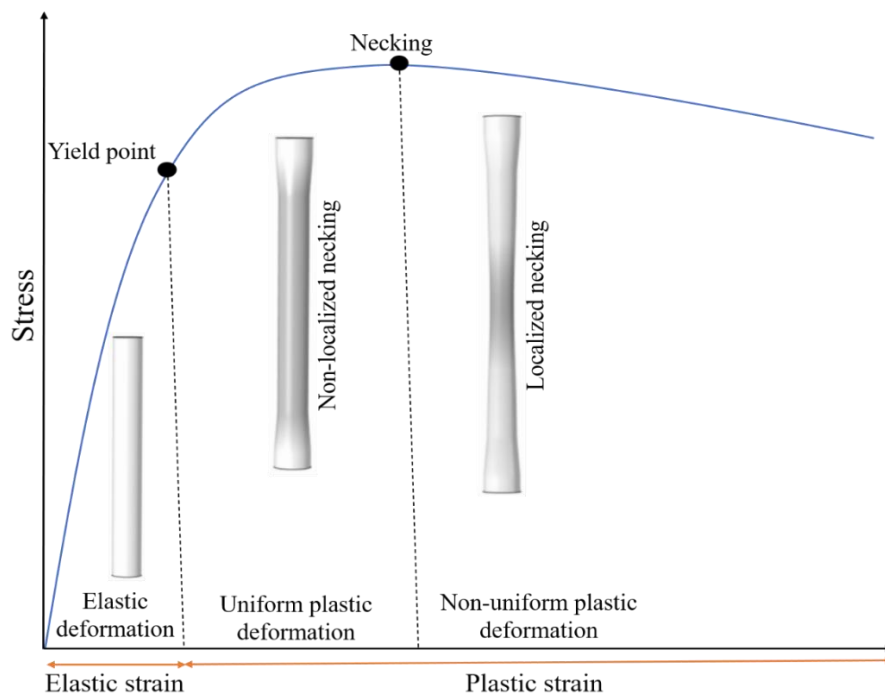


Figure 3.8 Stress-strain relationship in the uniaxial tensile stretching of a viscoelastic material.

The central temperature range in the arc discharge location is around 1300°C, according to references on arc-induced LPG [73, 75]. Based on this information, the

simulation is conducted in this temperature range. After determining the temperature profile, building a model of glass fiber is the next step. The following Subsection is included a model of a glass fiber using the actual fiber dimensions.

### 3.2.1 Structure model

In the model adopted for this study, a cylindrical glass fiber with a length of  $500\ \mu\text{m}$  and a radius of  $62.5\ \mu\text{m}$  (the radius of standard silica fiber) is subjected to various elongations. Since this problem requires highly sufficient fine mesh (small in size and large in number), a two-dimensional axial symmetry model is adopted to conduct the calculations for only one-fourth of the geometry. The entire geometry can be obtained using a rotation around the vertical axis and a mirror oriented on the horizontal axis, as illustrated in Fig. 3.9.

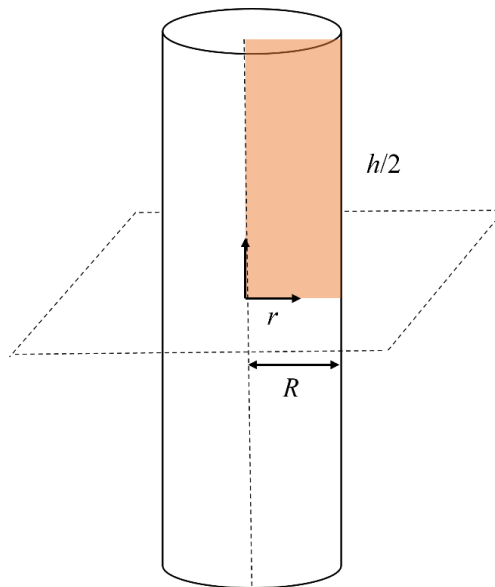


Figure 3.9 Schematic illustration of the model of the optical fiber used in this simulation. The dash line and the square indicate the rotational symmetrical axis and mirror, respectively.

The main module used in the simulation for this study has been chosen as "Structural Mechanics". The range of material behavior is selected as "Plasticity", and the

plasticity model is determined to be "Large Plastic Strains." The bottom and top boundaries are set as high-temperature plane and stress-affected plane, respectively. In the following Subsection, the governing equations of viscoelastic material and its adoption to the glass fiber are discussed.

### 3.2.2 Material model

The elastic behavior of silica fiber material is characterized by Young's modulus of 73.1 GPa and Poisson's ratio of 0.17 [74]. At a high enough temperature, the plastic response of a viscoelastic material like glass can be characterized by yield stress as follows [74]:

$$\sigma_y = \sigma_{y0} + \sigma_h, \quad (3.5)$$

where  $\sigma_{y0}$  is the initial yield stress and  $\sigma_h$  is the nonlinear hardening function as given in the following:

$$\sigma_h(\varepsilon_{pe}) = H\varepsilon_{pe} + (\sigma_{yf} - \sigma_{y0})[1 - \exp(-\xi\varepsilon_{pe})]. \quad (3.6)$$

The hardening function  $\sigma_h$  depends nonlinearly on the equivalent plastic strain  $\varepsilon_{pe}$ . Here,  $H$  is the linear hardening coefficient,  $\sigma_y$  is the saturation flow stress or residual yield stress, and  $\xi$  is the saturation exponent. The corresponding numerical values for the hardening function are listed in Table 3.1 [74].

Table 3.1 Numerical values for parameters relating with hardening function.

Parameter	Value
$\sigma_{y0}$	1.5 MPa
H	0.07 MPa
$\sigma_y$	3 MPa
$\xi$	100.93

Figure 3.10 shows the plotted diagram of Eq. 3.5 using the parameters shown in Table 3.1.

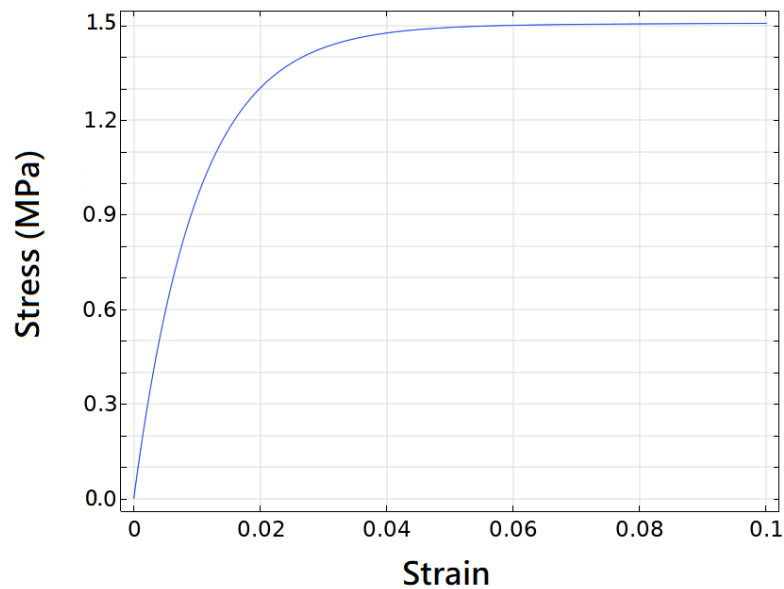
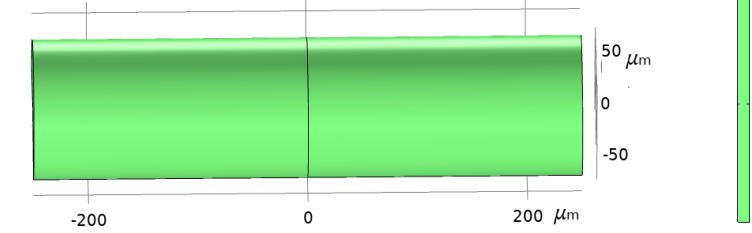
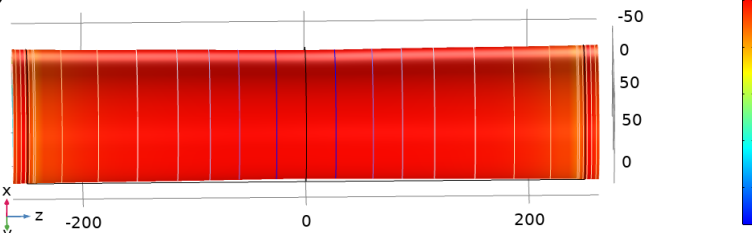
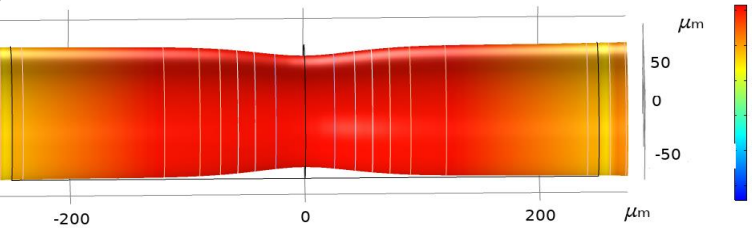


Figure 3.10 Nonlinear isotropic hardening as a function of equivalent plastic strain for a glass fiber.

### 3.2.3 Glass fiber necking

Applying the above stress-strain relationship on glass fiber with a temperature of 1300°C results in an elongation of 0  $\mu\text{m}$  to 220  $\mu\text{m}$  (Fig. 3.11). Figure 3.11 shows the gradual transformation of a non-tapered fiber to a tapered fiber. The figure includes 3D geometric deformation along the fiber at 3 MPa stress (or 29.4 mN), scaled by color. As shown in Fig. 3.11(a), the green color throughout the fiber shows no stress on the fiber, which means there is no tapering on the fiber at the beginning. Upon an elongation of 24.3  $\mu\text{m}$ , the tapered fiber waist decreases to 120.11  $\mu\text{m}$ . The color scale indicates the occurrence of non-localized necking through the entire fiber with maximum stress (red) (Fig 3.11(b)). Although increasing the fiber elongation to 48.1  $\mu\text{m}$  reduces the tapered waist to 105.35  $\mu\text{m}$ , the uniform plastic deformation regime dominates because most of the fiber is exposed

to the maximum stress (3 MPa) as shown in Fig 3.11(c). A 70.2  $\mu\text{m}$  elongation changes the effective stress distribution from the entire length of the fiber to the middle section, resulting in localized necking (Fig 3.11(d)). For elongations greater than 70.2  $\mu\text{m}$ , the tapered waist decreases significantly due to the maximum stress on the central region, implying that the process is in the non-uniform plasticity regime.

Elongation ( $\mu\text{m}$ )	Resulting structure	Taper Waist ( $\mu\text{m}$ )
0.0	<p>(a)</p> 	125
24.3	<p>(b)</p> 	120.11
48.1	<p>(c)</p> 	105.38

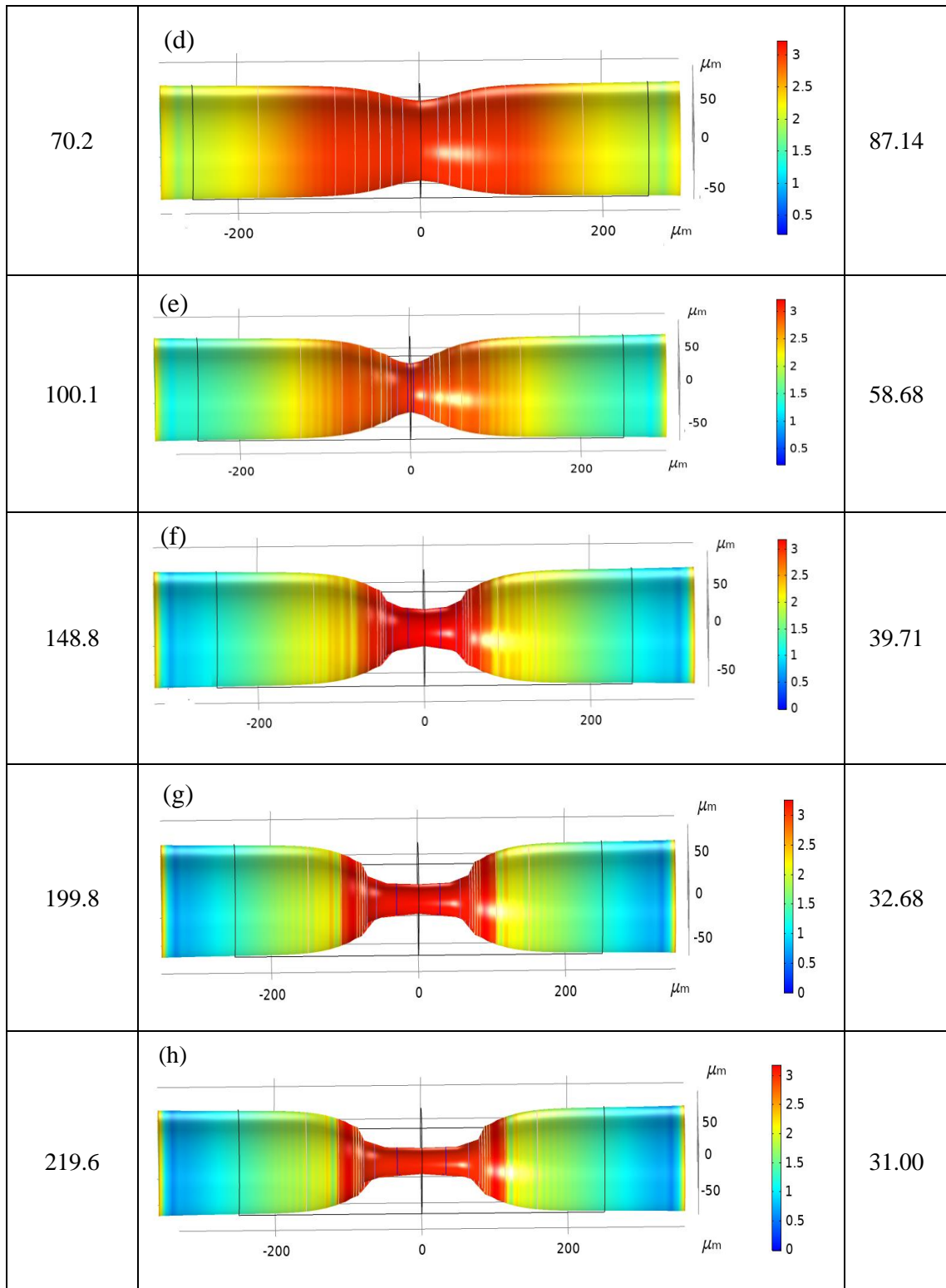


Figure 3.11 Simulation results for stretched fiber under the stress of 3 MPa. The stress is scaled by color.

It is noteworthy to consider the diameter of the waist of the prepared micro-tapers and tapered fibers. As shown in Fig. 3.12, increasing the fiber elongation results in a nonlinear decrease in the tapered waist.

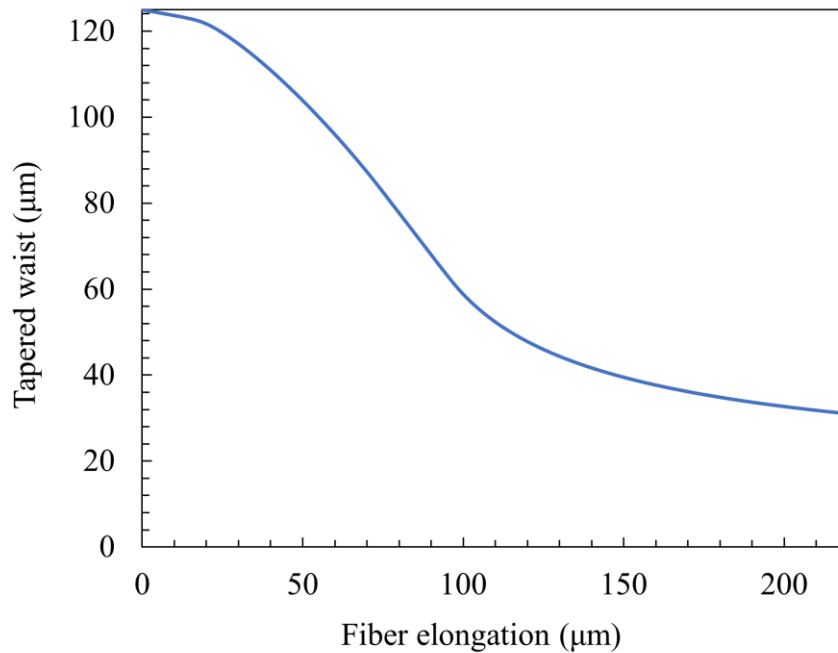


Figure 3.12 Necking development in the middle section of a fiber at a temperature of 1300°C and stress of 3 MPa.

### **3.3 Simulation on the effect of fabrication parameters on the formation of the LPG**

#### **3.3.1. LPG electric field distribution and transmission spectrum**

This Subsection describes an LPG simulation using a two-dimensional geometry model in COMSOL Multiphysics software. Figure 3.13 shows one period of the LPG model, during which the fiber core and cladding sections are created using rectangles. The lengths of these rectangles are the same and equal to the product of the number of gratings multiplied by

the periodicity ( $N \times \Lambda$ ). In contrast, the transverse dimension corresponds to the diameters of core and cladding sections of the single-mode fiber, which are 10 and 125  $\mu\text{m}$ , respectively. The grating segment and geometric deformation are shown using half ellipses. The minor and major axes of the ellipse are used to simulate LPG geometric deformations that result from the use of the arc discharge method. Generally, this model simulates a dielectric slab waveguide that is finite in the  $x$  and  $y$  directions.

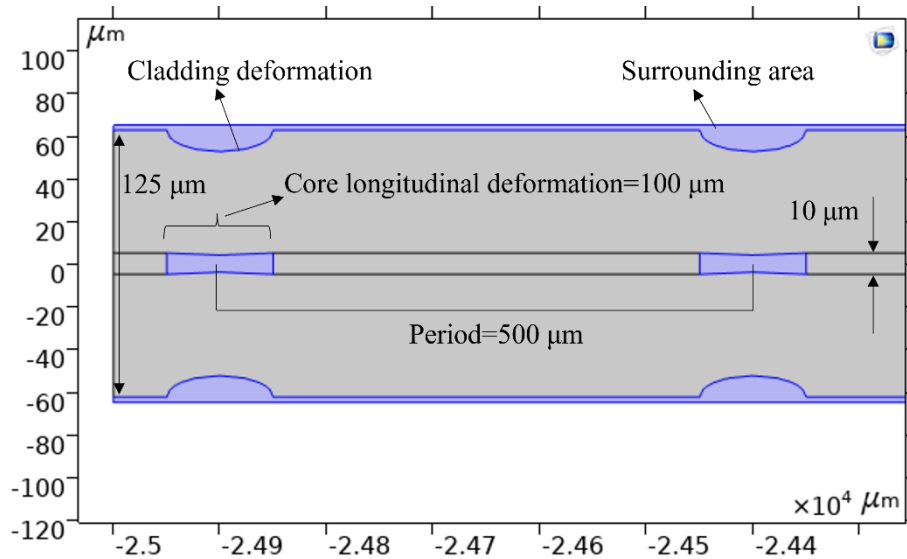


Figure 3.13 Geometry of one period of the of a two-dimensional model of the LPG in COMSOL. The  $y$ -direction is compressed by 0.5 to permit the entire period to be represented in the figure. the vertical axis scale is ( $\mu\text{m}$ ), and transverse axis is scale ( $\times 10^4 \mu\text{m}$ ).

The refractive indices of the core, the cladding, and the surrounding area (air) are reported to be 1.4457, 1.4378 (with  $\pm 1\%$  relative error on  $\Delta n (= n_{\text{co}} - n_{\text{cl}})$ ) [70], and 1.0 ( $1.0 \pm 1.2 \times 10^{-4}$ ) [77], respectively. Based on Ref. [74], changes in the refractive indices of the fiber core and cladding in the tapered sections due to the arc discharge are assumed as  $(-7.0 \pm 0.2) \times 10^{-4}$  and  $(3.0 \pm 0.1) \times 10^{-7}$ , respectively. Therefore, the refractive index for the grating sections in the fiber core is determined to be  $1.44500 \pm (0.00002)$ , while the

cladding refractive index modulation is neglected due to its small values compared to the core refractive index modulation. A scattering boundary condition is also selected due to the power loss through the boundaries during light propagation in the LPG. The periodicity of the LPG is chosen to be 500  $\mu\text{m}$  according to experimental samples. In the electromagnetic wave module in COMSOL software, "port" is the location where the electromagnetic energy enters or exits the model. Since the outcome of the model is electric field amplitude, the numerical type of port (input and output boundaries) is used to model the propagating wave. Another important aspect is the choice of the method used to model electric field distribution. As discussed in Section 3.1, the best option to model the LPG is to use the beam envelope method. Main equations and assumptions are explained in Section 3.1. Since the wave propagates predominately in one direction, a unidirectional wave is chosen instead of a bidirectional one. Due to its nature, the beam envelope method does not require the fine mesh to perform these calculations, but the maximal element size must still be in the same order of magnitude as the central wavelength. In this model, the core region is meshed by an equilateral triangular coarse mesh consisting of a height equal to the wavelength (1.550  $\mu\text{m}$ ), while the cladding and air region are meshed by the height of 3.65 times the wavelength ( $3.65 \times 1.55 \mu\text{m}$ ). Figure 3.14 shows the electric field distribution along the  $x$ -direction. The color scale indicates that most of the energy still propagates in the core region. Only a small part, peaked at the resonance wavelengths due to the coupling of the core mode with the higher-order cladding modes, penetrates the cladding regions (Fig. 3.15).

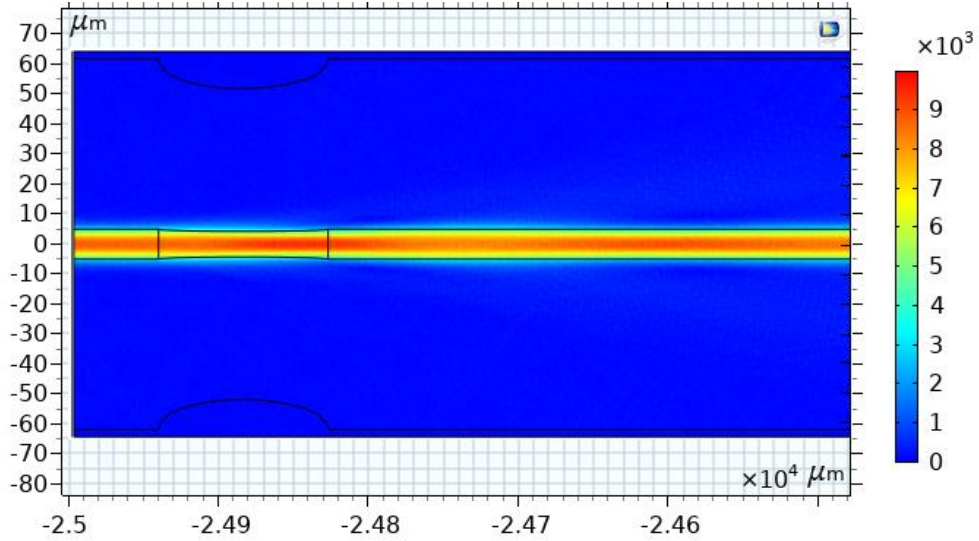


Figure 3.14 Electric field distribution in all fiber areas at a wavelength of 1550 nm. The color scale shows that most light energy propagate along the fiber core.

Since the LPG fabricated using the electric arc discharge method is usually weak in terms of core refractive index modulation, many periodicities are required to achieve concrete grating formation. The achieving transmission spectrum of the abovementioned structure is illustrated in Fig. 3.15. This spectrum is obtained from an LPG with a grating number of 100 and a periodicity of 500  $\mu\text{m}$ . As discussed in Subsection 1.4.2, resonance wavelengths in the transmission spectrum of LPG satisfy the phase-matching condition, which is given by:

$$\lambda_{\text{res}}^m = (n_{\text{eff,co}} - n_{\text{eff,cl}}^m)\Lambda, \quad (1.10)$$

where  $\Lambda$  is the grating period, and  $n_{\text{eff,co}}$  and  $n_{\text{eff,cl}}^m$  are the effective refractive indices of the core and the  $m^{\text{th}}$  order of the cladding modes, respectively. As Fig. 3.15 shows, the first resonance mode is formed at  $1491.1 \pm 0.1$  nm, while the second resonance is positioned at  $1665.8 \pm 0.1$  nm. Several side lobes around the second resonance mode in Fig. 3.15 indicate

that those wavelengths partially meet the phase-matching condition. For a detailed study of this phenomenon, one may need to consider the detuning parameter  $\delta$ , which is used to describe the coupling efficiency between the core and cladding modes in an LPG, as given by [34]:

$$\delta(\lambda) = \pi(n_{\text{eff,co}} - n_{\text{eff,cl}}^m) \left( \frac{1}{\lambda} - \frac{1}{\lambda_{\text{res}}} \right), \quad (3.7)$$

where  $\lambda$  indicates the wavelength where the detuning parameter is studied. Depending on how much the studied coupling has been detuned, the detuning parameter can be changed from 0 to 1.  $\delta=0$  occurs when the resonance wavelength corresponding to the coupled modes fully satisfies the phase-matching condition, and when  $\delta=1$ , the coupling between the core mode and the cladding modes is not detuned. Therefore, the side lobes around the second resonance mode corresponding to the cases when the values of the detuning parameter are close to zero, while this parameter is zero in case of resonance.

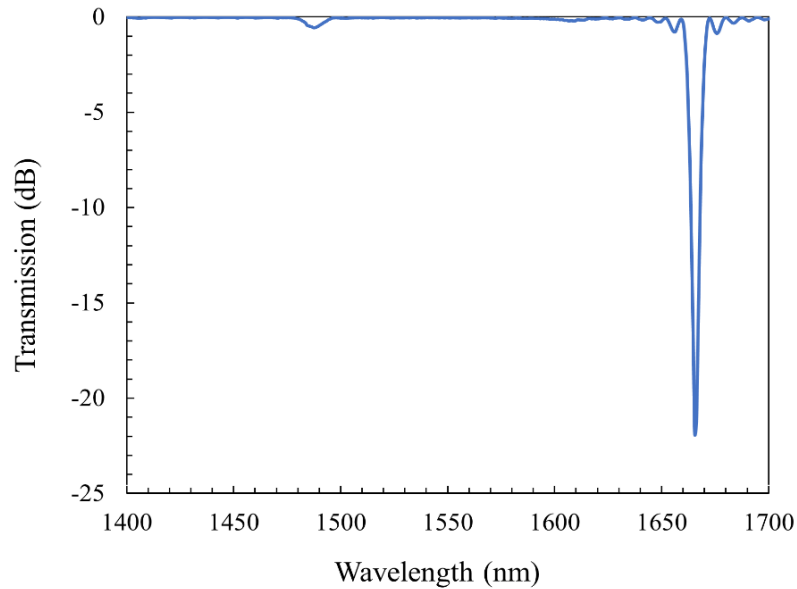


Figure 3.15 Transmission spectrum of an LPG with a periodicity of 500  $\mu\text{m}$ , grating number equal to 100, and a grating length of 100  $\mu\text{m}$ .

This study uses the second resonance mode to study LPG properties since higher-order modes are more sensitive to environmental perturbations.

### 3.3.2 Effect of the number of gratings on the properties of LPG

Since the transmission spectrum of LPG is crucial for its applications, it is vital to investigate the formation of the spectrum during LPG fabrication, focusing primarily on how varying the number of the grating periods ( $N$ ) affects spectrum growth. In this study, the grating longitudinal length ( $100\ \mu\text{m}$ ) and the periodicity ( $500\ \mu\text{m}$ ) are kept constant.

As shown in Fig. 3.16, the spectrum of this structure revolves around a resonance wavelength of  $1665.8\ \text{nm}$  as the number of grating periods changes. Figure 3.16 implies that, as the number of gratings increases, intensity loss becomes considerable. For instance, the attenuation dip for  $N=100$  is  $-22.134\ \text{dB}$ , while for  $N=75$ , it is  $-10.76\ \text{dB}$ .

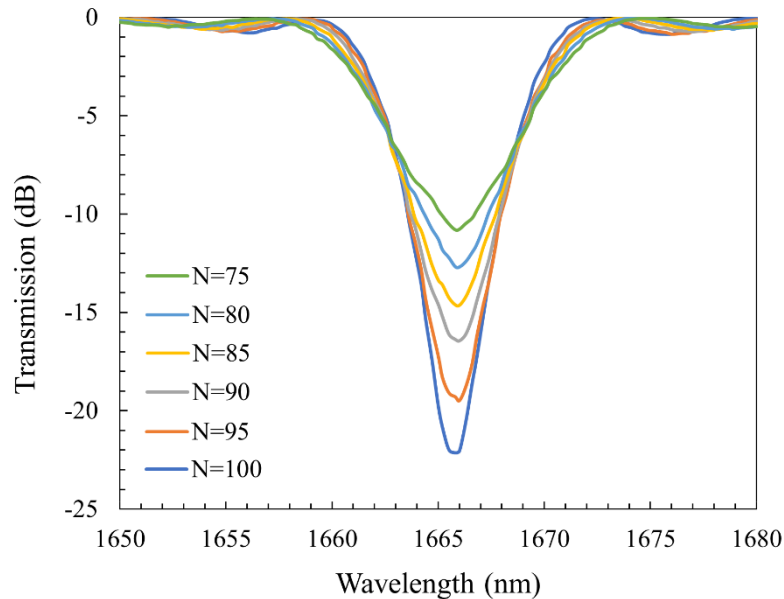


Figure 3.16 Evolution of the transmission spectra of LPGs with an increase in the grating number.

The remainder of this section investigates the effect of variations in the LPG fabrication parameters, such as arc current, arc duration, and mass as tension applied to the fiber.

### **3.3.3 Influence of arc current variation on the transmission spectrum of LPG**

Arc current is one of the important parameters in the operation of the fiber fusion splicer, playing an essential role in LPG fabrication. This part of the study uses a grating number of 100 and a periodicity of 500  $\mu\text{m}$ . According to the experimental results, geometric deformation and refractive index modulation in the core and cladding sections of the fiber result from the arc discharge applied on the fiber. The arc discharge serves to form micro-tapers in the fiber core and cladding sections. The average waist of a micro-taper fabricated at an arc current of 5 mA is  $110 \pm 1 \mu\text{m}$ , and  $105 \pm 1 \mu\text{m}$  when the arc current is 10 mA. The corresponding diameters with arc currents of 15, 20, and 25 mA are  $99 \pm 1$ ,  $91 \pm 1$ , and  $86 \pm 1 \mu\text{m}$ , respectively. In the tapering process, in addition to occurrence tapering in the fiber cladding, there is a fiber core tapering that must be included in the modeled structure in the COMSOL code. Since the tapering process occurs in fiber as a unified structure, an approximation to start quantitative analysis to take this modulation account is to use the same tapered waist ratio for the fiber cladding (tapered waist/fiber cladding diameter). For instance, for an arc current of 5 mA, the ratio of the tapered waist to the fiber diameter is  $110/125$ ; therefore, the tapered waist in the core is  $[(110/125) \times 10 = 8.8 \mu\text{m}$ . These data are adopted in the model to run in the COMSOL Multiphysics software. The results are illustrated in Fig. 3.17. For an arc current of 5 mA,  $\text{LP}_{02}$  mode is located at

1686.6 ± 0.1 nm, whereas the same mode for the LPG fabricated at an arc current of 10 mA peaks at 1678.2 ± 0.1 nm. The resonance wavelengths for arc currents of 15, 20, and 25 mA are 1669.7 ± 0.1 nm, 1663.7 ± 0.1 nm, and 1657.7 ± 0.1 nm, respectively.

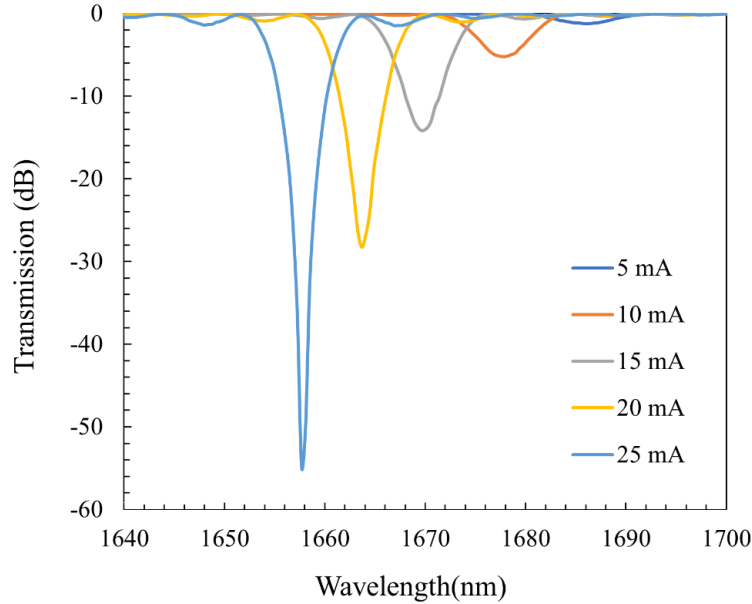


Figure 3.17 Evolution of the LPG transmission spectrum with varying arc current during fabrication.

As shown in Fig. 3.18, a linear dependence of the resonance wavelength on the arc current with a slope of  $-1.43 \pm 0.0068$  nm/mA (blueshift) is found. Note that the uncertainty for the slope of the linear trend is achieved using the equation:  $1 - R^2$ . Figure 3.19 shows the quadratic relationship between the intensity loss and the arc current applied for LPG fabrication. As the arc current increases, the fitted downside curve shows that the propagating light loses its intensity to a greater extent during propagating along the LPG.

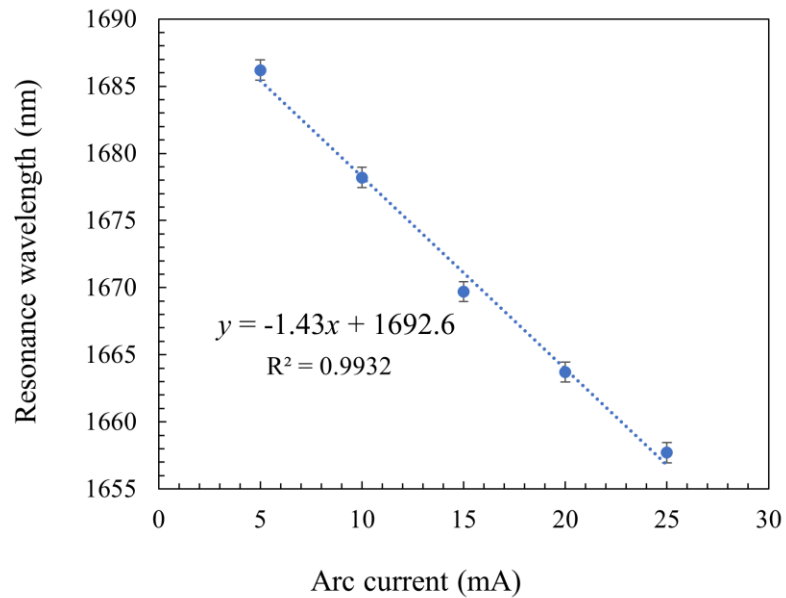


Figure 3.18 Dependence of resonance wavelength of the LPG on arc current.

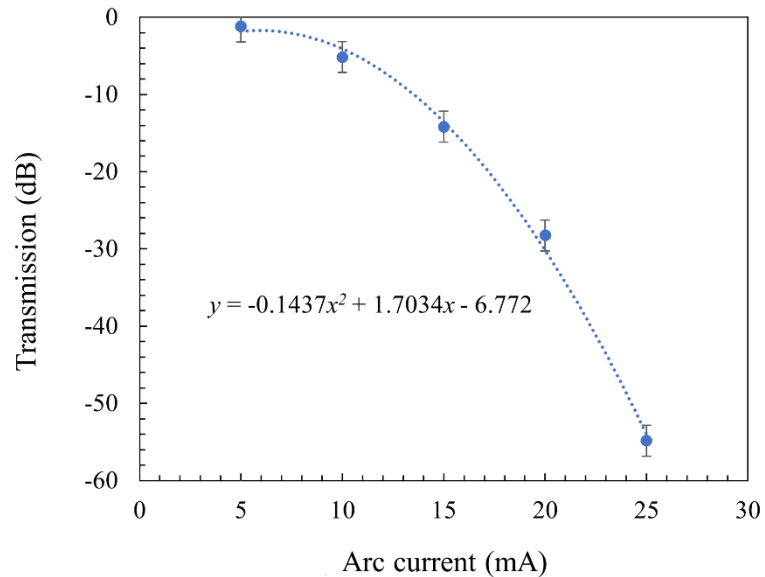


Figure 3.19 Intensity loss variations of the LPG when the arc current changes.

### 3.3.4 Influence of arc duration variation on the transmission spectrum

This Subsection examines how arc duration variation affects the LPG transmission spectrum. During the experiment, while the other parameters are fixed (arc current and

tension are set at 10 mA and 12.5 mN, respectively), the arc duration is varied from 150 ms to 450 ms. The average micro-taper diameter obtained from an arc duration of 150 ms is  $105 \pm 1 \mu\text{m}$ , while diameters obtained for arc durations of 250, 350, and 450 ms are  $101 \pm 1 \mu\text{m}$ ,  $97 \pm 1 \mu\text{m}$ , and  $94 \pm 1 \mu\text{m}$ , respectively. These values are used in the COMSOL Multiphysics software model to obtain the transmission spectra of the LPG (see Fig. 3.20). Figure 3.20 shows the shifting resonance wavelength position in the LPG transmission spectrum when the arc duration varies between 150 and 450 ms. Any increase in the arc duration results in a blueshift of the resonance wavelength.

The resonance wavelength locates at  $1678.2 \pm 0.1 \text{ nm}$  for 150 ms arc duration and  $1669.7 \pm 0.1 \text{ nm}$  for the arc duration of 250 ms. Resonance wavelengths obtained using arc durations of 350 and 450 ms are  $1661.7 \pm 0.1 \text{ nm}$  and  $1657.7 \pm 0.1 \text{ nm}$ , respectively.

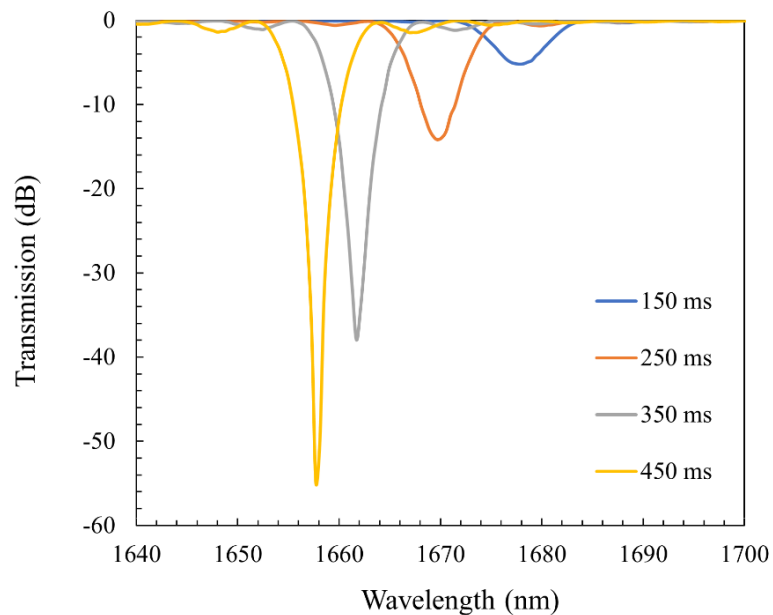


Figure 3.20 Changes in the transmission spectrum of the LPG resulting from arc duration variations.

Figure 3.21 shows the dependence of resonance wavelengths on their corresponding arc durations. The best linear fit shows a negative slope of  $-0.069 \pm 0.023$  nm/ms, indicating that the resonance wavelengths shift towards increasingly shorter wavelengths as arc duration increases. Since each increment in the arc duration in the fusion splicer is 100 ms, with a one-increment increase in the arc duration, the blueshift in the resonance wavelength is 6.9 nm.

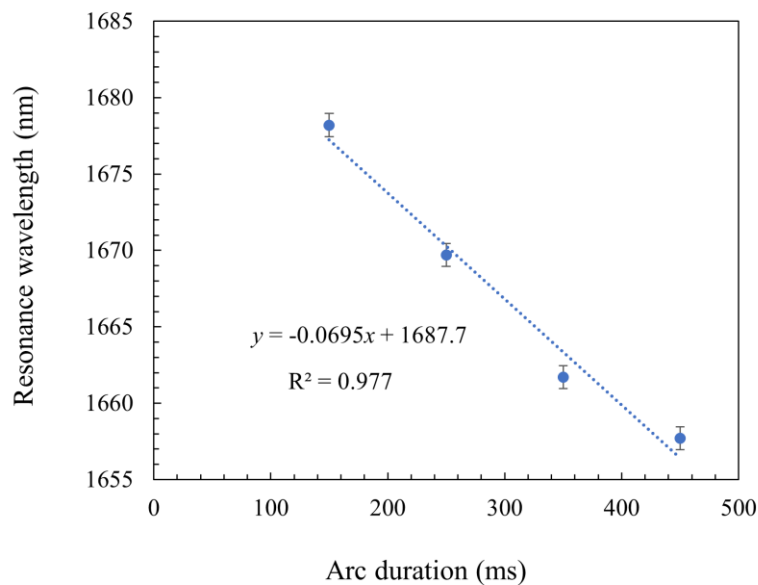


Figure 3.21 Shifts in the resonance wavelength of the LPG resulting from variation in arc duration.

Figure 3.22 shows changes in the intensity loss when the arc duration is varied. In this case, the best fit for the data is a nonlinear trend. Thus, as the arc duration increases, the propagating light loses its intensity to a greater extent during propagating along the LPG.

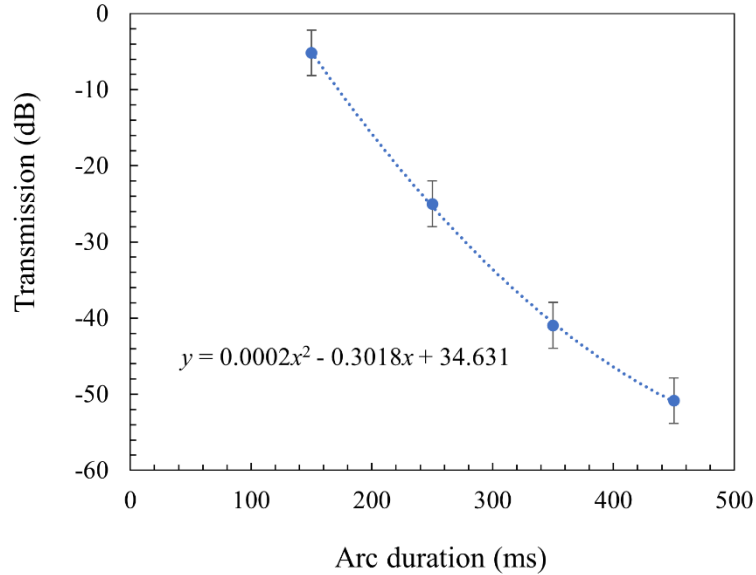


Figure 3.22 Changes in intensity loss of the LPG resulting from arc duration variation.

### 3.3.5 Influence of tension variation on the transmission spectrum of LPG

The last parameter examined is the tension along the fiber. As a standard procedure, the arc current and the arc duration are fixed at 10 mA and 250 ms, respectively, while the tension is varied between 12.5 to 25.5 mN. The calculated transmission spectra are shown in Fig 3.23. This figure shows that the resonance wavelength shifts increasingly towards the shorter wavelengths as the tension increases.

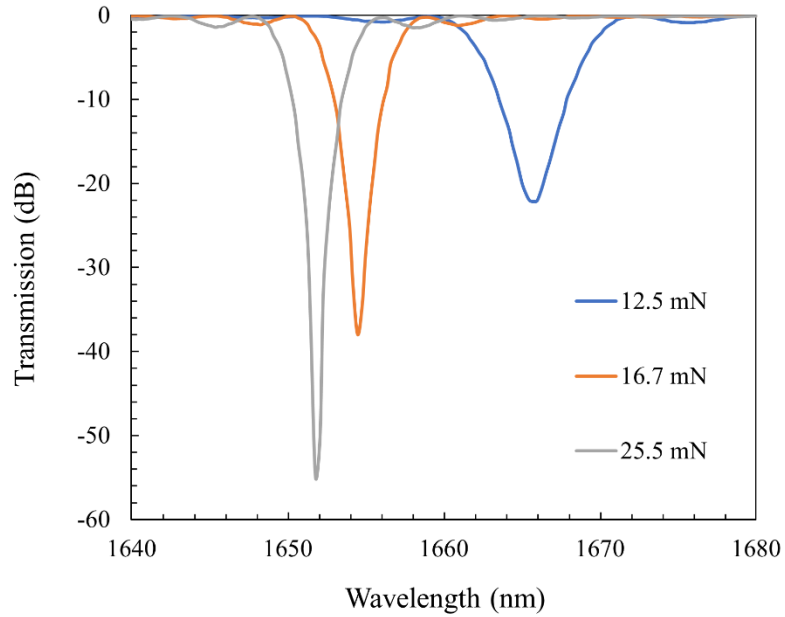


Figure 3.23 Changes in the transmission spectrum of LPG resulting from tension variation.

Figure 3.24 shows the resonance wavelengths shift when the applied tension along the fiber changes. As the tension increases, the resonance wavelength in the LPG transmission spectrum shifts towards shorter wavelengths.

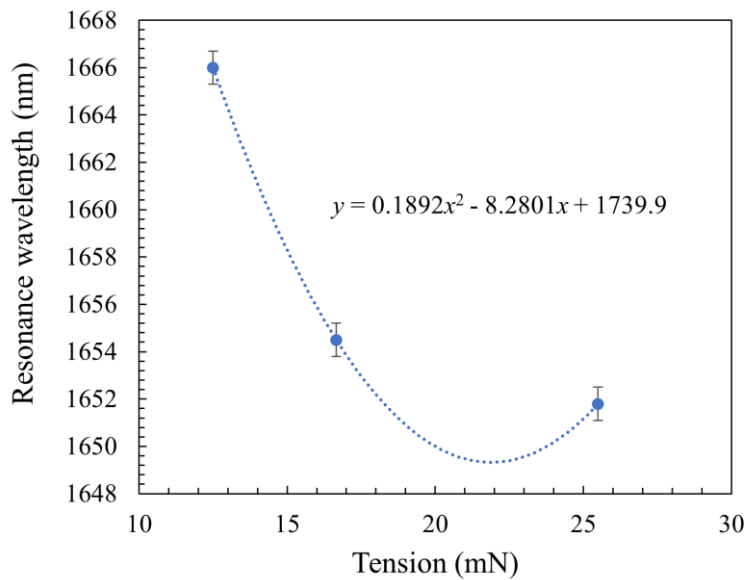


Figure 3.24 Shifts in the resonance wavelength of the LPG when the tension change.

An examination of the changes in the intensity loss due to variations in mass proves to be worthwhile (see Fig. 3.25). The best fit for the data exhibits a quadratic trend, indicating that the propagating waves increasingly lose their intensity as the mass increases.

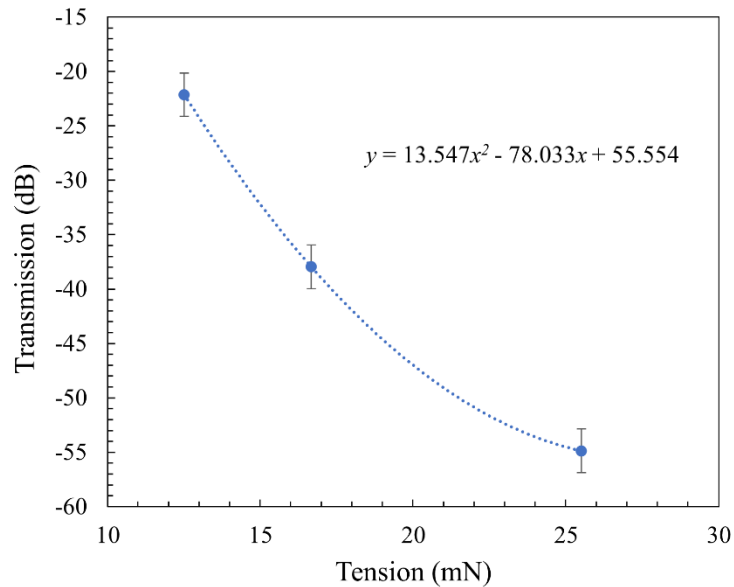


Figure 3.25 Changes in the intensity loss of the LPG resulting from tension variation.

In general, increasing any of the fabrication parameters results in a decrease in the effective refractive index of the fiber core, while the effective refractive index of the fiber cladding is negligible compared to the core refractive index modulation [74]. According to Eq. (1.10), since the periodicity is fixed at 500  $\mu\text{m}$ , the resonance wavelength value decreases, which means a shift towards shorter wavelengths. Furthermore, increasing one of the LPG fabrication parameters, whether arc current, arc duration, or tension, leads to the formation of micro-tapers with a smaller waist. Smaller waist micro-tapers cause a decrease in the local fiber core diameter and increase the coupling strength between the core mode and higher-order cladding modes, resulting in a more substantial loss in the

guided mode. In addition, any modulations in the core refractive index can nonlinearly change the transmission spectrum of the LPG due to Eq. (1.11), which implies that the light transmission through the core of LPG follows a sinusoidal function of the core refractive index modulation for the wavelengths in the resonance [66].

This section has discussed simulations conducted on an LPG using the electric arc discharge method. The effects of varying parameters on LPG fabrication have been investigated, and the influence of those parameters on the LPG transmission spectrum has been examined. The sensing properties of the arc-induced LPG will be discussed in the next section.

### **3.4 Use of LPG as a sensor**

Variations in external parameters, such as temperature, strain, bending, load, or refractive index, change the physical properties of LPG, including their transmission spectrum. This feature enables LPG to act as a sensor to monitor environmental parameters by detecting shifts of resonance wavelengths in the transmission spectrum. This section describes the simulation of arc-induced LPG in response to external refractive index and temperature using the beam envelope method with COMSOL Multiphysics software.

#### **3.4.1 LPG as an environmental refractive index sensor**

This subsection examines the sensing performance of LPG refractive index sensors. As previously mentioned, resonance wavelengths in the transmission spectrum of an LPG result from the coupling of the core mode into the higher order of cladding modes. The

phase-matching condition for the coupling of the forwarded propagating core mode and the  $m^{\text{th}}$  order of the cladding mode has been explained using Eq. (1.10) in Section 1.4.

Due to absorption and scattering, cladding modes escaping from a fiber into its surrounding medium are the main mechanisms for an LPG to act as a refractive index sensor. According to Eq. (1.10), a resonance wavelength is dependent on the effective refractive indices of core ( $n_{\text{eff}}^{\text{co}}$ ) and cladding ( $n_{\text{eff}}^{\text{cl}}$ ) modes, as well as on the grating period ( $\Lambda$ ). Because the effective refractive index of a cladding mode depends on the refractive index of the ambient environment (Eq. (3.9)), any change in the refractive index of the surrounding medium will result in a shift in the transmission spectrum [78]. In the present model, this issue addresses by changing the refractive index of the surrounding layer from 1.0 to 1.4375. Figure 3.26 shows the geometry model for these measurements. The model

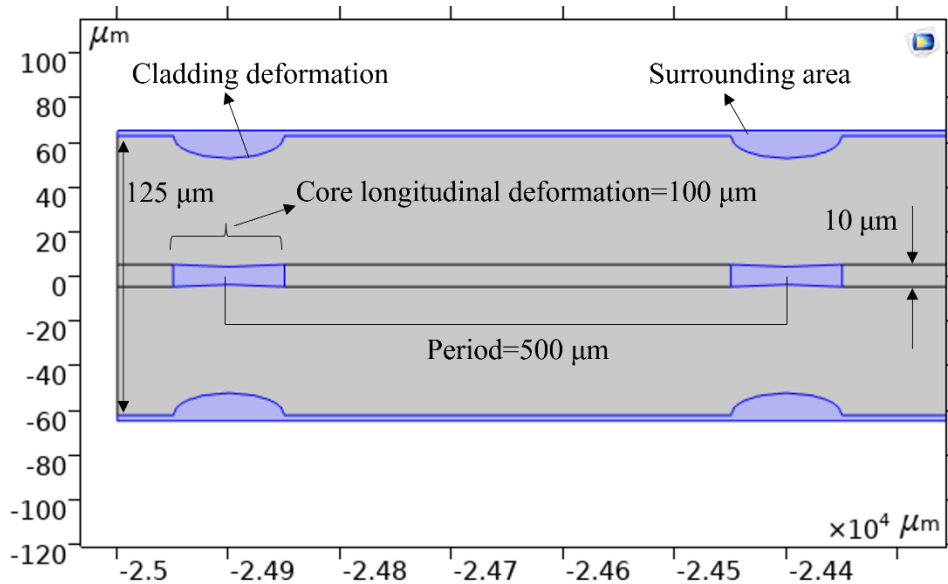


Figure 3.26 Geometry of 2D model of LPG adopted in COMSOL simulation.

adopts the same structure used to investigate arc-induced LPG properties. The geometric deformations and the surrounding area are illustrated in the inset of the figure.

Figure 3.27 shows a simulation result of the LPG transmission spectrum shifts when the environmental refractive index changes. As shown in Fig. 3.27, an increase in the surrounding refractive index results in a blueshift in the transmission spectrum. Since an LPG fabricated using the arc discharge technique is a weak grating, to achieve a better resolution, the number of the gratings, the mass, the arc current, and the arc duration are set as 70, 2.5 g, 10 mA, and 250 ms, respectively. As evident in Fig. 3.27, when the surrounding refractive index is very close to 1.0 (the refractive index of air), there is no considerable change in the resonance wavelength. Even for the case with a refractive index of water (1.33), the spectrum is still very close to the situation where the surrounding

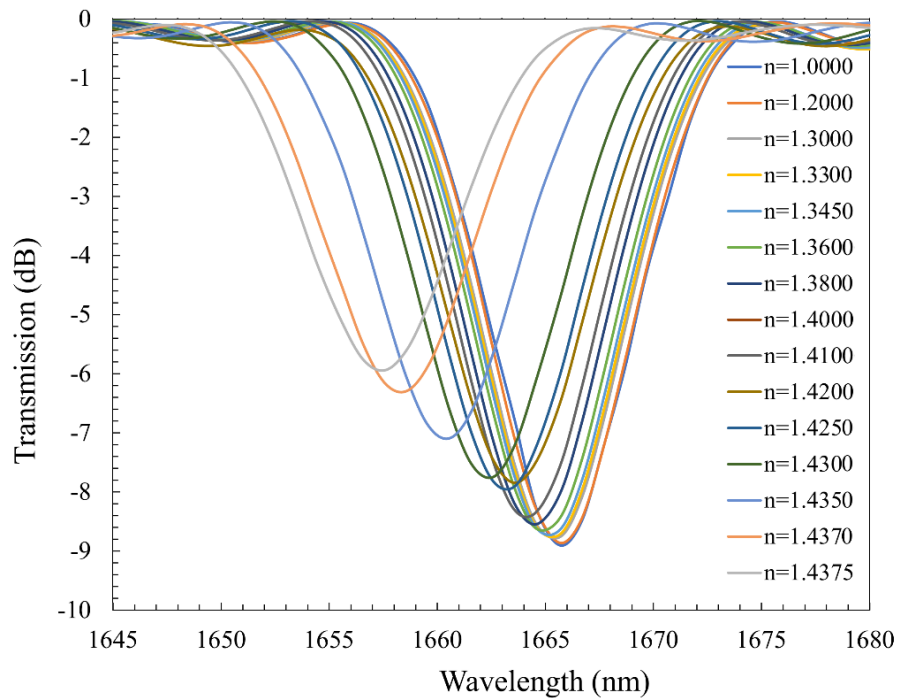


Figure 3.27 Influence of refractive index variation on resonance wavelength in arc-induced transmission spectra of LPG (simulation results).

medium is air. However, when the surrounding refractive index approaches that of the cladding, the variation of the transmission spectrum becomes significant. As shown in Fig 3.27, a considerable blueshift in the spectrum is found for values very close to 1.4378 (the cladding refractive index).

As shown in Fig. 3.28, the shift in resonance wavelength is minimal for a surrounding medium having a small refractive index. However, when the refractive index approaches that of the cladding, the resonance wavelength shifts significantly, so that for a range from environmental refractive indices 1.4000 to 1.4375, the LPG sensitivity to the surrounding medium refractive index is significant (-170.82 nm/RIU).

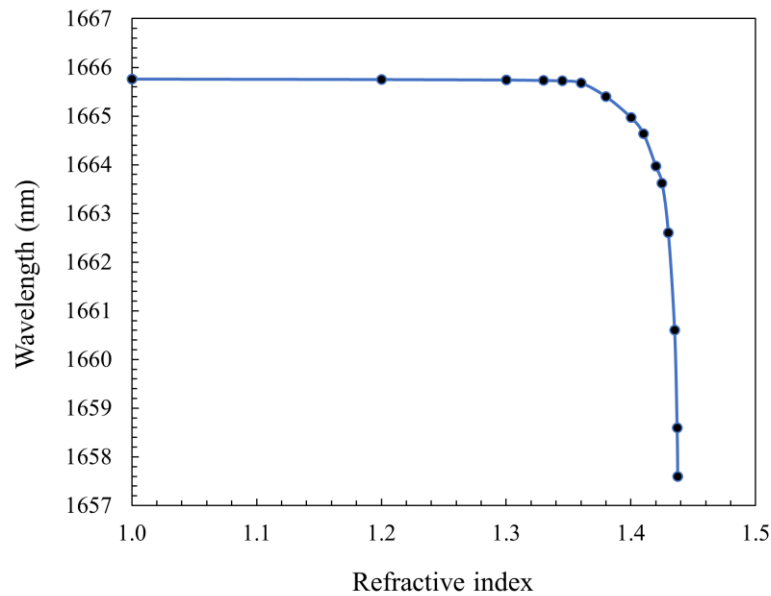


Figure 3.28 Dependence of resonance wavelength shifts on environmental refractive indices for an arc-induced LPG (simulation results).

LPG sensitivity to the environmental refractive index originates from the dependency of the fiber cladding's effective refractive index on the surrounding medium refractive index ( $n_s$ ). The effective refractive index of the cladding modes determines the

resonance wavelength in a transmission spectrum. This dependency can be represented by the following equation [79]:

$$\frac{d\lambda_{\text{res}}}{dn_s} = \lambda_{\text{res}}\gamma\Gamma_s, \quad (3.7)$$

where  $\gamma$  is the general sensitivity factor describing waveguide dispersion, given by [79]:

$$\gamma = \frac{d\lambda_{\text{res}}/d\Lambda}{n_{\text{eff}}^{\text{co}} - n_{\text{eff}}^{\text{cl}(m)}}, \quad (3.8)$$

in which  $d\lambda_{\text{res}}/d\Lambda$  represents the slope of the dispersion curves, and  $\Gamma_s$  is expressed by [79]:

$$\Gamma_s = - \frac{u_m^2 \lambda_{\text{res}}^3 n_s}{8\pi r_{\text{cl}}^3 n_{\text{cl}} (n_{\text{eff}}^{\text{co}} - n_{\text{eff}}^{\text{cl}(m)}) (n_{\text{cl}}^2 - n_s^2)^{3/2}}, \quad (3.9)$$

which is valid for  $n_s < n_{\text{cl}}$ . In equation (3.9), which confirms the waveguide dispersion dependency on the environmental refractive index, the term  $u_m$  is the  $m^{\text{th}}$  root of the zero-order Bessel function. Equations (3.8) and (3.9) imply that the sensitivity can be enhanced with the slope of the dispersion curves ( $d\lambda/d\Lambda$ ), which require higher-order modes. This is why the LP<sub>02</sub> mode is chosen as the reference resonance wavelength for measuring external refractive index variations.  $\Gamma_s$  is a negative parameter; therefore, for any surrounding medium refractive index smaller than the refractive index of the cladding, there is a blueshift since all other parameters are positive in Eq. (3.7). As Eq. (3.9) shows, there is an increase in sensitivity as the environmental refractive index approaches that of the cladding. This is why any resonance wavelength shift becomes significant when the surrounding medium refractive index is very close to that of the cladding. For a refractive index very close to the refractive index of the cladding, the evanescent field penetrates

further in the external medium and has a stronger interaction with the surrounding environment; therefore, the sensitivity is increased in this range of the refractive index. If the environmental refractive index equals that of the cladding, the resonance disappears because the total internal reflection rule becomes invalid. The resonance appears at longer wavelengths for a refractive index higher than that of the cladding [80]. These results have been proven through experiments [81, 82, 84].

### 3.4.2 LPG as a temperature sensor

To simulate LPG acting as a temperature sensor, a thermal stress module with a temperature variation ranging from 20°C to 120°C is used in the COMSOL Multiphysics software. This module, which is a combination of a "solid mechanics" interface and a "heat transfer" interface, permits heat energy from the heat transfer interface to act as a thermal load for the solid mechanics interface, resulting in thermal expansion of the LPG (and as a result, periodicity expansion). Also, environmental temperature variations affect the transmission spectrum by influencing the refractive indices of the fiber core and cladding. This effect is examined using the beam envelope method. The temperature sensitivity of the LPG originates from the following equation [84]:

$$\frac{d\lambda}{dT} = \frac{d\lambda}{d(\delta n_{\text{eff}})} \left( \frac{dn_{\text{co}}}{dT} - \frac{dn_{\text{cl}}}{dT} \right) + \Lambda \frac{d\lambda}{d\Lambda} \frac{1}{L} \frac{dL}{dT}, \quad (3.10)$$

where  $\lambda$  is the resonance wavelength of the attenuation band,  $T$  is the environmental temperature,  $n_{\text{co}}$  is the effective refractive index of the core mode,  $n_{\text{cl}}$  is the effective refractive index of the cladding mode,  $\delta n_{\text{eff}}$  is  $(n_{\text{co}} - n_{\text{cl}})$ ,  $L$  is the length of the LPG, and  $\Lambda$  is the LPG period. Two main terms form the right-hand side of Eq. (3.10). The first term

shows the material contribution from the thermo-optical properties of the core and the cladding materials. Obviously, fiber composition and cladding mode order are the main factors in this contribution. For coupling to lower-order cladding modes, which can be obtained for  $\Lambda > 100 \mu\text{m}$ , the material contribution dominates the temperature sensitivity of the fiber. In contrast, for higher-order cladding mode couplings (accessible for  $\Lambda < 100$ ), the impact of this term will be negligible [85]. In this term, the material contribution appears as a change in differential effective refractive indices. The second term of the right-hand side of Eq. (3.10) is the waveguide contribution. This term originates from the LPG periodicity variations. Increasing the temperature expands the length of the structure, which in turn expands the periodicity. The order of the cladding mode determines the sign and the magnitude of this part. Since all components in this term are positive, the sign of this term is determined by  $d\lambda/d\Lambda$ . The sign of  $d\lambda/d\Lambda$  is positive if the primary core mode is coupled with the lower-order cladding modes, i.e., for  $m$  from 1 to 9 in the cases discussed in this thesis, while this term will be negative in cases where the modes are coupled into higher-order cladding modes [85]. Since all parts in Eq. (3.10) are positive, an increase in the environmental temperature results in a redshift in the LPG transmission spectrum. To simulate these effects on a standard single-mode optical fiber, COMSOL uses the required parameters of the fiber, which are listed in Table 3.2 [74].

Table 3.2 Physical parameters of a single-mode fiber.

Property	Value
Coefficient of thermal expansion	$0.55 \times 10^{-6}$ [1/k]
Heat capacity at constant pressure	703 [J/(kg.K)]
Density	2203 [kg/m <sup>3</sup> ]
Thermal conductivity	1.38 [W/(m.K)]
Young's modulus	73.1 [GPa]
Poisson's ratio	0.17

Since the refractive index modulations in the arc-induced long-period fiber gratings are relatively low (around  $10^{-4}$  for  $n_{\text{core}} = 1.4478$  and  $10^{-7}$  for  $n_{\text{cladding}} = 1.4378$ ), the calculation must use LPG with a high grating number. In this model, the number of gratings is chosen to be 100 so that the intensity loss for the  $LP_{02}$  resonance mode is around -23 dB, as shown in Fig. 3.29(a). In addition, the calculations are conducted with lower uncertainty (0.05 nm) because of very small shifts in resonance wavelength (compared to the environmental refractive index variation) due to temperature variations. The original resonance wavelength for the modeled structure is  $1665.70 \pm 0.05$  nm, measured at room temperature (20°C). When the temperature is increased to 40°C, the resonance wavelength shifts to  $1665.80 \pm 0.05$  nm, indicating a 100 pm shift towards longer wavelengths. This change is very small and difficult to distinguish in Fig. 3.29(a); therefore, enlarged curves around  $1665.70 \pm 0.05$  nm are shown in Fig. 3.29(b). When the temperature increases to 60°C, the resonance wavelength shifts by 300 pm towards longer wavelengths. A further increase in the temperature to 80°C results in a resonance wavelength shift of 400 pm in the transmission spectrum towards longer wavelengths. Running the code for temperatures up to 100°C induces a shift in the resonance wavelength from 1665.7 to 1666.4 nm, corresponding to a 700 pm redshift. The environmental temperature of 120°C leads to a redshift in the transmission spectrum by 900 pm.

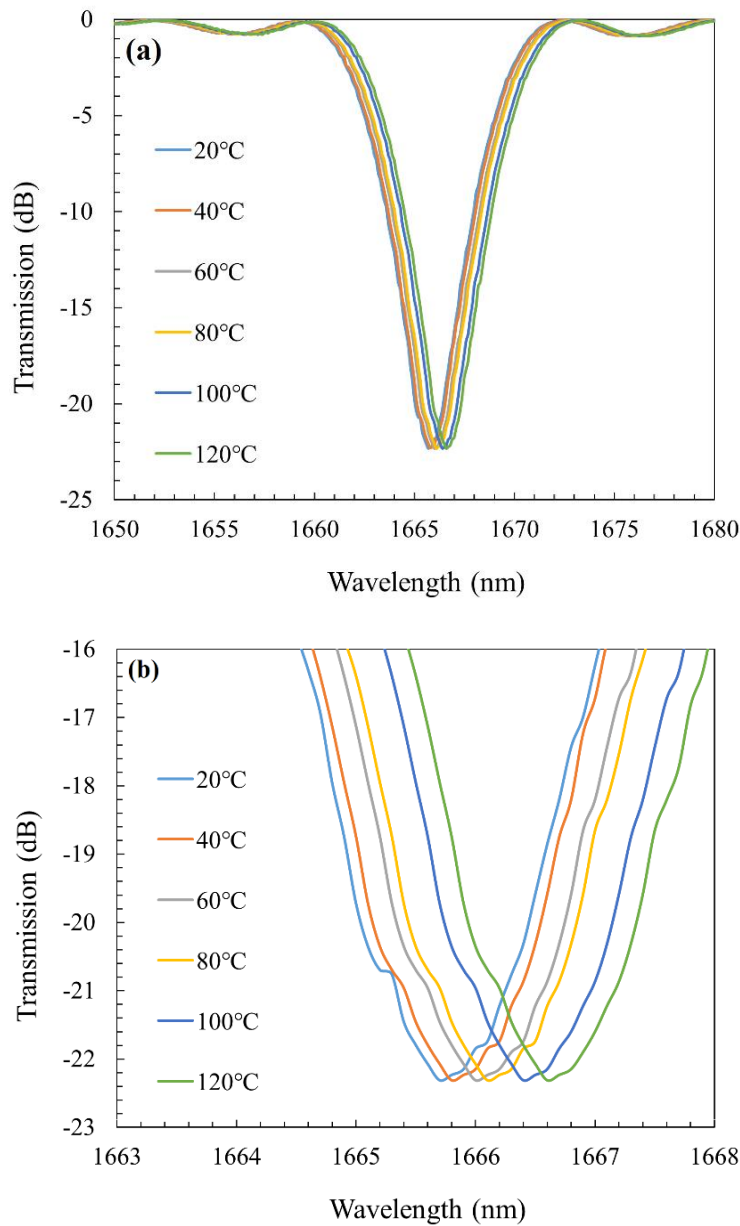


Figure 3.29 (a) Influence of temperature variation on resonance wavelength in the transmission spectrum of an arc-induced LPG. (b) Enlarged curves of the resonances at around 1665.70 nm.

From Fig. 3.30, the temperature sensitivity of the LPG can be derived from the linear fit, which is  $(9.8 \pm 0.0036) \times 10^{-3} \text{ nm}/^\circ\text{C}$  ( $\approx 10 \text{ pm}/^\circ\text{C}$ ). In most cases, for an LPG fabricated using UV light or femtosecond lasers, its sensitivities were reported to change

in a range from 0.01 to 0.1 nm/°C [85]. The same order of the sensitivity magnitude is revealed here for a sensor fabricated using the electric arc discharge method.

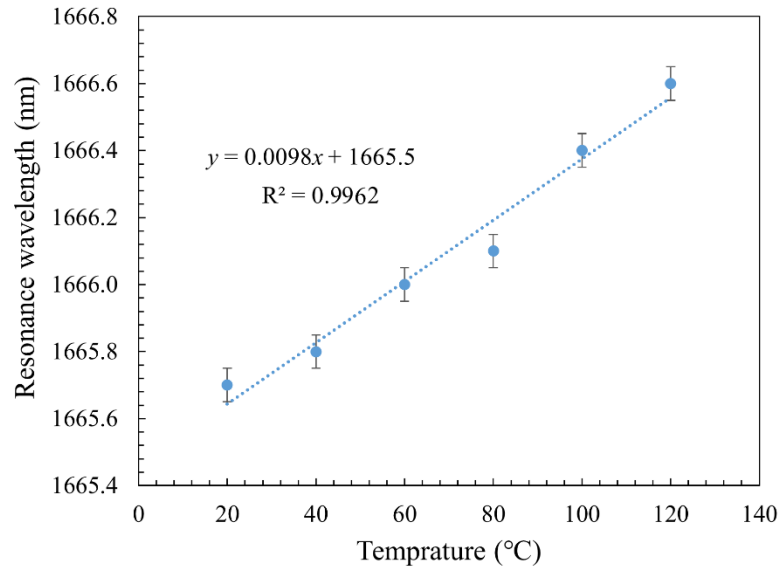


Figure 3.30 Effects of temperature variation on resonance wavelength in the transmission spectrum of arc-induced LPG (simulation results).

In summary, this chapter has investigated the suitable method for simulations on LPG properties resulting from the arc discharge method and its sensing properties. Using the beam envelope method in COMSOL Multiphysics software, the formation of geometry deformation resulting from applying the arc discharge on the fiber and variations in different LPG fabrication parameters have been simulated and discussed. The resulting LPG has been used as a sensor for environmental refractive index and temperature in the last section.

## **Chapter 4 Tapered fibers as a protein sensor**

### **4.1 Introduction**

Although fiber Mach-Zehnder interferometers (FMZI) consisting of dual tapers have been reported [86], the properties and applications of a single fiber taper have not been well studied. Such a study is worthwhile since single taper structures possess such salient advantages as simple structure and easy fabrication. The first part of this chapter discusses three single tapered fiber-based biosensors, each having different tapered waists. The first sample is a tapered fiber with a waist of 97  $\mu\text{m}$  and a length of 378  $\mu\text{m}$ . The second sample has the same length and a 58  $\mu\text{m}$  waist. This sample has an experimental correspondence that forms an inline MZI [67]. The third sample is a tapered fiber with the same length and a 45  $\mu\text{m}$  waist.

### 4.1.1 Structure functionalization

A symmetrical double tapered structure was used as an interferometer in experimental work performed by A. Maryam [67], a former MSc candidate of this Photonics Group. In this section, the sensing of protein concentrations is simulated only for a single tapered fiber. Figure 4.1 shows the geometry of a tapered fiber used for simulation in COMSOL Multiphysics with a length of 378  $\mu\text{m}$  and a waist of 58  $\mu\text{m}$ .

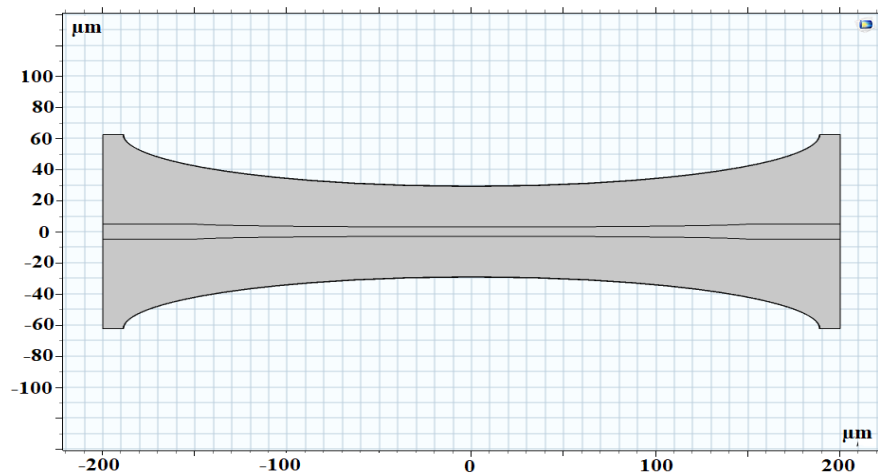


Figure 4.1 Geometry of a tapered fiber used for sensing in simulation.

The experimental results of Maryam *et al.* [67] state that the surface of a tapered fiber must first be functionalized in order to achieve biosensing capability. For this purpose, the structure is first treated with 1 wt% ethanolic KOH solution for 15 minutes. This step is essential because it provides the surface with negative charges so that the poly (allylamine hydrochloride) (PAH) monolayer can adhere to it. Next, the structure is dipped into 0.5 wt% PAH and then into negatively charged  $\text{SiO}_2$ : Au nanoparticles, each for 15 minutes to form one bilayer of PAH/ $\text{SiO}_2$ :Au NPs. This process is repeated two more times

to create two more bilayers. Finally, the three bilayers of PAH/SiO<sub>2</sub>:Au NPs are functionalized with 7 mM of Biotin for 30 seconds, rendering the structure ready to function as a biosensor [67].

Simulation computed using the COMSOL Multiphysics software also follows these steps adopted for the experimental study. In the simulation, it is challenging to determine how to model the nanoparticles on the structure. Every particle is a "Domain" in COMSOL software, and the maximum number of domains that COMSOL can support in a simulation code is limited to around 2000, whereas the actual number of nanoparticles deposited on the structure far exceeds this limit. Therefore, nanoparticles are treated as a nano-layer in the simulation, although the thickness of this layer has to be in the order of the relevant nanoparticle's average diameter. Also, it can be a good thought if the nanolayers are considered as several discrete pieces with several gaps between them. In this case, the gaps between every two discrete pieces must be filled with air or other related material which increase the number of Domains and makes it difficult to compile the code. In general, the

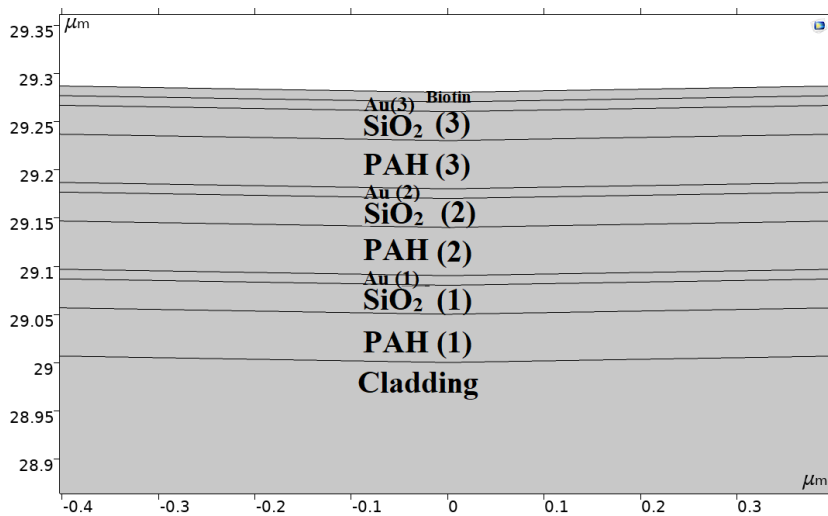


Figure 4.2 Schematic illustration of three bilayers used to functionalize a tapered fiber.

variety of dimensions from nanometer to centimeter in the structure makes the Domains meshing complicated enough and adding any more Domains to the COMSOL code, while the system facilities remain the same, makes stop the code compiling. In all structures adopted in the simulation, the thicknesses of PAH, SiO<sub>2</sub> and Au are 50 [87], 30 [88], and 10 nm [87], respectively, with refractive indices of 1.38 [89], 1.44 [90], and 0.5 +10i (10 for the imaginary part of the refractive index at 1550 nm wavelength) [91], respectively. For the top bilayer on the structure, the thickness and refractive index of the Biotin are considered as 10 nm [91] and 1.5 [93], respectively. Figure 4.2 shows the resulting three bilayers on the structure.

#### **4.1.2 Adsorption process**

On the surface of the fiber taper, a massive number of Biotin particles (in layer shape) adsorb Streptavidin proteins and change the optical properties of the surface, such as the refractive index. In the COMSOL Multiphysics software, surface reactions can be performed in the "Reaction Engineering" interface as a part of the "Chemistry" module. The reaction between surface Biotin and Streptavidin is expressed as [67]:



where  $SV$  represents nearby Streptavidin proteins, and  $B_{\text{surf}}$  is an abbreviation for Biotin on the tapered surface. The adsorption process takes place between these two materials. Since the Biotin concentration is fixed at the surface (7 mM), changing the protein concentrations makes it possible to control and adjust the reaction. The simulation using the COMSOL Multiphysics software is shown in Fig. 4.3.

The initial concentration of the protein is 83 nM (see Fig. 4.3). It is reasonable to assume that all the proteins adsorb to the Biotins due to the massive number of receptors on the surface of the fiber taper (7 mM). Figure 4.3 indicates the initial value for protein, which depletes in one second to produce  $SVB_{\text{surf}}$ . The final  $SVB$  amount is the same as the initial protein concentration. Since the "Surface Reaction" interface in the "Chemical" module includes a "deforming mesh" for the structure surface, the refractive index modulation caused by adsorption of the proteins onto the surface can be detected using the beam envelope method.

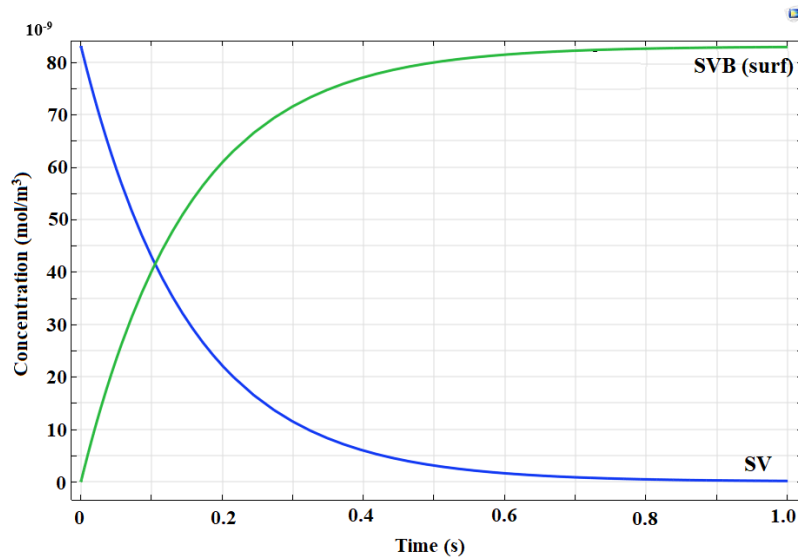


Figure 4.3 Adsorption reaction occurring between Biotin and Streptavidin protein on taper surface at room temperature.

#### 4.1.3 Simulation on sensing of Streptavidin protein concentration

To investigate the feasibility of a protein optical fiber sensor, it is a standard approach to use the Biotin-Streptavidin binding process [94]. The process mechanism is quite simple: binding the proteins to localized Biotins on the surface induces an increase in the refractive index of the surface. The change in the refractive index of the surface results in a detectable

change in the transmission spectrum, signifying a blueshift or redshift in the resonance peaks. The change in the refractive index strongly depends on the amount of proteins that bind to the Biotin on the surface. The amount of bound protein depends on the concentration of the protein. Therefore, based on the mechanisms mentioned here, it is feasible to detect SV protein concentration variations by evaluating the shift in the transmission spectrum.

## **4.2 Single tapered fiber biosensors**

### **4.2.1 Single tapered fiber biosensors coated with (PAH/SiO<sub>2</sub>:Au)<sub>3</sub>/Biotin, with a waist of 97, 58, or 45 μm**

Figure 4.4 shows the transmission spectra of a single tapered fiber biosensor with a waist of 97 μm, a length of 378 μm, and a coating of (PAH/SiO<sub>2</sub>:Au)<sub>3</sub>/Biotin. The peak wavelength, which occurs at 1564.42 nm for a bare single tapered fiber in water, shifts to 1564.410 ± 0.001 nm after coating, thereby showing a blueshift of 0.010 ± 0.002 nm. At 1564.410 ± 0.001 nm, this resonance wavelength serves as the reference point for measuring wavelength shifts due to different SV concentrations on the surface. Adding 83 nM SV-protein to the solution results in a shift in resonance wavelength towards shorter wavelengths at 1564.400 ± 0.001 nm, corresponding to a blueshift of 0.010 ± 0.002 nm. Increasing the SV concentration to 300 nM exhibits a blueshift of 0.030 ± 0.002 nm in the resonance wavelength. In contrast, the blueshift values are 0.050 ± 0.002 nm and 0.090 ± 0.002 nm for the 800 and 1300 nM SV concentrations, respectively. Tapered fiber with a large waist, such as in the case here, does not show a pronounced sensitivity due to a low

likelihood of evanescent field interaction with the surrounding environment. The same measurements are conducted for the tapered fibers with 58 and 45  $\mu\text{m}$  waists. Resonance wavelength shifts corresponding to each step are shown in Figs. 4.5 and 4.6. Table 4.1 shows the resonance wavelength shifts for all three tapers.

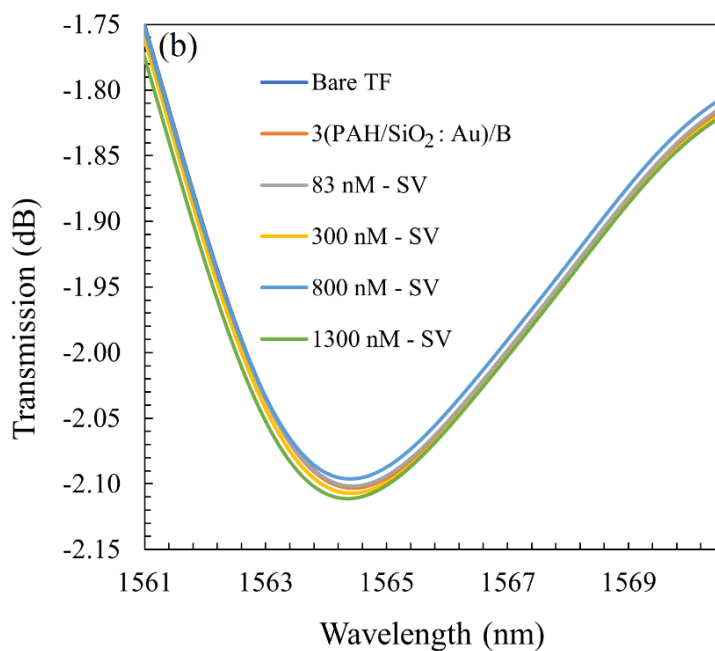
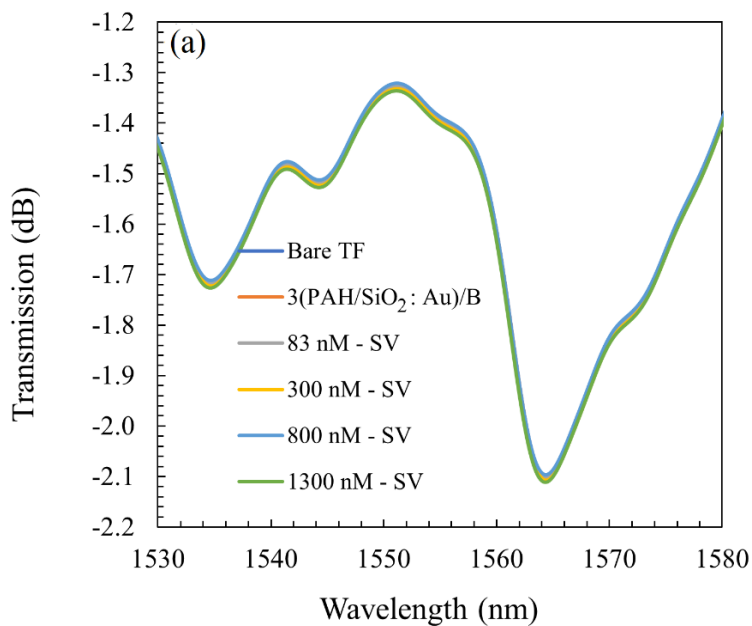


Figure 4.4 (a) Transmission spectra of a tapered fiber biosensor coated with  $(\text{PAH}/\text{SiO}_2:\text{Au})_3/\text{Biotin}$ , having a waist of  $97\ \mu\text{m}$  and surrounded by different concentrations of streptavidin protein; (b) enlarged curves in the vicinity of a resonance wavelength at  $1564.42\ \text{nm}$ .

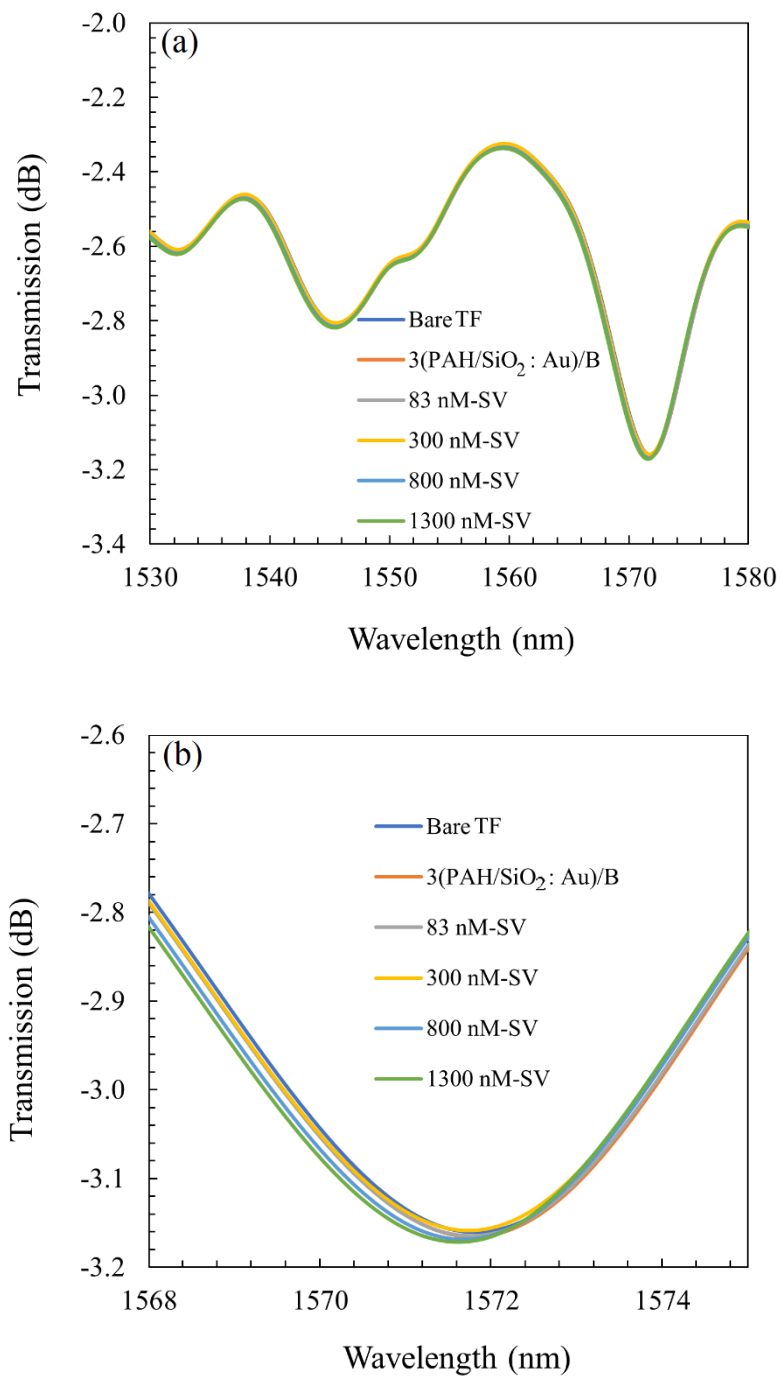


Figure 4.5 (a) Transmission spectra of a tapered fiber biosensor coated with (PAH/SiO<sub>2</sub>: Au)<sub>3</sub>/Biotin, having a waist of 58  $\mu\text{m}$  and surrounded by different SV concentrations; (b) enlarged curves in the vicinity of a resonance wavelength at 1571.85 nm.

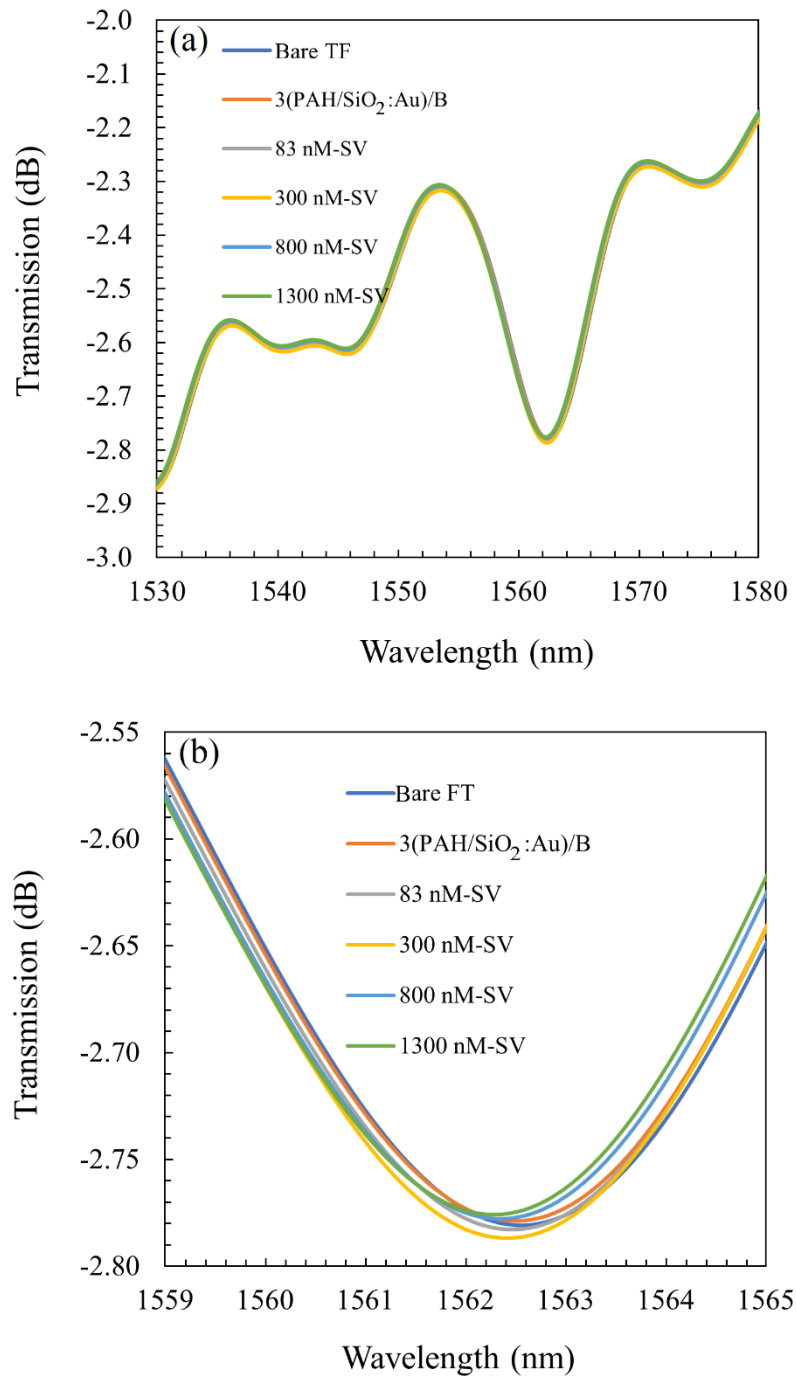


Figure 4.6 (a) Transmission spectra of a tapered fiber biosensor coated with (PAH/SiO<sub>2</sub>:Au)<sub>3</sub>/Biotin, having a waist of 45  $\mu$ m and surrounded by different SV concentrations; (b) enlarged curves in the vicinity of a peak wavelength at 1562.46 nm.

Table 4.1 Resonance wavelength shifts due to the addition of protein with different concentrations.

Tapered fiber waist ( $\mu\text{m}$ )	Shifts in resonance wavelength (nm)			
	83 nM-SV	300 nM-SV	800 nM-SV	1300 nM-SV
97	0.01	0.03	0.05	0.09
58	0.02	0.05	0.11	0.17
45	0.03	0.08	0.15	0.21

The shapes of the curves are different since the tapered waist thicknesses differ. The decrease in tapered waist thicknesses results in a larger intensity loss due to the coupling between the core and higher-order cladding modes. Thus, when the tapered waist is changed, the transmission spectrum varies accordingly.

#### 4.2.1.1 Analysis of results on (PAH/SiO<sub>2</sub>:Au)<sub>3</sub>/Biotin coated single tapered biosensors

This subsection analyzes the performance of the (PAH/SiO<sub>2</sub>:Au)<sub>3</sub>/Biotin coated biosensor derived from simulation on a single tapered fiber. According to [68], the sensitivity of a biosensor can be calculated using the following formula:

$$S = \frac{\Delta\lambda_{\max}}{\sigma}, \quad (4.2)$$

where  $\Delta\lambda_{\max}$  is the maximum wavelength shift observed in the process, and  $\sigma$  is the surface density of the detected biomaterial, as described by the following equation:

$$\sigma = \frac{M_{\text{MW}}}{N_{\text{A}} \times P^2}, \quad (4.3)$$

where  $M_{MW}$  is the molecular weight of Streptavidin ( $M_{MW} = 60.0$  g/mol),  $N_A$  is Avogadro's number, and  $P$  is the average length of Streptavidin (4.0 nm). Since  $\sigma = 6.23$  ng/mm<sup>2</sup>, the sensitivity of the single tapered fiber biosensor with a 97  $\mu\text{m}$  waist is  $0.014 \pm 0.008$  nm/(ng/mm<sup>2</sup>). The corresponding sensitivities for single tapered fiber biosensors with 58 and 45  $\mu\text{m}$  waists are  $0.027 \pm 0.008$  and  $0.033 \pm 0.008$  nm/(ng/mm<sup>2</sup>), respectively. These results are reasonable since decreasing the tapered waist excites more cladding modes, and as a result, the biosensor becomes more sensitive to external change in the refractive index.

Figure 4.7 shows shifts in the resonance wavelengths when SV protein concentrations change. The sensitivity of the sensors increases with a decrease in the thicknesses of the tapered waists.

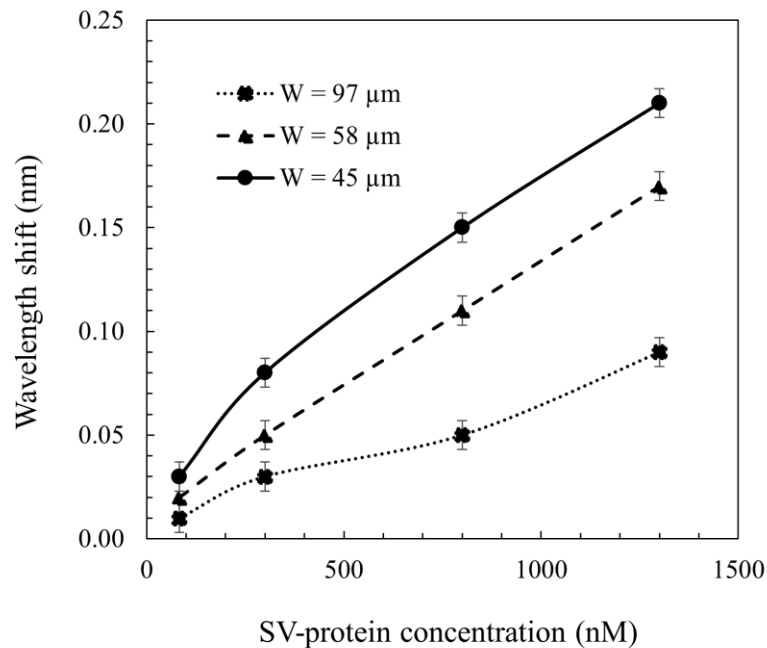


Figure 4.7 Comparison of resonance wavelength shifts for three tapered fiber-based biosensors with three different waist thicknesses, all coated with (PAH/SiO<sub>2</sub>: Au)<sub>3</sub>/Biotin.

#### 4.2.2 Single tapered fiber biosensor coated with (PAH/PSS)<sub>3</sub>/Biotin

The previous section described how tapered fibers coated with (PAH/SiO<sub>2</sub>:Au)<sub>3</sub>/Biotin are applied as protein sensors. This section describes a simulation on structures coated with the (PAH/PSS)<sub>3</sub>/Biotin, where PSS stands for poly(styrene-sulfonate). The structure functionalization process is the same as for the (PAH/SiO<sub>2</sub>:Au)<sub>3</sub>/Biotin case. The only difference is that, instead of depositing SiO<sub>2</sub>: Au NPs, PSS is used. The other materials and drying times are the same as in the former case. The physical and chemical properties of PSS can be found in Ref. [67]. In the COMSOL code, PAH and PSS thicknesses are determined as 50 and 40 nm [95], respectively. The refractive indices of PAH and PSS are 1.38 and 1.50 [96], respectively. Figure 4.8 shows an enlarged illustration of the coated structure designed using COMSOL Multiphysics software.

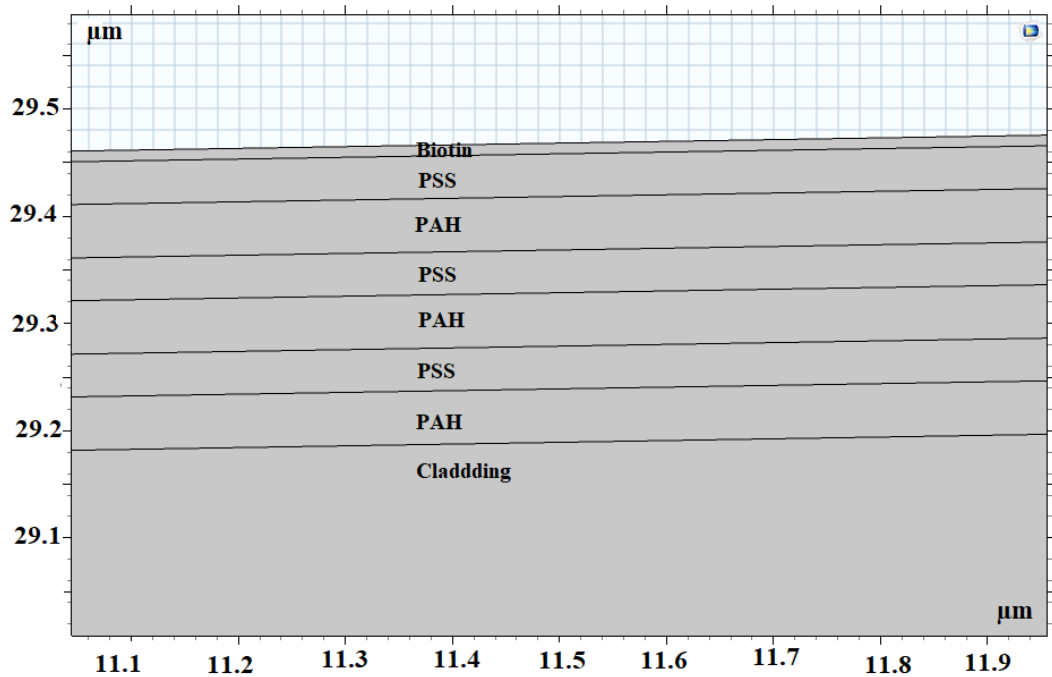


Figure 4.8 Functionalization of tapered fiber with (PAH/PSS)<sub>3</sub>/Biotin coating.

Following similar procedures for simulation using the COMSOL code, as monitored in the previous section, an adsorption interaction is activated first, after which the protein concentration is computed (the interaction between the SV proteins and the Biotins on the tapered fiber surface has been explained in Section 4.1.2). The hosts for the (PAH/PSS)<sub>3</sub>/Biotin coatings are the tapered fibers shown in Table 4.1. The waists of these structures are 97, 58, and 45 μm, while their length is fixed at 378 μm. Since the effective refractive index of (PAH/PSS)<sub>3</sub>/Biotin is around 1.425, larger than that in the (PAH/SiO<sub>2</sub>:Au)<sub>3</sub>/Biotin case (1.320), a more significant shift in resonance wavelength is expected due to an increase in protein concentration.

#### **4.2.2.1 Single tapered fiber biosensors with a waist of 97, 58, or 45 μm**

Figure 4.9 illustrates the transmission spectra of a tapered fiber with a coating of (PAH/PSS)<sub>3</sub>/Biotin having a waist of 97 μm and a length of 378 μm. Similar to the case of the (PAH/SiO<sub>2</sub>:Au)<sub>3</sub>/Biotin coated taper, the initial concentration of the SV protein is 83 nM. Note that, since the 83 nM concentration of SV protein is not sufficient to have a tangible effect of the transmission spectrum of tapered fiber, the concentration of 160 nM is added to the calculations. The peak wavelength at  $1564.490 \pm 0.001$  nm shifts to  $1564.430 \pm 0.001$  nm after coating, indicating a blueshift of  $0.060 \pm 0.002$  nm for a bare single tapered fiber in water. The resonance wavelength at 1564.430 nm serves as the reference point for measuring wavelength shifts at different SV concentrations. Adding 83 and 160 nM of SV-protein to the solution lead shifts the resonance wavelength to  $1564.350 \pm 0.001$  and  $1564.330 \pm 0.001$  nm, corresponding to blueshifts of  $0.080 \pm 0.002$  and  $0.100$

$\pm 0.002$  nm, respectively. Further increasing the SV concentration to 300 nM results in a blueshift of  $0.130 \pm 0.002$  nm in the resonance wavelength. In contrast, for 800 and 1300 nM SV concentrations, shift values are  $0.190 \pm 0.002$  and  $0.230 \pm 0.002$  nm towards shorter wavelengths, respectively. This process is also conducted for tapered fibers with a waist of 58 or 45  $\mu\text{m}$ . Table 4.2 indicates the resonance wavelength shifts at each step of the process for all three (PAH/PSS)<sub>3</sub>/Biotin coated tapered fibers. Figures 4.10 and 4.11 show the transmission spectra of single tapered fiber biosensors with waists of 58 and 45  $\mu\text{m}$ , respectively, when the protein concentrations vary.

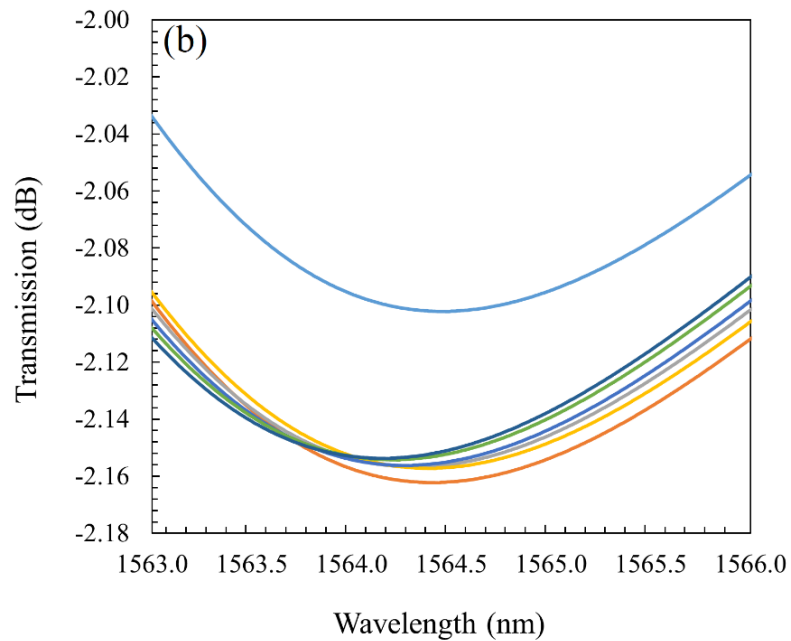
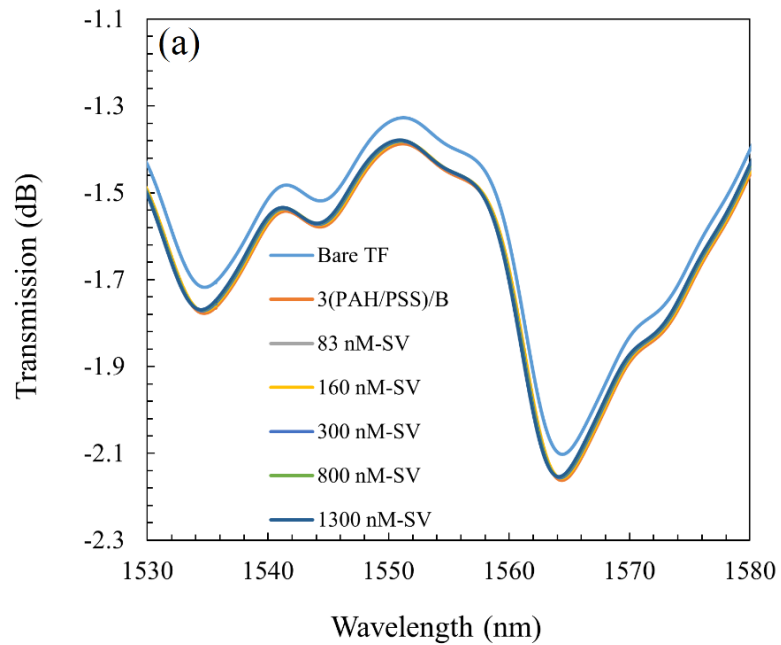


Figure 4.9 (a) Transmission spectra of  $(\text{PAH/PSS})_3/\text{Biotin}$ -coated single tapered biosensor ( $97 \mu\text{m}$  waist) with different concentrations of streptavidin protein; (b) enlarged curves in the vicinity of the resonance wavelength at  $1564.49 \text{ nm}$ .

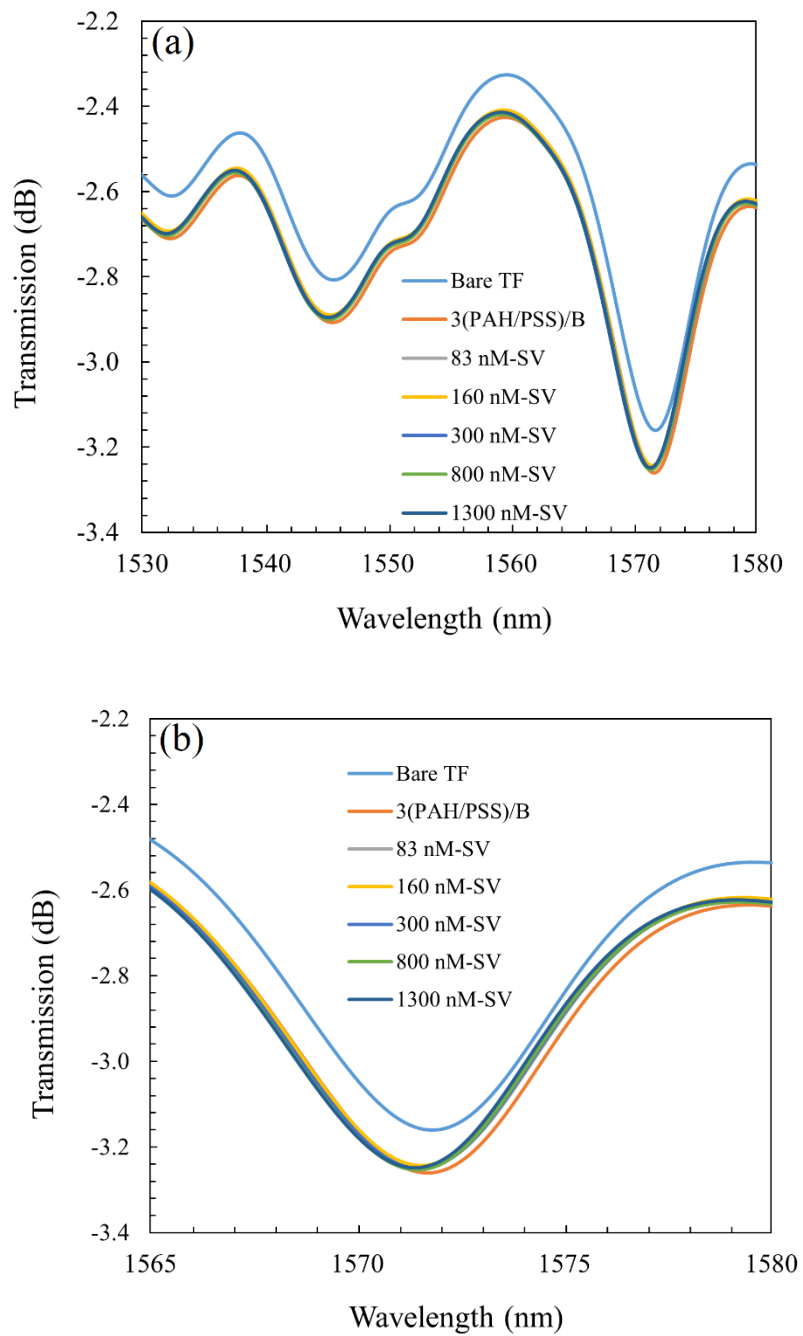


Figure 4.10 (a) Transmission spectra of (PAH/PSS)<sub>3</sub>/Biotin-coated tapered fiber biosensor (58  $\mu\text{m}$  waist) surrounded by different concentrations of SV; (b) enlarged curves in the vicinity of the resonance wavelength at 1571.80 nm.

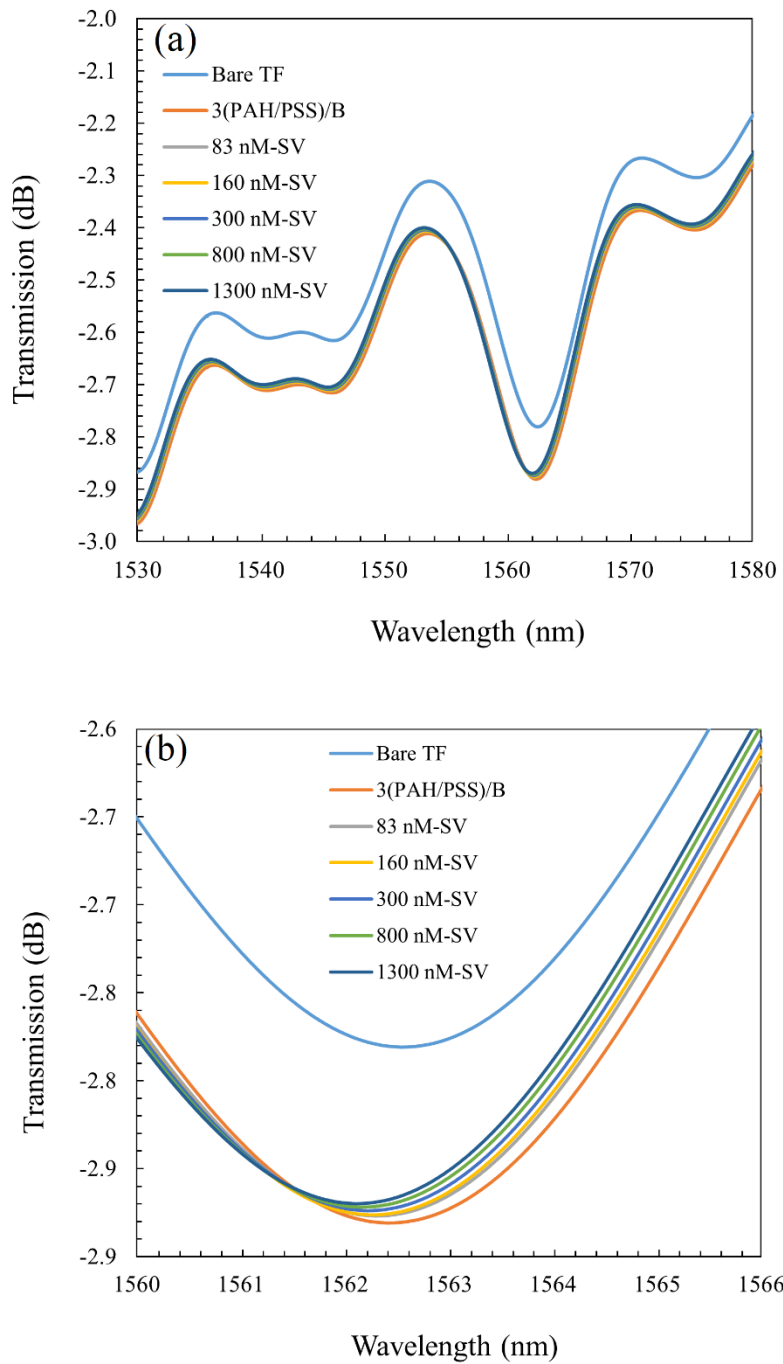


Figure 4.11 (a) Transmission spectra of (PAH/PSS)<sub>3</sub>/Biotin-coated tapered fiber biosensor (45  $\mu\text{m}$  waist) surrounded by different concentrations of SV; (b) enlarged curves in the vicinity of the resonance wavelength at 1562.55 nm.

Table 4.2 Resonance wavelength shifts for three (PAH/PSS)<sub>3</sub>/Biotin-coated single tapered fibers having different waists thicknesses.

Tapered fiber waist (μm)	Wavelength shift (nm)				
	83 nM-SV	160 nM-SV	300 nM-SV	800 nM-SV	1300 nM-SV
97	0.08	0.10	0.13	0.19	0.23
58	0.13	0.15	0.19	0.24	0.30
45	0.12	0.17	0.20	0.21	0.31

#### 4.2.2.2 Analysis of results on (PAH/PSS)<sub>3</sub>/Biotin-coated single tapered fiber biosensors

Figure 4.12 shows the dependence of the shift in the resonance wavelength of the three single tapered fiber biosensors on SV protein concentrations when the fiber tapers are coated with (PAH/PSS)<sub>3</sub>/Biotin.

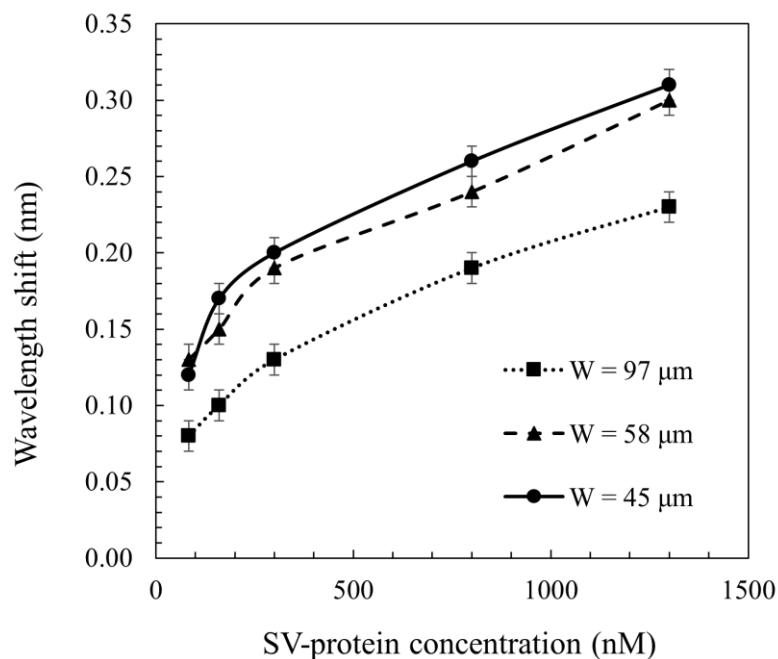


Figure 4.12 Comparison of resonance wavelength shifts for three single tapered fiber-based biosensors with three different waists thicknesses, all coated with (PAH/PSS)<sub>3</sub>/Biotin.

Clearly, the sensitivity of the biosensor with the smallest waist is the highest. This can be explained by evanescent field theory. For a taper with a smaller waist, cladding modes with higher order can be excited due to more penetration of its core mode to the cladding area [96]. Since higher-order cladding modes are more sensitive to external perturbations, the fiber tapers with smaller waist are more sensitive to the surrounding medium refractive index changes [92]. This is supported by calculating the sensitivities of the biosensors using Eq. (4.2). Repeating the calculation for these biosensors reveals sensitivities of  $0.037 \pm 0.008$ ,  $0.048 \pm 0.008$ , and  $0.050 \pm 0.008$  nm/(ng/mm<sup>2</sup>) for 97, 58, and 45  $\mu$ m waist biosensors, respectively. For a protein concentration of 83 nM, these calculations are not reasonable for the 58 and 45  $\mu$ m waists because the low protein concentration cannot considerably change the surface refractive index. Within the uncertainty range, both taper-based biosensors have approximately the same resonance wavelength shifts. However, when the protein concentration is increased to 160 nM, the resulting shifts in the transmission spectrum of 45 and 58  $\mu$ m waists of tapered fibers follows the general trend.

### **4.3 Inline tapered fiber Mach-Zehnder Interferometer as a protein sensor**

This section discusses the response of an inline tapered fiber MZI to Streptavidin protein concentration variations. The experimental study has been carried out by Maryam *et al.* [67] using two symmetrical tapered fibers as a Mach-Zehnder interferometer with a tapered waist of 58  $\mu$ m and a length of 378  $\mu$ m. The present section provides a computational analysis of the protein concentration detection using two inline tapered fiber MZIs, one

symmetrical, the other asymmetrical. Both MZIs are 4 cm in length (the distance between the centers of the two tapers)

Figure 4.13 shows the 4 cm-long inline tapered fiber MZI structure modeled in COMSOL Multiphysics software. For the symmetrical MZI, the waists and lengths of the fiber tapers are 58  $\mu\text{m}$  and 378  $\mu\text{m}$ , respectively, and the distance between the two tapered fiber centers is 4 cm. For the asymmetrical MZI, the first tapered waist is the same as 58  $\mu\text{m}$ , and the second tapered waist is reduced to 45  $\mu\text{m}$ , while the interferometer length is fixed at the same as 4 cm. The same materials with the same thicknesses are used for functionalizing MZI. As mentioned before, protein sensing is achieved through two steps: (a) adsorption process and (b) concentration detection (both steps have been explained in Section 4.1).

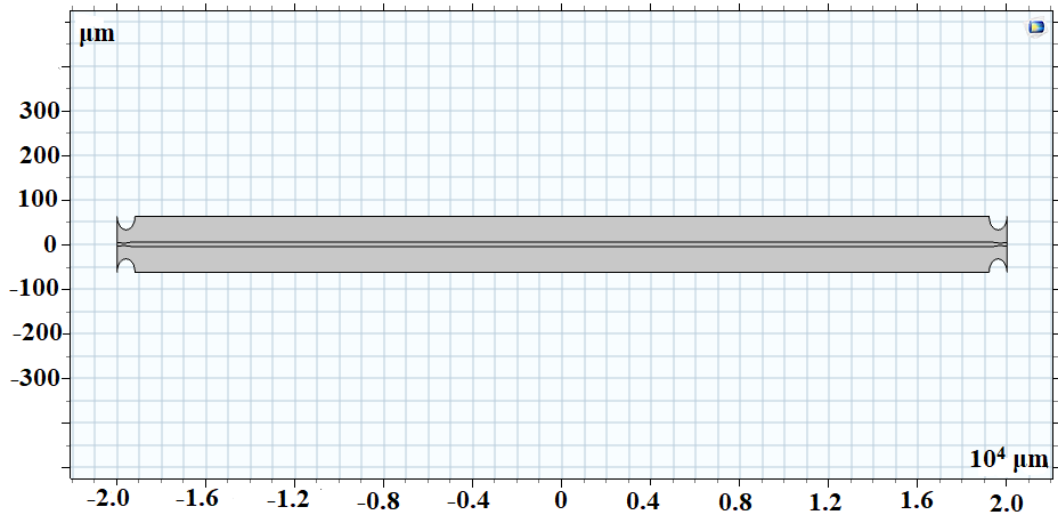


Figure 4.13 Model of a Mach-Zehnder interferometer with a length of 4 cm, adopted for simulation using COMSOL Multiphysics.

### 4.3.1 Properties of an inline symmetrical MZI coated with (PAH/SiO<sub>2</sub>:Au)<sub>3</sub>/Biotin

Figure 4.14 shows the transmission spectra of the MZI when the SV concentration changes from 83 to 1300 nM. As the protein concentration increases, the transmission spectrum shifts towards shorter wavelengths. According to Maryam's experimental results [67], no specific signal loss is found when the SV concentration increased, however, a blueshift in the resonance wavelength is observed. The 1556.10 nm resonance wavelength in the transmission spectrum of the bare MZI surrounded by water is shown in Fig 4.14(b). Coating the MZI with (PAH/SiO<sub>2</sub>:Au)<sub>3</sub>/Biotin leads to the shift of the abovementioned resonance wavelength to  $1555.95 \pm 0.01$  nm (towards shorter wavelengths), indicating a wavelength shift of  $0.15 \pm 0.02$  nm. This point is used as the reference for measuring wavelength shifts when the SV concentration changes. Adding SV protein with a concentration of 83 and 160 nM to the structure leads to shifts of resonance wavelength to  $1555.82 \pm 0.01$  and  $1555.73$  nm, showing blueshifts of  $0.12 \pm 0.02$  and  $0.22 \pm 0.02$  nm in the resonance wavelength of the transmission spectrum, respectively. Increasing the SV concentration to 300 nM results in a blueshift of  $0.40 \pm 0.02$  nm in the transmission spectrum. The corresponding resonance wavelength shifts for the SV concentration of 800 and 1300 nM are  $0.75 \pm 0.02$  and  $0.95 \pm 0.02$  nm, respectively.

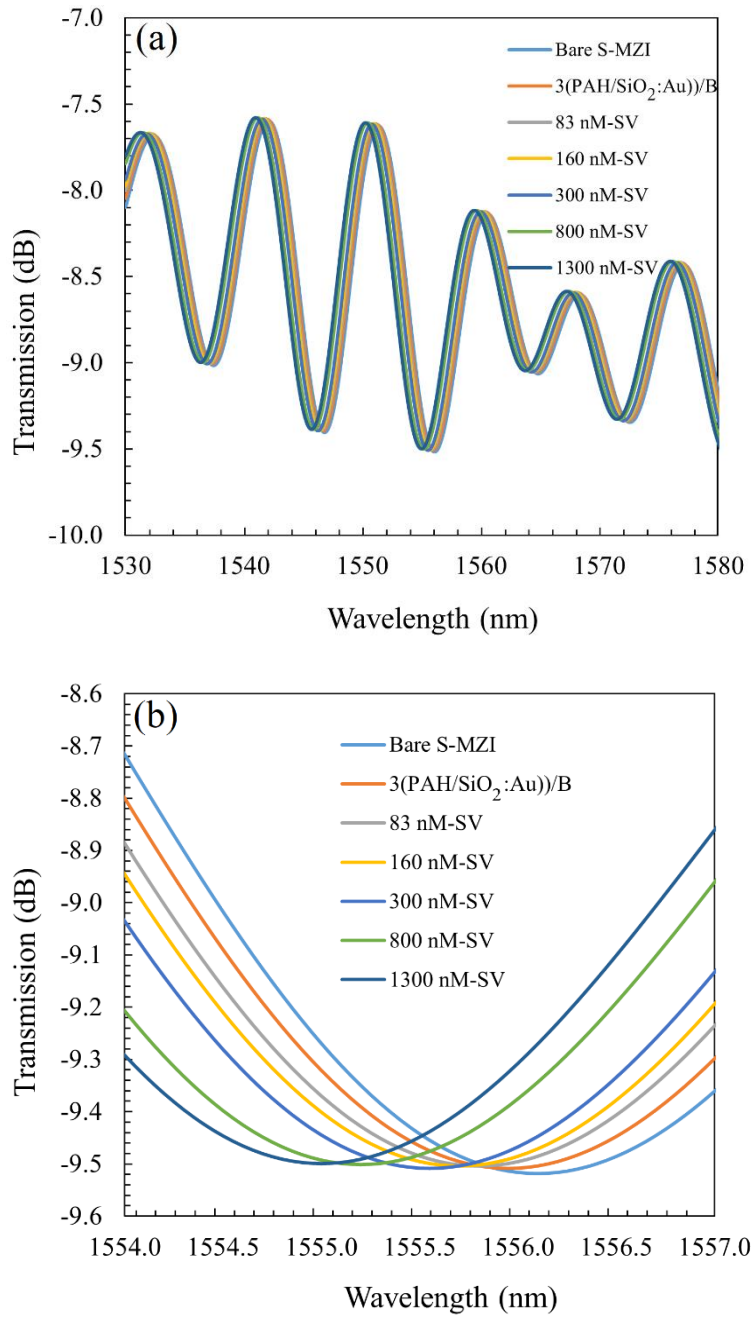


Figure 4.14 (a) Transmission spectra of a coated FMZI (length: 4 cm) with different concentrations of streptavidin protein; (b) enlarged curves around the wavelength in the vicinity of 1555.75 nm.

### 4.3.2 Properties of an inline asymmetrical MZI coated with (PAH/SiO<sub>2</sub>:Au)<sub>3</sub>/Biotin

Having considered the symmetrical MZI, it is now instructive to examine the asymmetrical one, for which the first tapered fiber (on the right in Fig. 4.13) has the same waist thickness (58  $\mu\text{m}$ ) and the same length as the symmetrical one (378  $\mu\text{m}$ ). The other taper has the same length, but its waist is shortened to 45  $\mu\text{m}$ , and the distance between tapers centers is the same as 4 cm. Similar to the practice adopted in the previous case (symmetrical MZI), as a first step, computation is performed for the bare MZI while the structure is surrounded by water, then the whole structure is coated with (PAH/SiO<sub>2</sub>:Au)<sub>3</sub>/Biotin. The addition of the SV protein at different concentrations induces shifts in the transmission spectrum of light, as indicated in Fig. 4.15. A resonance wavelength of 1556.80 nm is chosen in Fig 4.15(b) for detailed observation of resonance wavelength shift induced by different SV protein concentrations absorbed on the surface. Adding the coating to the structure leads to a shift in the resonance wavelength by  $1556.70 \pm 0.01$  nm, indicating a blueshift of  $0.10 \pm 0.02$  nm. This point is chosen as the reference of resonance wavelength for measuring shifts due to the SV concentration variations. When an 83 nM concentration of SV protein is added to the structure, the resonance wavelength in the transmission spectrum shifts by  $0.17 \pm 0.02$  nm towards shorter wavelengths. When the SV-protein concentration increases to 160 nM, the transmission spectrum shows a blueshift of  $0.27 \pm 0.02$  nm. Increasing the concentration to 300 nM shows a blueshift of  $0.45 \pm 0.02$  nm in the resonance wavelength, reaching  $1556.25 \pm 0.01$  nm. The additions of SV protein with 800 and 1300 nM

concentrations result in blueshifts in the resonance wavelength with magnitudes of  $0.90 \pm 0.02$  and  $1.00 \pm 0.02$  nm, respectively.

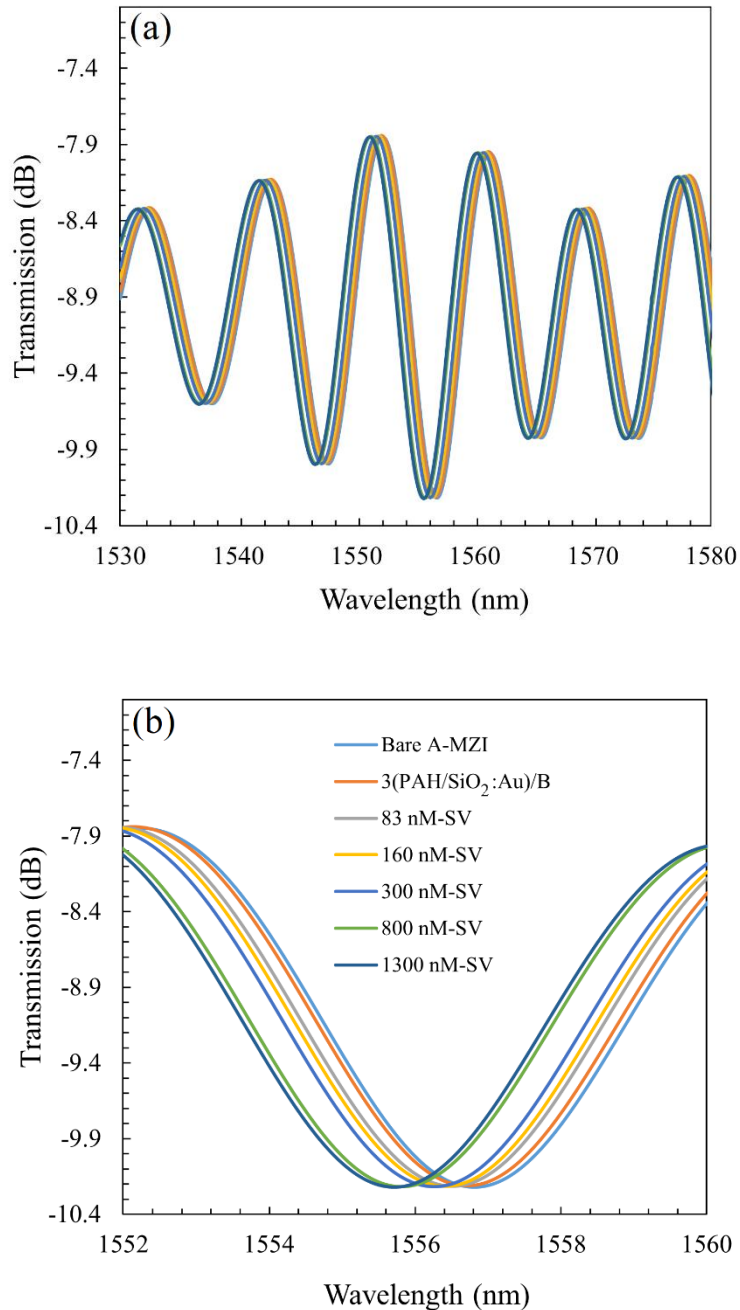


Figure 4.15 (a) Transmission spectra of coated ((PAH/SiO<sub>2</sub>:Au)<sub>3</sub>/Biotin) asymmetrical MZI (4 cm in length) with different concentrations of streptavidin protein; (b) enlarged curves around the resonance wavelength of 1556.80 nm.

#### 4.3.2.1 Analysis on results of simulation on symmetrical and asymmetrical MZI coated with $(\text{PAH}/\text{SiO}_2:\text{Au})_3/\text{Biotin}$

A comparison between the simulation results on the 4-cm-long symmetrical and asymmetrical MZI and the experimental results of the 4-cm-long symmetrical MZI is illustrated in Fig.4.16. Shifts for the asymmetrical MZI-based biosensors are more pronounced than for both symmetrical cases. In the asymmetrical MZI, the presence of the smaller waist results in more exciting cladding modes [96], inducing increasing interaction with the surrounding environment and enhancing the sensitivity to changes in any of the external parameters such as the refractive index.

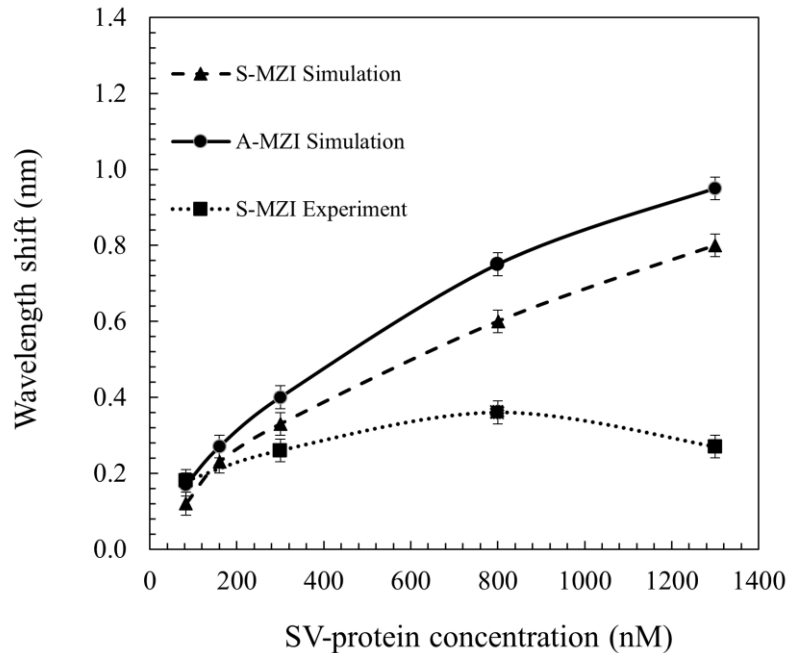


Figure 4.16 Comparison between results obtained through experimental and simulation studies on 4-cm-long symmetrical and asymmetrical MZI coated with  $(\text{PAH}/\text{SiO}_2:\text{Au})_3/\text{Biotin}$ . The dotted line shows the experimental results [67], while the dashed and solid lines indicate the simulation results for symmetrical and asymmetrical MZI, respectively.

Applying Eq. (4.2), the corresponding sensitivities for symmetrical MZI in the simulation and the experiment has been found to be  $0.144 \pm 0.080$  and  $0.07 \pm 0.08$  nm/(ng/mm<sup>2</sup>), respectively. In contrast, the sensitivity for the asymmetrical MZI in the simulation is calculated as  $0.152 \pm 0.080$  nm/(ng/mm<sup>2</sup>). Also, in the simulation, 100% adsorption (of proteins to Biotins on the surface) is assumed as indicated in Fig 4.3, therefore, the sensitivities are higher than those of the experimental results. Some SV proteins may not have reached the biotin surface during the experimental process, or some nanoparticles might be lost during the washing process [67]. As a result, the effective refractive index of the cladding could not increase as much as shown in the simulation. Another point in Fig 4.16 is related to the 83 nM protein concentration mentioned before in the discussion on single tapered fiber biosensors (Section 4.2.2.2). The 83 nM protein concentration is not significant, so that within the uncertainty range, the resonance wavelength shifts are approximately the same for all biosensors. This problem is solved for the 160 nM-SV protein concentration so that in this concentration, the blueshifts in the simulation results of both symmetrical and asymmetrical MZI-based biosensors are higher than the experimental results.

### **4.3.3 MZI protein sensor coated with (PAH/PSS)<sub>3</sub>/Biotin**

As mentioned before, the other coating material used for performing SV protein concentration measurements is (PAH/PSS)<sub>3</sub>/Biotin. Maryam *et al.* [67] carried out the corresponding experiments for the 4-cm-long MZI with two tapers having identical measurements for the waist (58 μm) and length (378 μm) (the functionalization process

was explained in Section 4.1). After the bare MZI transmission spectrum in water is obtained, the structure is coated with (PAH/PSS)<sub>3</sub>/Biotin. During this step, the second transmission spectrum is taken. Subsequent steps are adding different SV protein concentrations to the solution; and monitoring the transmission spectrum for possible shifts.

These processes are implemented on symmetrical and asymmetrical inline tapered fiber MZI in this simulation. As mentioned before, the code is compiled using COMSOL Multiphysics software.

#### **4.3.3.1 Properties of an inline symmetrical Mach-Zehnder Interferometer coated with (PAH/PSS)<sub>3</sub>/Biotin**

Figure 4.17 illustrates the transmission spectra of a 4-cm-long symmetrical MZI-based protein sensor before and after coating with (PAH/PSS)<sub>3</sub>/Biotin, when exposed to different SV protein concentrations. A resonance wavelength of 1556.10 nm in the transmission spectrum of the bare MZI fiber surrounded by water is chosen to show the transmission spectrum shift at each step, as shown in Fig. 4.17(b). Coating the structure with (PAH/PSS)<sub>3</sub>/Biotin induces a shift in the resonance wavelength from  $1556.10 \pm 0.01$  to  $1555.00 \pm 0.01$  nm, indicating a blueshift of  $1.10 \pm 0.02$  nm in the transmission spectrum. Adding SV protein at concentrations of 83 and 160 nM leads to blueshifts of the resonance wavelength  $0.90 \pm 0.02$  and  $1.3 \pm 0.02$  nm. A wavelength shift of  $1.70 \pm 0.02$  nm results from an increase in the protein concentration to 300 nM. After increasing the SV concentration to 800 and 1300 nM, the resonance wavelength shifts towards shorter wavelengths by  $2.20 \pm 0.02$  nm and  $2.40 \pm 0.02$  nm, respectively.

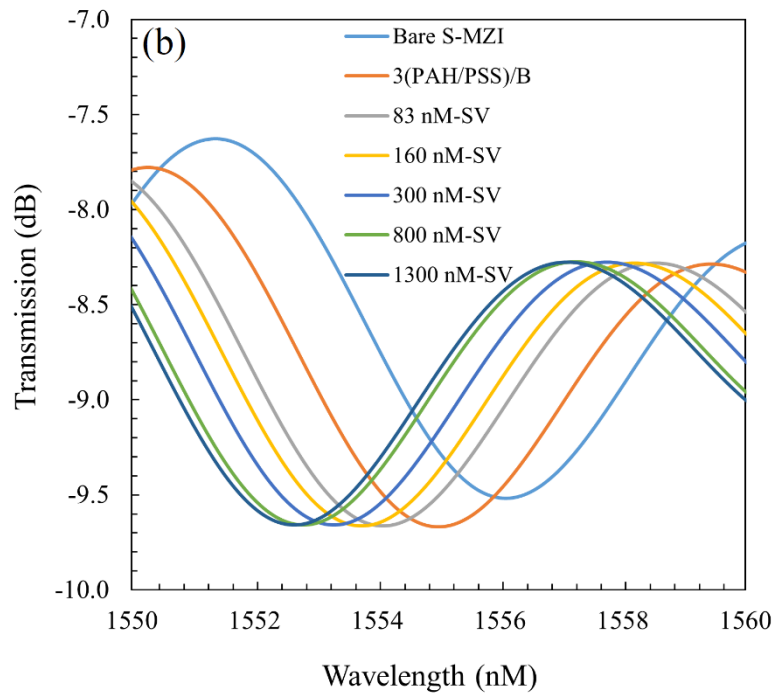
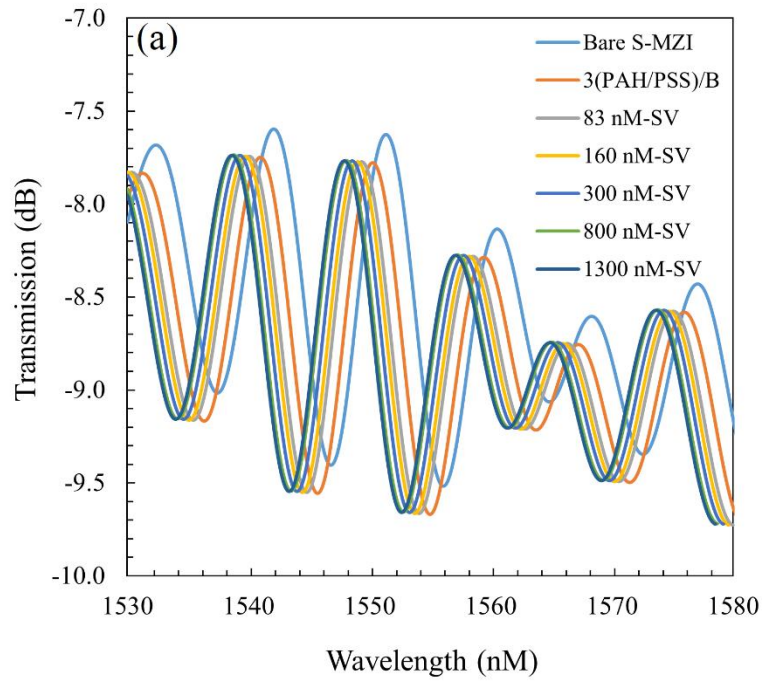


Figure 4.17 (a) Transmission spectra of  $(\text{PAH/PSS})_3/\text{Biotin}$ -coated symmetrical MZI with a length of 4 cm in different concentrations of streptavidin protein; (b) enlarged transmission spectra around the resonance wavelength of 1556.10 nm.

#### **4.3.3.2 Properties of an inline asymmetrical Mach-Zehnder Interferometer coated with (PAH/PSS)<sub>3</sub>/Biotin**

Figure 4.18 illustrates the transmission spectra of a 4-cm-long asymmetrical MZI fiber structure before and after coating with (PAH/PSS)<sub>3</sub>/Biotin while exposed to different SV concentrations. A 1556.80 nm resonance wavelength in the transmission spectrum of the bare MZI surrounded with water is chosen for determining the transmission spectrum shift at each step, as shown in Fig. 4.18(b). Coating the structure with (PAH/PSS)<sub>3</sub>/Biotin induces a shift in the resonance wavelength to  $1555.85 \pm 0.01$  nm, indicating a blueshift of  $1.05 \pm 0.02$  nm. This resonance wavelength is used as the reference point for the asymmetrical MZI coated with (PAH/PSS)<sub>3</sub>/Biotin. When an SV protein solution with a concentration of 83 nM is added, the resonance wavelength shifts by  $0.95 \pm 0.02$  nm towards shorter wavelengths. Increasing the SV concentration to 160 and 300 nM induce blueshift of  $1.45 \pm 0.02$  and  $1.85 \pm 0.02$  nm in the transmission spectrum, respectively. The solution of SV with concentrations of 800 and 1300 nM lead to shifts in the transmission spectra towards shorter wavelengths as  $2.30 \pm 0.02$  and  $2.75 \pm 0.02$  nm, respectively.

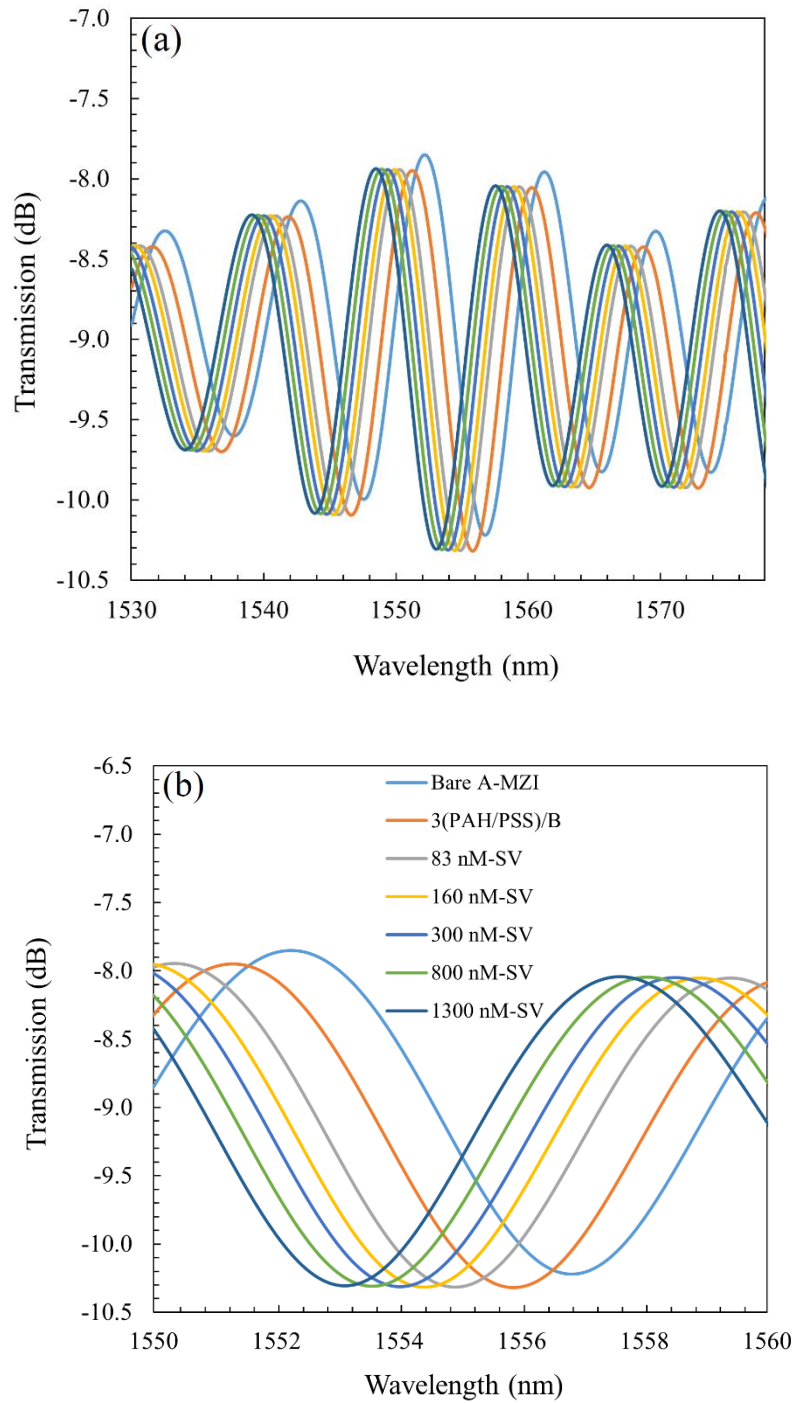


Figure 4.18 (a) Transmission spectra of (PAH/PSS)<sub>3</sub>/Biotin-coated asymmetrical MZI with a length of 4 cm with different concentrations of streptavidin protein; (b) enlarged transmission spectra around the resonance wavelength of 1556.80 nm.

#### 4.3.3.3 Analysis of results on symmetrical and asymmetrical MZI both coated with (PAH/PSS)<sub>3</sub>/Biotin

Figure 4.19 compares the simulation results for symmetrical and asymmetrical MZI sensors with the experimental results for the symmetrical sensor, all coated with (PAH/PSS)<sub>3</sub>/Biotin. Compared to the experimental results, the simulation results for both the symmetrical and asymmetrical MZI sensors indicate higher sensitivities. The asymmetrical MZI sensor shows a higher sensitivity in the simulations due to adopting a taper with a smaller, 45  $\mu\text{m}$  waist. At lower SV protein concentrations, such as 83 nM, the two symmetrical and asymmetrical MZI-based biosensors show similar results within the uncertainty range. In contrast, at a higher SV protein concentration (1300 nM), the difference in the results is significant.

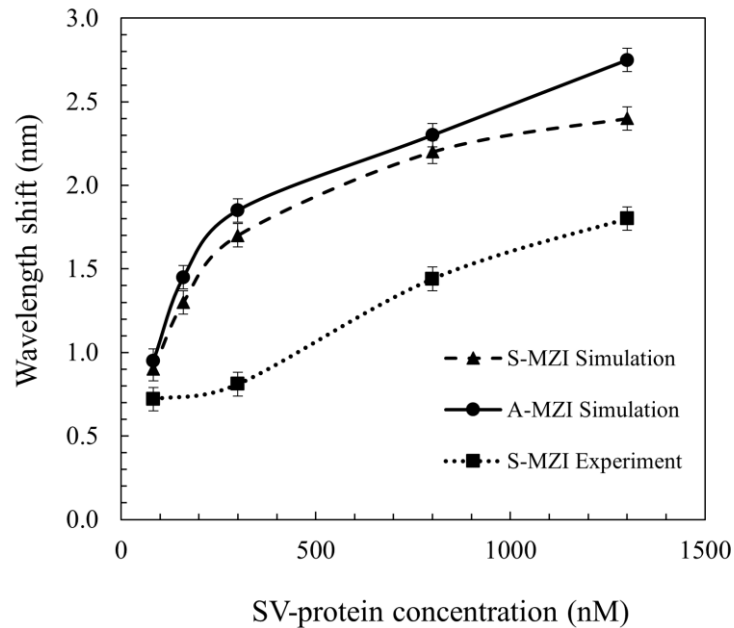


Figure 4.19 Comparison between the experimental and simulation results of 4 cm-long symmetrical and asymmetrical MZI coated with (PAH/PSS)<sub>3</sub>/Biotin. The dotted line shows the experimental result, while the dashed and solid lines indicate the simulation results for symmetrical and asymmetrical MZI, respectively.

With Eq. (4.2), sensitivities for the 4-cm symmetrical and asymmetrical MZIs are calculated as  $0.38 \pm 0.08$  and  $0.44 \pm 0.08$  nm/(ng/mm<sup>2</sup>), respectively, while the sensitivity for the experimental symmetrical case was  $0.29 \pm 0.08$  nm/(ng/mm<sup>2</sup>) [67]. Compared to the experimental result, the simulated sensitivities for both symmetrical and asymmetrical MZIs are higher. The reason for this has been mentioned in Section 4.3.2.1.

#### **4.4 Differences between the sensitivities of two biosensors**

MZI biosensor simulation using different coatings indicates that the sensitivities of these biosensors are different: the (PAH/PSS)<sub>3</sub>/Biotin coating-based biosensor shows a sensitivity several times higher than that of the (PAH/SiO<sub>2</sub>:Au)<sub>3</sub>/Biotin-coated biosensor. The effective refractive index of the nano-layers in (PAH/SiO<sub>2</sub>:Au)<sub>3</sub>/Biotin is very close to that of water (1.3300). This value is much lower than the refractive index of the cladding, which is 1.4378; therefore, nano-layer refractive index variations in the order of 10<sup>-4</sup> (resulting from the addition of protein concentrations [89]) would not significantly impact the transmission spectrum. However, in the case of (PAH/PSS)<sub>3</sub>/Biotin-coated biosensors, the effective refractive index of the layers (1.4250) is very close to the cladding refractive index (1.4478). In this case, any slight variation in the refractive index of the surrounding ambient will increasingly weaken the total internal reflection of the tapered fiber, so that more exciting cladding modes will be available to interact with the surrounding area, which results in a significant shift in the transmission spectrum. This has been proved by the simulation on an inline tapered fiber MZI with a length of 4 cm. In one case, the environmental refractive index of inline tapered fiber MZI is changed from 1.3300 to

1.3350. Figure 4.20 indicates a blueshift in the spectra. Despite a significant change in the refractive index ( $10^{-3}$ ) in comparison to changes resulting from the addition of protein ( $10^{-4}$ ) [89], the highest shift is 1.5 nm (1556.10 nm for 1.3300 and 1554.60 nm for 1.3350), while the value for protein sensing is 1.00 nm.

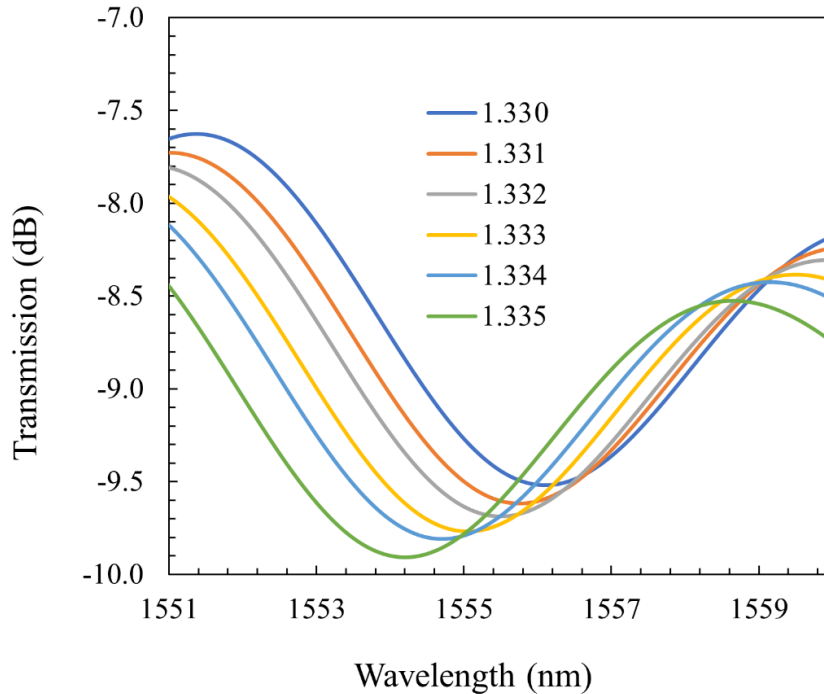


Figure 4.20 Shifts in the transmission spectrum of the MZI due to changes in the environmental refractive index around 1.330.

These simulations have been performed for the same structure but with an environmental refractive index of 1.4200. Figure 4.21 shows that any slight variation in the refractive index of the surrounding medium results in a significant shift in the transmission spectrum of the MZI. The resonance wavelength corresponding to a refractive index of 1.4200 is 1555.0 nm. The resonance wavelength shifts to 1550.8 nm for a refractive index of 1.4250, indicating a blueshift of 4.2 nm, which is approximately three times more than

the shift in the wavelength compared to the case that its environmental refractive index is around 1.330.

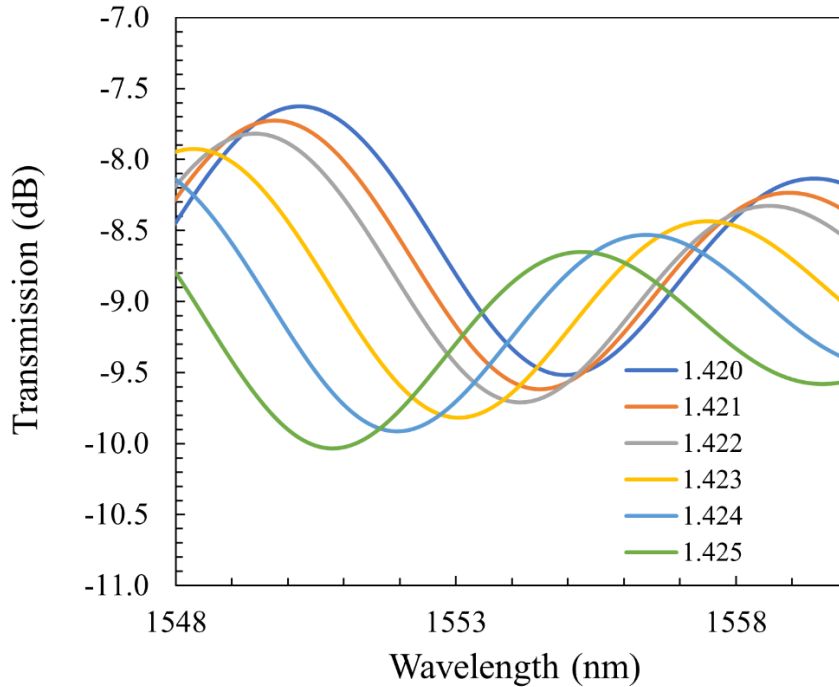


Figure 4.21 Shifts in the transmission spectrum of the MZI due to variations in the environmental refractive index around 1.4200.

In summary, this chapter has computationally and experimentally discussed single tapered fiber and inline tapered fiber-based MZI biosensing properties using two different types of surface functionalization: ((PAH/SiO<sub>2</sub>:Au)<sub>3</sub>/Biotin and (PAH/PSS)<sub>3</sub>/Biotin. Sensitivities of (PAH/PSS)<sub>3</sub>/Biotin coated biosensors are higher in both cases (single tapered fiber and inline MZI). Calculations on effective refractive indices of two different types of bilayers show that since the effective refractive index of (PAH/PSS)<sub>3</sub>/Biotin coated biosensor is very close to that of the fiber cladding, this type of biosensor is more sensitive to variations on SV protein concentration. In addition, although the simulation results show

higher sensitivities than those of the experimental results due to 100% adsorption (of proteins to Biotins on the surface), which is assumed in the simulation, the simulation results generally have revealed the same order sensitivity as the experimental results. In total, single tapered fiber and inline tapered fiber-based MZI biosensors show the excellent ability to measure the SV-protein concentrations of more than 83 nM.

## **Chapter 5 Conclusion**

Optical fiber sensors have been playing important roles in science and technology owing to their extraordinary advantages such as small size, light-weight, immunity to electromagnetic interference, and viability in harsh environments. Ongoing efforts have been aimed to improve the performance and applicability of these sensors for industrial uses. Among the photonic microstructure-based optical fiber sensors, long-period gratings and tapered fibers have found their place in modern technology. In this thesis study, long-period fiber gratings fabricated on single-mode fibers using the arc discharge method have been examined. The influence of variations of fabrication parameters on the properties of the prepared samples, including their micro-taper diameters and transmission spectra, has been investigated. The results indicate that the average diameter of micro-tapers decreases

by increasing any of the three fabrication parameters: arc current, arc duration, and tension along the fiber.

Local stress relaxation on the fiber core and cladding is a key mechanism in micro-taper formation. With typical fabrication parameters of 10 mA for the arc current and 250 ms for the arc duration, the fiber temperature in the arc position reaches 1300°C in less than half a second [58]. Applying stress in the order of several MPa induces a significant strain on the arc position in the fiber and forms the micro-tapers. This phenomenon is modeled and confirmed by simulation results using COMSOL<sup>®</sup> Multiphysics software for the first time in this study.

To investigate the changes in the transmission spectrum of fabricated LPGs, investigation on the deformations in the geometries of micro-tapers fabricated with different values of these three parameters have been implemented in the model using COMSOL Multiphysics software. The results show a blueshift in the LPG transmission spectrum when any of the three fabrication parameters increases. In general, an increase in any of the parameters leads to the formation of micro-tapers with smaller waists, which increases coupling strength and the corresponding intensity loss. With larger fabrication parameters, stress relaxation can be enhanced significantly due to higher fiber temperatures, resulting in a decrease in the core refractive index and inducing a blueshift in the resonance wavelength.

After considering fundamental LPG features, the feasibility of using such device for sensing environmental refractive index and temperature has been studied. For

environmental refractive index ranging from 1.0 to 1.4375, the shift in resonance wavelength is minimal for a surrounding medium having a refractive index close to 1. However, when the refractive index approaches that of the cladding, the resonance wavelength shifts significantly, so that for a range from environmental refractive indices 1.4000 to 1.4375, the LPG sensitivity to the surrounding medium refractive index is significant (-171.82 nm/RIU).

In general, LPG sensor sensitivity to a refractive index originates from the fact that the effective refractive index of cladding modes depends on the environmental refractive index. The effective refractive index of the cladding determines the resonance wavelength in the transmission spectrum. Tuning the ambient refractive index to approach that of the cladding weakens the total internal reflection condition. As a result, the evanescent fields existing in the fiber cladding have a greater potential to interact with the surrounding ambient, boosting the sensitivity of the sensor.

The arc-induced LPG is also simulated as a temperature sensor. A sensitivity of 10 pm/°C is obtained for this sensor. LPG sensitivity to the ambient temperature is related to the thermal expansion and the temperature-dependent modulation of the refractive indices of the fiber core and cladding. Increasing the ambient temperature causes a thermal expansion in the LPG length, shifting the resonance wavelength towards longer wavelengths. On the other hand, variations in the environmental temperature influence the refractive indices of the core and cladding and lead to a shift in the resonance wavelength.

Furthermore, tapered fibers in the configurations of either single or in-line MZI are studied as biosensors for detecting the concentration of SV protein computationally and compared with the experimental results previously obtained in our research group. According to simulation results, for the structures differently functionalized, the largest sensitivity has been found for the tapered fiber with the smallest waist. In contrast, for the in-line tapered fiber MZI, the asymmetric MZI shows the largest sensitivity. The simulation results also have revealed a very good agreement with the experimental results indicating the effective refractive indices of the coating materials play a significant role in determining the sensitivity. The effective refractive index for structures coated with (PAH/SiO<sub>2</sub>: Au)<sub>3</sub>/Biotin is 1.3340, which is considerably smaller than the cladding refractive index (1.4378). This means that any variation in the surrounding refractive index will not considerably affect the transmission spectrum. On the other hand, the effective refractive index of the (PAH/PSS)<sub>3</sub>/Biotin-coated structure is around 1.4250, which is very close to the cladding refractive index. Hence, resonance wavelength can be shifted significantly by any slight variation in the environmental refractive index due to weakening the total internal reflection of tapered fiber.

These results show the feasibility of using LPG as a sensor, a single tapered fiber, and an in-line tapered fiber MZI as biosensors, all for external parameters such as environmental temperature, refractive index, and some biomolecules like proteins (with concentrations of more than 83 nM). Based on the findings of this study, it will be possible to design LPG-based and tapered fiber-based optical fiber sensors and biosensors that can

be used in a variety of fields, including telecommunications, chemistry, medicine, and environmental sciences.

## References

- [1] Kao, K. C., and Hockham, G. A. (1966). Dielectric-fiber surface waveguides for optical frequencies. In *Proceedings of the Institution of Electrical Engineers*, 113(7), 1151-1158.
- [2] Pedrotti, F. L., Pedrotti, L. M., and Pedrotti, L. S. (2017). *Introduction to Optics*. Prentice Hall.
- [3] Buck, J. A. (2004). *Fundamentals of Optical Fibers*, 50. John Wiley and Sons.
- [4] Snyder, A. W., and Love, J. (2012). *Optical waveguide theory*. Springer Science and Business Media.
- [5] Keck, D. B. (1981). Optical fiber waveguides. *Fundamentals of Optical Fiber Communications*, 1-107, Elsevier.
- [6] Adachi, S. (2008). Distributed optical fiber sensors and their applications. In *2008 SICE Annual Conference* (pp. 329-333). IEEE.
- [7] Wu, R., Chen, X., Zhang, S., and Fu, H. (2017). Fiber-optic sensing system for simultaneous measurement of temperature and transversal loading based on reflective fiber Mach-Zehnder interferometer. In *Conference on Lasers and Electro-Optics/Pacific Rim* (p. s1146). Optical Society of America.
- [8] Phichi, M., Imyim, A., Tuntulani, T., and Aeungmaitrepirom, W. (2020). based cation-selective optode sensor containing benzothiazole Calix [4] arene for dual colorimetric  $\text{Ag}^+$  and  $\text{Hg}^{2+}$  detection. *Analytica Chimica Acta*, 1104, 147-155.
- [9] Mahnke, P., Kliebisch, O., and Damm, M. (2019). Precise characterization of a fiber-coupled laser Doppler anemometer with well-defined single scatterers. *Applied Physics B*, 125(7), 1-10.
- [10] Garcia, Y. R., Corres, J. M., and Goicoechea, J. (2010). Vibration detection using optical fiber sensors. *Journal of Sensors*, 2010, 1-12.
- [11] Lee, C. E., Taylor, H. F., Markus, A. M., and Udd, E. (1989). Optical-fiber Fabry-Perot embedded sensor. *Optics letters*, 14(21), 1225-1227.
- [12] Singh, L., Zhu, G., Singh, R., Zhang, B., Wang, W., Kaushik, B. K., and Kumar, S. (2019). Gold Nanoparticles and Uricase Functionalized Tapered Fiber Sensor for Uric Acid Detection. *IEEE Sensors Journal*, 20(1), 219-226.

- [13] Warren-Smith, S. C., Schartner, E. P., Nguyen, L. V., Otten, D. E., Yu, Z., Lancaster, D. G., and Ebendorff-Heidepriem, H. (2019). Stability of grating-based optical fiber sensors at high temperatures. *IEEE Sensors Journal*, 19(8), 2978-2983.
- [14] Arie, A., Karoubi, R., Gur, Y. S., and Tur, M. (1986). Measurement and analysis of light transmission through a modified cladding optical fiber with applications to sensors. *Applied optics*, 25(11), 1754-1758.
- [15] Kamizi, M. A., Lugarini, D., Fuser, R., Negri, L. H., Fabris, J. L., and Muller, M. (2019). Multiplexing Optical Fiber Macro-Bend Load Sensors. *Journal of Lightwave Technology*, 37(18), 4858-4863.
- [16] Mathew, J., Semenova, Y., Rajan, G., Wang, P., and Farrell, G. (2011). Improving the sensitivity of a humidity sensor based on fiber bend coated with a hygroscopic coating. *Optics and Laser Technology*, 43(7), 1301-1305.
- [17] Casas, J. R., and Cruz, P. J. (2003). Fiber optic sensors for bridge monitoring. *Journal of Bridge Engineering*, 8(6), 362-373.
- [18] Kumar, P., Kumar, S., Kumar, J., Purbia, G. S., Prakash, O., and Dixit, S. K. (2019). Graphene-oxide-coated fiber Bragg grating sensor for ethanol detection in petrol. *Measurement Science and Technology*, 31(2), 025109.
- [19] Zhao, N., Lin, Q., Jiang, Z., Yao, K., Tian, B., and Zhang, Z. (2019). High Temperature Sapphire Optical Fiber Sensor. *Sensors and Transducers*, 237(9/10), 37-42.
- [20] Sánchez-Escobar, S., and Hernández-Cordero, J. (2019). Fiber-optic fluorescence temperature sensors using up-conversion from rare-earth polymer composites. *Optics Letters*, 44(5), 1194-1197.
- [21] Huang, Z., Zhu, Y., Chen, X., and Wang, A. (2005). Intrinsic Fabry-Pe/SPL acute/rot fiber sensor for temperature and strain measurements. *IEEE Photonics Technology Letters*, 17(11), 2403-2405.
- [22] Liu, T., Zhang, W., Wang, S., Jiang, J., Liu, K., Wang, X., and Zhang, J. (2018). Temperature insensitive and integrated differential pressure sensor for liquid level sensing based on an optical fiber Fabry-Perot interferometer. *IEEE Photonics Journal*, 10(4), 1-8.
- [23] Liu, S., Wang, Y., Liao, C., Wang, G., Li, Z., Wang, Q., and Tang, J. (2014). High-sensitivity strain sensor based on in-fiber improved Fabry-Perot interferometer. *Optics letters*, 39(7), 2121-2124.

- [24] Quan, M., Tian, J., and Yao, Y. (2015). Ultra-high sensitivity Fabry–Perot interferometer gas refractive index fiber sensor based on photonic crystal fiber and Vernier effect. *Optics letters*, 40(21), 4891-4894.
- [25] Song, B., Zhang, H., Miao, Y., Lin, W., Wu, J., Liu, H., and Liu, B. (2015). Highly sensitive twist sensor employing Sagnac interferometer based on PM-elliptical core fibers. *Optics express*, 23(12), 15372-15379.
- [26] Omar, M. A., Cholan, N. A., Zawawi, M. A. A. M., Jaharudin, N. A. N., Abd Rahim, M. S., Talib, R., and Ngajikin, N. H. (2020). Application of Sagnac Interferometer for Temperature Monitoring: Experimental Study. *Journal of Electronic Voltage and Application*, 1(1), 52-57.
- [27] Liu, Q., Li, S. G., and Wang, X. (2017). Sensing characteristics of an MF-filled photonic crystal fiber Sagnac interferometer for magnetic field detecting. *Sensors and Actuators B: Chemical*, 242, 949-955.
- [28] Xiao, S., Zhang, L., Wei, D., Liu, F., Zhang, Y., and Xiao, M. (2018). Orbital angular momentum-enhanced measurement of rotation vibration using a Sagnac interferometer. *Optics Express*, 26(2), 1997-2005.
- [29] Bao, L., Dong, X., Shum, P. P., and Shen, C. (2018). Compact temperature sensor with highly Germania-doped fiber-based Michelson interferometer. *IEEE Sensors Journal*, 18(19), 8017-8021.
- [30] Wang, P., Ni, K., Wang, B., Ma, Q., and Tian, W. (2019). Methylcellulose coated humidity sensor based on Michelson interferometer with thin-core fiber. *Sensors and Actuators A: Physical*, 288, 75-78.
- [31] Wang, B., Ni, K., Wang, P., Ma, Q., Tian, W., and Tan, L. (2018). A CNT-coated refractive index sensor based on Michelson interferometer with thin-core fiber. *Optical Fiber Technology*, 46, 302-305.
- [32] Li, P., Yan, H., and Zhang, H. (2018). Highly sensitive liquid level sensor based on an optical fiber Michelson interferometer with core-offset structure. *Optik*, 171, 781-785.
- [33] Vengsarkar, A. M., Lemaire, P. J., Judkins, J. B., Bhatia, V., Erdogan, T., and Sipe, J. E. (1996). Long-period fiber gratings as band-rejection filters. *Journal of Lightwave Technology*, 14(1), 58-65.
- [34] Erdogan, T. (1997). Fiber grating spectra. *Journal of Lightwave Technology*, 15(8), 1277-1294.

- [35] Chen, X., Zhang, L., Zhou, K., Davies, E., Sugden, K., Bennion, I., and Hine, A. (2007). Real-time detection of DNA interactions with long-period fiber-grating-based biosensor. *Optics letters*, 32(17), 2541-2543.
- [36] Sharma, A. K., and Marques, C. (2019). Design and performance perspectives on fiber optic sensors with plasmonic nanostructures and gratings: A review. *IEEE Sensors Journal*, 19(17), 7168-7178.
- [37] Hill, K. O., & Meltz, G. (1997). Fiber Bragg grating technology fundamentals and overview. *Journal of lightwave technology*, 15(8), 1263-1276.
- [38] Cusano, A., Paladino, D., and Iadicicco, A. (2009). Microstructured fiber Bragg gratings. *Journal of Lightwave Technology*, 27(11), 1663-1697.
- [39] James, S. W., and Tatam, R. P. (2003). Optical fiber long-period grating sensors: characteristics and application. *Measurement Science and Technology*, 14(5), 49.
- [40] Zhao, X. W., and Wang, Q. (2019). Mini-review: Recent advances in long-period fiber grating biological and chemical sensors. *Instrumentation Science and Technology*, 47(2), 140-169.
- [41] Garg, R., Tripathi, S. M., Thyagarajan, K., and Bock, W. J. (2013). Long-period fiber grating-based temperature-compensated high-performance sensor for biochemical sensing applications. *Sensors and Actuators B: Chemical*, 176, 1121-1127.
- [42] Hromadka, J., Hazlan, N. N. M., Hernandez, F. U., Correia, R., Norris, A., Morgan, S. P., and Korposh, S. (2019). Simultaneous in situ temperature and relative humidity monitoring in mechanical ventilators using an array of functionalized optical fiber long-period grating sensors. *Sensors and Actuators B: Chemical*, 286, 306-314.
- [43] Zhang, L., Liu, Y., Zhao, Y., and Wang, T. (2016). High sensitivity twist sensor based on helical long-period grating written in two-mode fiber. *IEEE Photonics Technology Letters*, 28(15), 1629-1632.
- [44] Chen, Y., Tang, F., Bao, Y., Tang, Y., and Chen, G. (2016). A Fe-C coated long-period fiber grating sensor for corrosion-induced mass loss measurement. *Optics Letters*, 41(10), 2306-2309.
- [45] Janczuk-Richter, M., Dominik, M., Roźniecka, E., Koba, M., Mikulic, P., Bock, W. J., and Niedziółka-Jönsson, J. (2017). Long-period fiber grating sensor for detection of viruses. *Sensors and Actuators B: Chemical*, 250, 32-38.

- [46] Chung, K. W., and Yin, S. (2004). Analysis of a widely tunable long-period grating by use of an ultrathin cladding layer and higher-order cladding mode coupling. *Optics Letters*, 29(8), 812-814.
- [47] Iadicicco, A., Campopiano, S., Giordano, M., and Cusano, A. (2007). Spectral behavior in thinned long period gratings: effects of fiber diameter on refractive index sensitivity. *Applied Optics*, 46(28), 6945-6952.
- [48] Del Villar, I., Fuentes, O., Chiavaioli, F., Corres, J. M., and Matias, I. R. (2018). Optimized strain long-period fiber grating (LPFG) sensors operating at the dispersion turning point. *Journal of Lightwave Technology*, 36(11), 2240-2247.
- [49] Saez-Rodriguez, D., Cruz, J. L., Johnson, I., Webb, D. J., Large, M. C. J., and Argyros, A. (2010). Water diffusion into UV inscribed long-period grating in microstructured polymer fiber. *IEEE Sensors Journal*, 10(7), 1169-1173.
- [50] Kowal, D., Statkiewicz-Barabach, G., Mergo, P., and Urbanczyk, W. (2014). Microstructured polymer optical fiber for long period gratings fabrication using an ultraviolet laser beam. *Optics Letters*, 39(8), 2242-2245.
- [51] Bhatia, V. (1999). Applications of long-period gratings to single and multi-parameter sensing. *Optics Express*, 4(11), 457-466.
- [52] Wang, Y. (2010). Review of long-period fiber gratings written by CO<sub>2</sub> laser. *Journal of Applied Physics*, 108(8), 11-29.
- [53] Rao, Y. J., Wang, Y. P., Ran, Z. L., and Zhu, T. (2003). Novel fiber-optic sensors based on long-period fiber gratings written by high-frequency CO<sub>2</sub> laser pulses. *Journal of Lightwave Technology*, 21(5), 1320-1327.
- [54] Ren, K., Ren, L., Liang, J., Kong, X., Ju, H., and Wu, Z. (2017). Online and efficient fabrication of helical long-period fiber gratings. *IEEE Photonics Technology Letters*, 29(14), 1175-1178.
- [55] Humbert, G., and Malki, A. (2002). Characterizations at very high temperature of electric arc-induced long-period fiber gratings. *Optics Communications*, 208(4-6), 329-335.
- [56] Dianov, E. M., Karpov, V. I., Grekov, M. V., Golant, K. M., Vasiliev, S. A., Medvedkov, O. I., and Khrapko, R. R. (1997). Thermo-induced long-period fiber gratings. In *Integrated Optics and Optical Fibre Communications, 11th International Conference on, and 23rd European Conference on Optical Communications (Conf. Publ. No.: 448)* (Vol. 2, pp. 53-56).

- [57] Tan, S. Y., Yong, Y. T., Lee, S. C., and Abd Rahman, F. (2015). Review on an arc-induced long-period fiber grating and its sensor applications. *Journal of Electromagnetic Waves and Applications*, 29(6), 703-726.
- [58] Colaço, C., Caldas, P., Del Villar, I., Chibante, R., and Rego, G. (2016). Arc-induced long-period fiber gratings in the dispersion turning points. *Journal of Lightwave Technology*, 34(19), 4584-4590.
- [59] Esposito, F., Ranjan, R., Campopiano, S., and Iadicicco, A. (2016). Influence of period on surrounding refractive index sensitivity of arc-induced long period gratings. *Procedia Engineering*, 168, 999-1002.
- [60] Ranjan, R., Esposito, F., Campopiano, S., and Iadicicco, A. (2017). Arc-Induced Long Period Gratings: Analysis of the Fabrication Parameters on the Surrounding Refractive Index Sensitivity. In *Advances in Optical Science and Engineering* (pp. 355-360). Springer, Singapore.
- [61] Sévigny, B., Leduc, M., Faucher, M., Godbout, N., and Lacroix, S. (2009). Characterization of the large index modification caused by electrical discharge in optical fibers. In *Conference on Lasers and Electro-Optics* (p. JTuD72). Optical Society of America.
- [62] Abrishamian, F., Dragomir, N., and Morishita, K. (2012). Refractive index profile changes caused by arc discharge in long-period fiber gratings fabricated by a point-by-point method. *Applied Optics*, 51(34), 8271-8276.
- [63] Estudillo-Ayala, J. M., Mata-Chavez, R., Hernandez-Garcia, J. C., and Rojas-Laguna, R. (2012). Long-period fiber grating produced by arc discharges. *Fiber Optic Sensors, 1*, 295-316.
- [64] Rego, G. (2009). Annealing of arc-induced gratings at high temperatures. *Electronics Letters*, 45(19), 972-974.
- [65] Erdogan, T. (1997). Cladding-mode resonances in short-and long-period fiber grating filters. *Journal of the Optical Society of America A*, 14(8), 1760-1773.
- [66] Costa, R. Z. V., Kamikawachi, R. C., Muller, M., and Fabris, J. L. (2009). Thermal characteristics of long-period gratings 266 nm UV-point-by-point induced. *Optics Communications*, 282(5), 816-823.
- [67] Alharbi, M. (2018). In-line tapered fiber Mach-Zehnder interferometer for biosensing applications (Master's thesis, *Memorial University of Newfoundland*).

- [68] Marques, L., Hernandez, F. U., James, S. W., Morgan, S. P., Clark, M., Tatam, R. P., and Korposh, S. (2016). Highly sensitive optical fiber long-period grating biosensor anchored with silica core gold shell nanoparticles. *Biosensors and Bioelectronics*, 75, 222-231.
- [69] Polycarpou, A. C. (2005). Introduction to the finite element method in electromagnetics. *Synthesis Lectures on Computational Electromagnetics*, 1(1), 1-126.
- [70] Tahhan, S. R. A., and Falih, A. (2017). Design and Simulation of Fiber Bragg Grating by Comsol Multiphysics Software. *Electronics and Communication Engineering*, 6(5), 2085-2095
- [71] Yablon, A. D. (2005). Mechanics of fusion splicing. *Optical Fiber Fusion Splicing*, 103, 49-89.
- [72] Borzycki, K., Kobelke, J., Schuster, K., and Wójcik, J. (2010). Arc fusion splicing of photonic crystal fibers to standard single mode fibers. In *Photonic Crystal Fibers IV*, (7714), 771414. International Society for Optics and Photonics.
- [73] do Rego, G. M. (2006). Arc-induced long-period fibre gratings. Fabrication and their applications in optical communications and sensing (Doctoral dissertation, *Universidade do Porto* (Portugal)).
- [74] Pan, Z., Kobelke, J., Schuster, K., and Bartelt, H. (2015). Determination of effective axial temperature profile in tube furnaces via the viscous stretching Method. *Optical Materials Express*, 5(9), 2024-2035.
- [75] Caldas, P., Jorge, P. A., Rego, G., Frazão, O., Santos, J. L., Ferreira, L. A., and Araújo, F. (2011). Fiber optic hot-wire flowmeter based on a metallic coated hybrid long period grating/fiber Bragg grating structure. *Applied Optics*, 50(17), 2738-2743.
- [76] Coelho, J. M., Nespereira, M., Abreu, M., and Rebordão, J. (2013). 3D finite element model for writing long-period fiber gratings by CO<sub>2</sub> laser radiation. *Sensors*, 13(8), 10333-10347.
- [77] Li, Y., Wei, T., Montoya, J. A., Saini, S. V., Lan, X., Tang, X., and Xiao, H. (2008). Measurement of CO<sub>2</sub>-laser-irradiation-induced refractive index modulation in single-mode fiber toward long-period fiber grating design and fabrication. *Applied Optics*, 47(29), 5296-5304.
- [78] Rego, G. M., Santos, J. L., and Salgado, H. M. (2006). Refractive index measurement with long-period gratings arc-induced in pure-silica-core fibres. *Optics Communications*, 259(2), 598-602.

- [79] Bhatia, V. (1999). Applications of long-period gratings to single and multi-parameter sensing. *Optics Express*, 4(11), 457-466.
- [80] Grubsky, V., and Feinberg, J. (2000). Long-period fiber gratings with variable coupling for real-time sensing applications. *Optics Letters*, 25(4), 203-205.
- [81] Chong, J. H., Shum, P., Haryono, H., Yohana, A., Rao, M. K., Lu, C., and Zhu, Y. (2004). Measurements of refractive index sensitivity using a long period grating refractometer. *Optics Communications*, 229(1-6), 65-69.
- [82] Saad, A., Cho, Y., Ahmed, F., and Jun, M. B. G. (2016). Numerical Approach to Modeling and Characterization of Refractive Index Changes for a Long Period Fiber Grating Fabricated by Femtosecond Laser. *Materials*, 9(11), 941.
- [83] Khaliq, S., James, S. W., and Tatam, R. P. (2002). Enhanced sensitivity fiber optic long period grating temperature sensor. *Measurement Science and Technology*, 13(5), 792-795.
- [84] Bhatia, V., Campbell, D. K., Sherr, D., D'Alberto, T., Zabaronick, N., Ten Eyck, G. A., and Claus, R. O. (1997). Temperature-insensitive and strain-insensitive long-period grating sensors for smart structures. *Optical Engineering*, 36(7), 1872-1877.
- [85] James, S. W., and Tatam, R. P. (2003). Optical fiber long-period grating sensors: characteristics and application. *Measurement Science and Technology*, 14(5), 49-61.
- [86] Lu, P., Men, L., Sooley, K., and Chen, Q. (2009). Tapered fiber Mach-Zehnder interferometer for simultaneous measurement of refractive index and temperature. *Applied Physics Letters*, 94(13), 131110.
- [87] Gill, R. S., Saraf, R. F., and Kundu, S. (2013). Self-assembly of gold nanoparticles on poly (allylamine hydrochloride) nanofiber: A new route to fabricate "necklace" as single-electron devices. *ACS Applied Materials and Interfaces*, 5(20), 9949-9956.
- [88] Kim, J. W., Kim, L. U., and Kim, C. K. (2007). Size control of silica nanoparticles and their surface treatment for fabrication of dental nanocomposites. *Biomacromolecules*, 8(1), 215-222.
- [89] Schauer, C. L., Chen, M. S., Chatterley, M., Eisemann, K., Welsh, E. R., Price, R. R., and Ligler, F. S. (2003). Color changes in chitosan and poly (allylamine) films upon metal binding. *Thin Solid Films*, 434(1-2), 250-257.
- [90] Tan, C. Z., and Arndt, J. (2000). Temperature dependence of refractive index of glassy SiO<sub>2</sub> in the infrared wavelength range. *Journal of Physics and Chemistry of Solids*, 61(8), 1315-1320.

- [91] Kubo, S., Diaz, A., Tang, Y., Mayer, T. S., Khoo, I. C., and Mallouk, T. E. (2007). Tunability of the refractive index of gold nanoparticle dispersions. *Nano Letters*, 7(11), 3418-3423.
- [92] Swift, J. L., and Cramb, D. T. (2008). Nanoparticles as fluorescence labels: is size all that matters? *Biophysical Journal*, 95(2), 865-876.
- [93] Himmelhaus, M., Krishnamoorthy, S., and Francois, A. (2010). Optical sensors based on whispering gallery modes in fluorescent microbeads: response to specific interactions. *Sensors*, 10(6), 6257-6274.
- [94] Urrutia, A., Bojan, K., Marques, L., Mullaney, K., Goicoechea, J., James, S., and Korposh, S. (2016). Novel highly sensitive protein sensors based on tapered optical fibers modified with Au-based nano coatings. *Journal of Sensors*, 2016, 1-11.
- [95] Gentile, F., Coppedè, N., Tarabella, G., Villani, M., Calestani, D., Candeloro, P., and Di Fabrizio, E. (2014). Microtexturing of the conductive PEDOT: PSS polymer for super hydrophobic organic electrochemical transistors. *BioMed Research International*, 2014, 1-10.
- [96] Yang, Z., Fang, Z., Sheng, J., Ling, Z., Liu, Z., Zhu, J., and Ye, J. (2017). Optoelectronic evaluation and loss analysis of PEDOT: PSS/Si hybrid heterojunction solar cells. *Nanoscale Research Letters*, 12(1), 1-6.
- [97] Ruddy, V., MacCraith, B. D., and Murphy, J. A. (1990). Evanescent wave absorption spectroscopy using multimode fibers. *Journal of Applied Physics*, 67(10), 6070-6074.